

**Studies on real-time and high sensitive  
monitoring methods for material processing  
using ultrashort-pulse laser techniques**

**HIRAOKA Takehiro**

2013

Nagoya University

Department of Electrical Engineering and Computer Science



# Contents

## Chapter 1 Introduction

1.1 Ultrashort-Pulse Laser.....	1
1.2 Wavelength-Tunable Ultrashort-Pulse Laser and Supercontinuum.....	3
1.3 Monitoring of Substrate Temperature for Plasma Processing.....	7
1.3.1 Conventional monitoring methods of substrate temperatures.....	15
1.3.1.1 Thermocouple.....	17
1.3.1.2 Fluorescent-type thermometer.....	19
1.3.1.3 Infrared radiation thermometer.....	20
1.3.1.4 Raman scattering thermometer.....	23
1.3.1.5 Substrate temperature monitoring using high-coherence Interferometry.....	24
1.3.2 Problems in substrate temperature monitoring using conventional low-coherence interferometry.....	25
1.4 High-Sensitive Monitoring for Biomaterials.....	27
1.5 Purpose and Composition of This Thesis.....	34
References for Chapter 1.....	37

## **Chapter 2 Principles of Measurement Methods**

2.1 Introduction.....	44
2.2 Substrate Temperature Measurement.....	44
2.2.1 Michelson interferometry.....	44
2.2.2 Low-Coherence Interferometry.....	47
2.2.3 Theory of Substrate Temperature Measurement.....	51
2.3 Cavity Ring-Down Spectroscopy.....	55
2.4 Summary.....	58
References for Chapter 2.....	59

## **Chapter 3 Temperature Measurement of Si Substrate Using Optical-Fiber-Type Low-Coherence Interferometry Employing Supercontinuum light**

3.1 Introduction.....	60
3.2 Experimental.....	62
3.3 Results and Discussion.....	65
3.3.1 Interference waveform.....	65
3.3.2 Numerical simulation of interference waveforms.....	69

## Contents

3.3.3 Temperature measurement of SiO <sub>2</sub> /Si substrate.....	78
3.4 Summary.....	82
References for Chapter 3.....	84

## **Chapter 4 Temperature Measurement of Silicon Substrate with Carbon Nanowalls Using Optical Low-Coherence Interferometry**

4.1 Introduction.....	85
4.2 Experimental.....	87
4.3 Results and Discussion.....	89
4.3.1 Fabrication of Carbon nanowalls.....	89
4.3.2 Interferogram of CNWs/Si substrate using SLDs and SC.....	92
4.3.3 Measurement of temperature parameters of CNWs/Si substrate.....	94
4.4 Summary.....	99
References for Chapter 4.....	100

## **Chapter 5 Optical-Fiber-Type Broadband Cavity Ring-Down Spectroscopy Using Wavelength-Tunable Ultrashort Pulsed Light**

5.1 Introduction.....	102
5.2 Experimental.....	105
5.3 Results and Discussion.....	108
5.3.1 Ring-down measurement on single-wavelength.....	108
5.3.2 Absorption measurement of glucose on multi-wavelength.....	112
5.4 Summary.....	115
References for Chapter 5.....	116

## **Chapter 6 Conclusions**

6.1 Summary of This Thesis.....	118
6.2 Scopes of Future work.....	121
Reference for Chapter 6.....	123

## **Acknowledgements.....124**

## **List of Papers.....127**

# Chapter 1

## Introduction

### 1.1 Ultrashort-Pulse Laser

Recently, ultrashort-pulse lasers have attracted much attention because of their useful applications. For example, various essential processes proceed in the femto to pico second time scale in not only atomic and molecules and but also their interactions.

The ultrashort-pulse lasers are also expected to be applied to the industrial field. Especially, in the optical communication and the computer technology, the ultrashort pulses are suitable for satisfying a social requirement to deal with huge information as fast as possible. In the material processing field, a fine and accurate processing without heat damage is strongly required. The ultrashort pulses have very-high instantaneous peak power with small average power or pulse energy, which is very useful for the laser

## Chapter 1

processing without excess heating. From the feature, they are expected to apply the ultrashort-pulse laser to the eye surgery to correct short sight in the medical field.

Recently, ultrashort-pulse fiber lasers are also intensively investigated among these ultrashort-pulse lasers. They have very practical features such as good stability, compactness, and high beam quality, because the fiber lasers are mainly composed of optical fibers. Er-doped fiber lasers have received much attention since 1980s, because the lasing wavelength at 1.55  $\mu\text{m}$  is within the low-loss window of optical fibers, which is appropriate for optical fiber communications. The first passive mode-locking was realized with a figure-eight fiber configuration in 1991.<sup>[1]</sup> The pulse width of 3.3 ps was achieved using nonlinear mirror effect in a fiber. The first passively mode-locked Yb-doped fiber laser was demonstrated in 1997.<sup>[2, 3]</sup> The 36-fs pulses were directly generated from the fiber ring cavity by optimizing the cavity dispersion.<sup>[4]</sup>

Ultrashort-pulse lasers have attracted much attention from the viewpoints of physical, chemical and engineering fields as described above.

## **1.2 Wavelength-Tunable Ultrashort-Pulse Laser and Supercontinuum**

The wavelength-tunable ultrashort-pulse lasers are very useful for applications in diverse areas such as ultrafast spectroscopy, material processing, optoelectronics, nonlinear optics, ultrafast optical chemistry and so on. The representatives are dye lasers, solid-state lasers, and optical parametric oscillators (OPOs) using nonlinear devices.

The ultrashort-pulse solid-state lasers generate sub-100-fs pulses in the near-infrared region. Among them, the Ti:Sapphire laser is widely used since it has the broad wavelength-tuning range from 700 to 1100 nm. However, the requirement of the expertise about the fine optical alignment limits the operation to only engineers or researchers with specialized laser techniques.

On the other hand, the very practical wavelength-tunable ultrashort-pulse laser was demonstrated by N. Nishizawa and T. Goto in 1999.<sup>[5]</sup> The laser was a passively mode-locked Er-doped fiber laser composed of a variable attenuator, and an anomalous-dispersive fiber. A soliton pulse generated as the femtosecond pulse with the high-peak power was injected into the negative group-velocity dispersion region of the fiber as shown in Fig. 1.1. The wavelength of the soliton pulse was shifted toward the longer-wavelength side depending on the laser power injected into the fiber. A

## Chapter 1

sech<sup>2</sup>-shaped Fourier-transform limited sub-300-fs pulse is obtained at the fiber end. The generated pulse is often called “Raman soliton pulse” because this phenomenon is caused by the formation of fundamental soliton pulse and the soliton self-frequency shift (SSFS) through the stimulated Raman scattering. [6, 7]

The SSFS enables the ultra-wide wavelength tuning range beyond the gain bandwidth of fiber amplifier. The Raman soliton pulse was generated in the wavelength region of 1.56 - 2.03  $\mu\text{m}$ . An electronically controllable, high-speed wavelength-tuning can be realized by introducing an acousto-optic modulator (AOM) as an intensity modulator. [8]

The anti-stokes pulses were also generated in the short-wavelength region by replacing the anomalous-dispersive fiber by a dispersion-shifted fiber, which zero-dispersion wavelength is close to the pump wavelength. [9]

Supercontinuum (SC) source is a new type of light source that provide a combination of desirable features: high output power, a broad spectrum, and a high degree of spatial coherence that allows tight focusing. A supercontinuum source typically consists of a pulse laser and a nonlinear element, in which a combination of nonlinear effects broadens the narrow-band laser radiation into a continuous spectrum without destroying the spatial coherence of the laser light.

## Chapter 1

Since its discovery in the late 1960's by Alfano and Shapiro,<sup>[10]</sup> SC generation has been widely studied due to the large potential applications such as optical coherence tomography (OCT), multi-photon excited fluorescence microscopy, frequency metrology, extremely short pulse generation, optical communications and so on.<sup>[11-14]</sup>

A dramatic bandwidth expansion over an octave was brought by the development of new highly nonlinear optical fibers. In 2000, J. K. Ranka et al. realized the SC generation extending from 390 to 1600 nm by injecting the 100-fs Ti:Sapphire laser pulse with only 0.8 nJ pulse energy into a 75-cm-long microstructured photonic crystal fiber.<sup>[15]</sup> In 2001, an all-fiber SC source with a wideband around 1.55  $\mu\text{m}$  was developed using passively mode-locked Er-doped fiber laser and highly-nonlinear fibers by N. Nishizawa and T. Goto, as shown in Fig. 1.2.<sup>[16]</sup> The source is stable, compact, and lightweight compared with the solid-state-laser-based SC sources due to its all-fiber configuration.

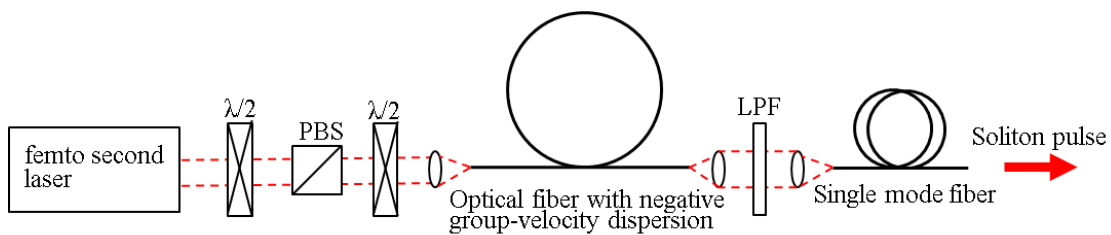


Fig. 1.1 Experimental setup for soliton pulse generation<sup>[5]</sup> PBS; polarization beam splitter, LPF, long pass filter

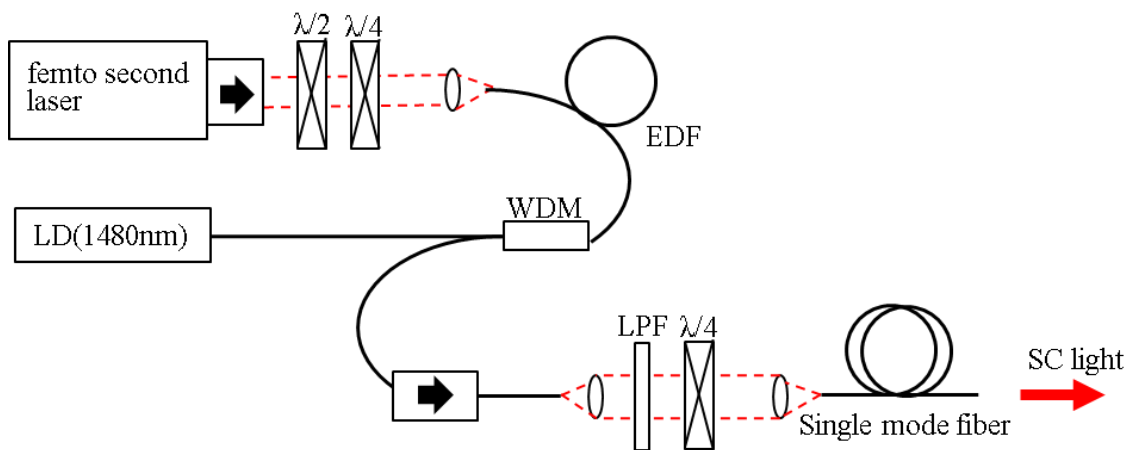


Fig. 1.2 Schematic diagram of supercontinuum (SC) light source.<sup>[16]</sup> EDF, Er doped fiber; LD, laser diode; WDM; wavelength division multiplex coupler, LPF, long pass filter; HNLFF, highly nonlinear fiber

## **1.3 Monitoring of Substrate Temperature for Plasma Processing**

Plasma processes that use non-equilibrium plasmas are indispensable for manufacturing ultralarge scale integrated (ULSI) circuits, solar cells, and liquid crystal devices. Plasma processes have many advantages in comparison with thermal and wet chemical processes for etching, deposition, and surface modification. ULSI circuits have been rapidly decreasing in size in accordance with Moore's law. Table 1.1 shows the interconnect technology requirements for MPU and DRAM, which International Technology Roadmap for Semiconductors (ITRS) showed on 2011.<sup>[17]</sup> The wafer diameter has become larger for enhancing the device yield and cost-effective products. The density of interconnect in a chip has increased. For this purpose, the interconnecting technology is getting more complicated.

Table 1.1 Interconnect technology requirements<sup>[17]</sup>

Year of Production	2012	2013	2014	2015	2016	2017	2018	2019
MPU/ASIC Metal 1 ½ Pitch (nm)(contacted)	32	27	24	21	18.9	16.9	15	13.4
DRAM ½ Pitch (nm)(contacted)	31	28	25	22	20	18	16	14
Wafer diameter	300	450	450	450	450	450	450	450
Total interconnect length (m/cm <sup>2</sup> )	2643	3143	3737	4195	4709	5285	5933	6659

As the design rules of ULSI circuits are reduced, etching processes become more complex. It is thus critical to realize ultraprecise control with few fluctuations on a subnanometer scale. Consequently, advances in the plasma technology are essential to develop the nanotechnology. Trial-and-error methods are generally used to develop plasma processes because the internal plasma state as shown in Fig. 1.3 is not sufficiently well understood so that it is treated as a black box.<sup>[17-19, 22]</sup> The etching and deposition characteristics of plasma processing are conventionally controlled through the external parameters such as electric power, pressure, and gas mixture ratio. However, in these processes, it is difficult to obtain the reproducibility of process characteristics by employing different types of process equipment since plasma

## Chapter 1

characteristics vary with mechanical variations, such as the type of plasma source and reactor size.

A new approach that controls plasma processes through internal plasma parameters such as the densities and energies of radicals, ions, and photons was proposed. In this case, the performance is independent of the reactor used. Radicals are particularly important because they play the most important role in plasma processes. A new approach that controls plasma processes through internal plasma parameters such as the densities and energies of radicals, ions, electrons, and photons has been proposed. Radicals are particularly important because they play the most important role in plasma processes. Therefore, one strategy for performing nano-processes with high-precision control is to evaluate the internal parameters and to feed back the results to the processing controlling system, that is, an autonomously controlled plasma system would monitor the internal parameters and feedback the results to the processing controlling system. For example, an autonomously controlled plasma etching system monitor the surface states and particles incident on the surface and then the external parameters of the processing controlling system which are related to the internal parameters are automatically adjusted to realize high performance. This new approach enable to evaluate the phenomena and performances which depend on the plasma reactor in terms

of the same criteria. In this case, the performance is independent of the reactor used.

This will allow results obtained in different type of plasma reactors to be compared with each other.

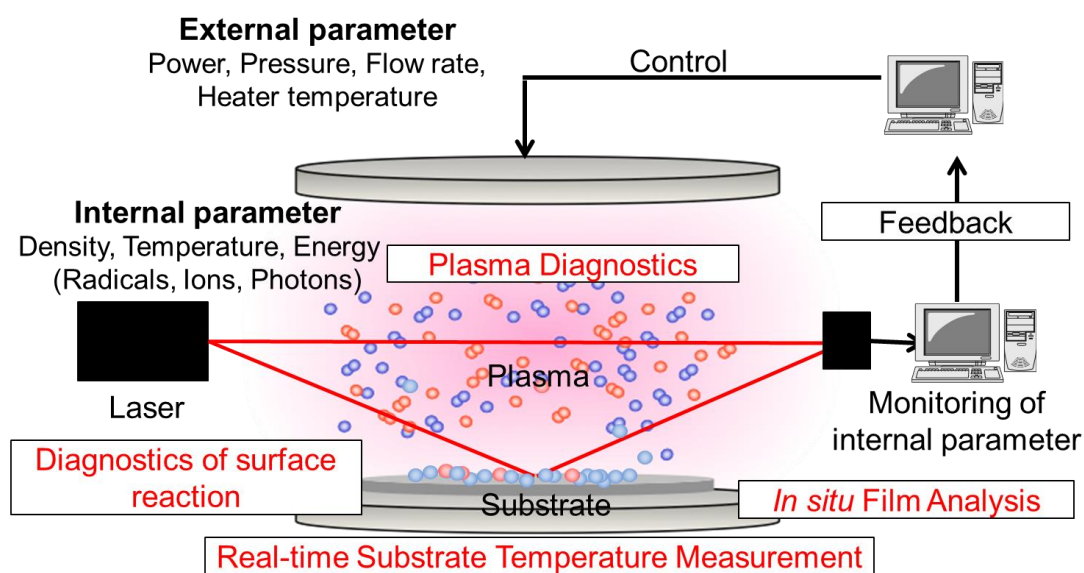


Fig. 1.3 Schematic diagram of plasma parameters. [17-19, 23]

## Chapter 1

The temperature management technology in semiconductor fabrication processes, including the monitoring or control of the Si substrate and substrate holder temperatures, is important to realize the processes with high precision and reproducibility. For example, in a plasma etching process, the etching rate and etching profile are sensitive to the Si substrate temperature.<sup>[22-26]</sup> The spatial distribution of the deposition rate, plasma chemistry, and thermal diffusion of species near the substrate holder changes depending on the local temperature of the wall or substrate holder, resulting in the non-uniform etching.<sup>[27-29]</sup> According to ITRS, the manufacturing variations of the gate electrode of MOSFET (Metal-Oxide-Semiconductor Field-Effect Transistor) must be controlled from 3 to 2 nm ( $3\sigma$ ) in the 45 nm generation and will be less than 1 nm in 20 nm generation which is scheduled in 2015. In the generation, temperature fluctuation control or autonomous radical-density control combined with precise temperature measurement less than 1 °C will be necessary. Thus, it is essential to measure the actual temperature of the substrate and all parts of a chamber accurately in many semiconductor etching processes.

Figure 1.4 shows the amount of bowing of the organic film as a function of the substrate temperature at a density ratio of  $H/(H+N) = 0.8$ .<sup>[23]</sup> The densities of hydrogen(H) and nitrogen(N) in the plasma were measured by vacuum ultra violet

absorption spectroscopy. The amount of bowing is defined as the difference between the width at the highest position or the most tapered position “B” and the width at the line at the top “A” as shown in Fig. 1.5(a). In order to meet the requirements of the etch process, it is better to reduce the size of the trench bottom “B”. Hence, if “B” is less than “A”, we always regard the data as the taper profile. The scanning electron microscopy (SEM) images of etched profile of organic film are shown in Fig. 1.5(b). The amount of bowing slightly, increased with increasing the substrate temperature as shown in Fig. 1.4. This change is important from the viewpoint of controlling the shape of side wall. Thus, the temperature measurement is important.

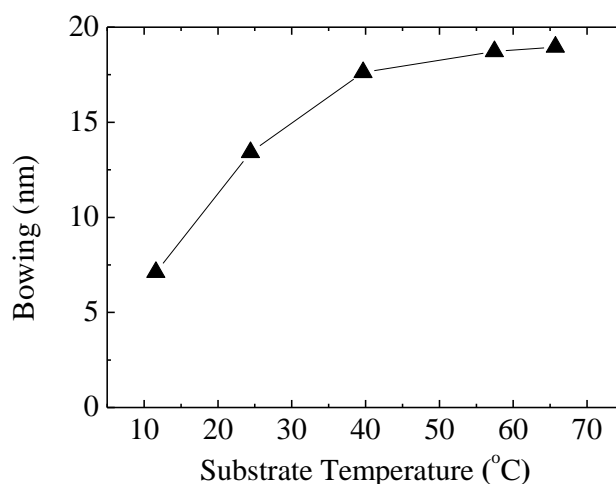
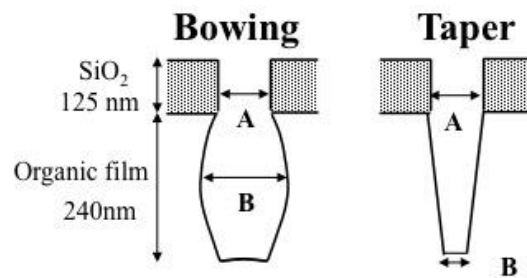
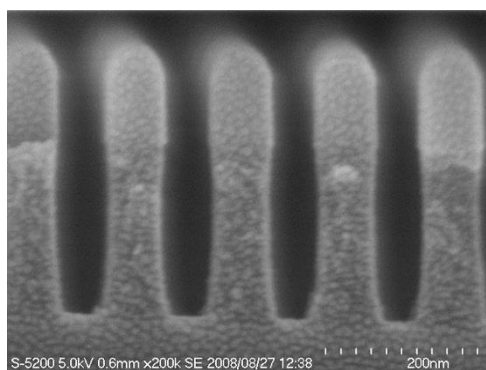


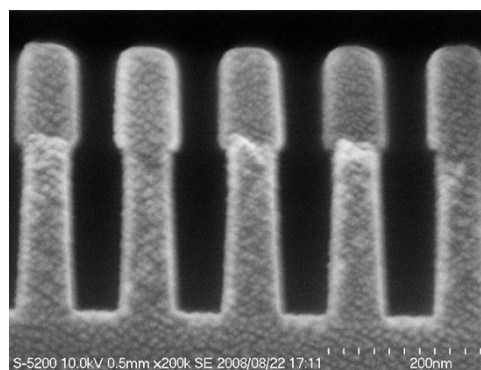
Fig. 1.4 The amount of bowing of the organic film as a function of the substrate temperature.<sup>[22]</sup>



(a)



Bowling



Taper

(b)

Fig. 1.5 Etched profile of organic film.<sup>[23]</sup>

## Chapter 1

Moreover, besides the etching process, the system will be more powerful tool in plasma enhanced plasma chemical vapor deposition (PECVD) processes. In this thesis, the system was successfully applied to carbon nanowalls (CNWs) thin-film deposited Si substrates as a PECVD process. The CNWs are one of carbon nanostructures. They comprise stacks of graphene layers standing vertically on a substrate and successfully synthesized by PECVD.<sup>[30-35]</sup> They have excellent electrical conductivity and chemical strength derived from the features of their graphene sheets. Therefore, using CNWs, it is expected to realize electronic channels, interconnects, and electrodes in logical devices, electron field emitters, catalytic electrodes of fuel cells, electric double-layer capacitors, biosensing elements, and other devices are expected to be realized using CNWs. The structure of CNWs, namely, their gap and height, are very sensitive to the substrate temperature as shown in Fig. 1.6.<sup>[36, 37]</sup> It is, therefore, essential to measure and control the substrate temperature in the CNWs synthesis processes.

Thus, the system will be applicable to various kinds of thin film deposition processes as well as CNWs and be a key tool for realizing autonomously controlled plasma etching and deposition processes.

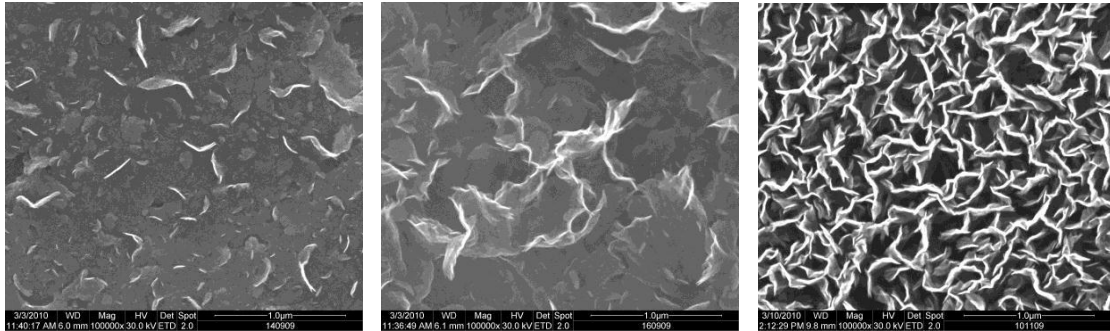


Fig. 1.6 SEM images of films deposited at various substrate temperature (I) 250 °C (II) 450 °C, (III) 665 °C. [36]

### 1.3.1 Conventional monitoring methods of substrate temperatures

There are various methods of measuring temperature during the plasma processing. [38-41] Typical methods in commercial chambers employ thermocouples, pyrometers, and optical-fiber fluorescence temperature sensors, as shown in Fig.1.7. [39, 42] However, these techniques have some problems, such as poor reliability and repeatability, and limited measurement range.

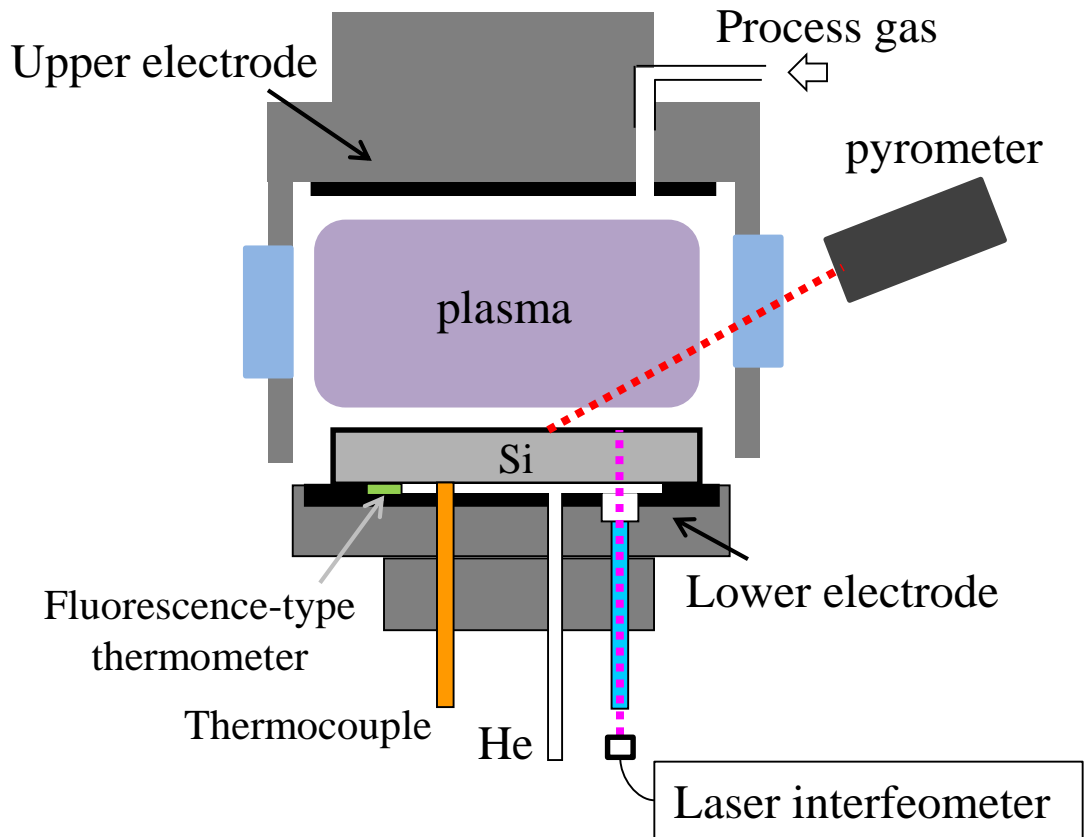


Fig. 1.7 Schematic diagram of conventional plasma etching of paratus equipped with substrate temperature monitor. <sup>[39, 42]</sup>

Heat is transferred to objects each other by emission (radiation), convection, and conduction. Temperature monitoring methods can be broadly categorized into contact and noncontact. The contact methods measure the temperature transferred to the sensing part from the measurement targets through the heat conduction and have simpler structures and cheaper than the others. On the other hand, noncontact methods measure

the infrared emission or Raman scattering from the objects or the thermal expansion in the optical path of target. Principles and problems of some conventional typical monitoring methods are presented in the next subsections.

### 1.3.1.1 Thermocouple

A thermocouple consists of two conductors of different materials that produce a voltage in the vicinity of the point where the two conductors are in contact through the Seebeck effect. The voltage is converted to the temperature. Type K (chromel –alumel) is most common general purpose thermocouple and type R (platinum–rhodium alloy) are used to 1600 °C because of its high tolerance for high temperature and oxidation and so on. The thermocouples are most commonly used in the plasma processes because of the low-price and the simple configuration. However, the efficiency of heat transfer from the measurement target to the sensor part becomes lower in the low pressure region. Figure 1.8 shows the efficiency of heat transfer  $k$  as a function of inverse of Knudsen number ( $1/Kn$ ) in the presence of various kind inert gases between the two planes with the temperature of 293 and 393 K.<sup>[43]</sup> The  $Kn$  is expressed by the following equation.

$$Kn = \frac{\lambda}{L} = \frac{k_B T}{\sqrt{2\pi\sigma^2 PL}}, \quad (1.1)$$

where  $T$  is absolute temperature (K),  $k_B$  is Boltzmann's constant,  $P$  is total pressure (Pa),

$\sigma$  is diameter of atoms,  $L$  is representative physical length,  $\lambda$  is mean free path.

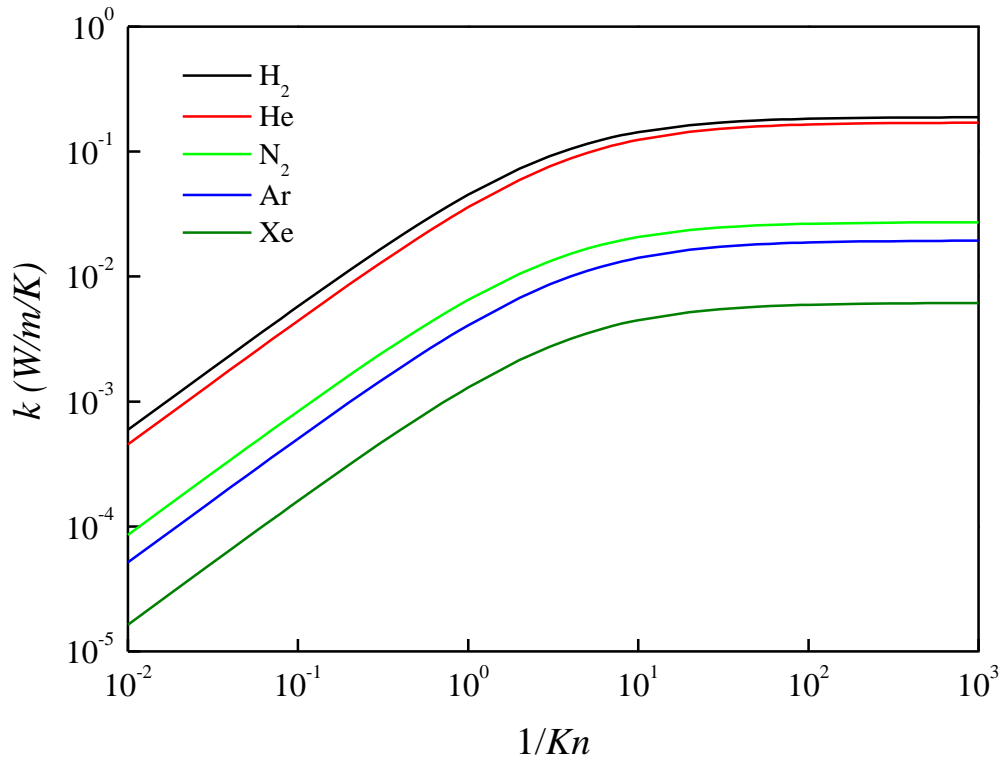


Fig. 1.8 Efficiency of heat transfer  $k$  as a function of  $1/Kn$ . <sup>[43]</sup>

The efficiency becomes lower in the  $1/Kn$  region lower than  $1/10$ , which means that the mean free path  $\lambda$  becomes larger, namely, the pressure becomes lower from eq.1.1. Therefore, contact-type thermometries are not suitable for low pressure processes because the measurement reliability depends a great deal on the condition of contacting surfaces, pressure, and kind of ambient gases. Moreover, the thermocouple is basically electric measurement, therefore, the large electric field applied to the substrate in plasma etching processes leads to large-electric noise or breakdown.

### **1.3.1.2 Fluorescent-type thermometer**

Fluorescent-type thermometer detects fluorescent light from a phosphor contacted with a measurement target. The sensor consists of light emitting diode (LED), photo diode (P.D.), and optical fibers as shown in Fig. 1.9 (a). The pulsed exiting light from LED travels to the phosphor located at the tip of the optical fiber, which is contacted to the measurement target. As shown in Fig. 1.9 (b), the fluorescent signal from the phosphor comes back to the P.D. via a dichroic mirror. The intensity of the signal at lower temperature is lower and its decay time is longer. On the other hand, they become higher and shorter, respectively, at higher temperature. From the decay time, the temperature of the phosphor can be derived.<sup>[44, 45]</sup> However, the measurable temperature

range is from 20 to 400 °C and too small to be applied in the plasma processes.

Moreover, this thermometry is basically contact type, therefore, and has the same shortcomings as thermocouple described in Section 1.3.1.1.

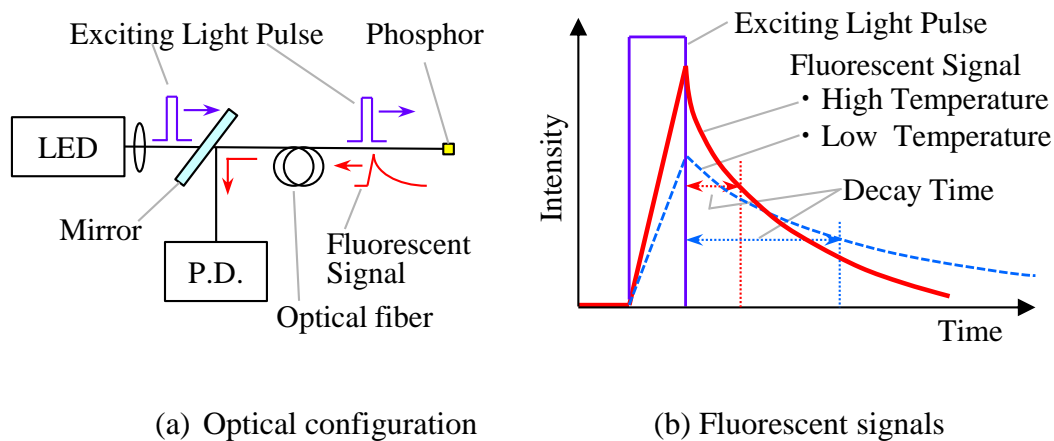


Fig. 1.9 Fluorescent-type thermometer. <sup>[44, 45]</sup>

### 1.3.1.3 Infrared radiation thermometer

Infrared radiation thermometer is one of most common noncontact thermometry and is used in industrial and clinical uses because of its simplicity and relatively low price.

It infers temperature from a portion of the thermal radiation sometimes called blackbody radiation emitted by the object being measured. Black-body radiation is the type of electromagnetic radiation within or surrounding a body in thermodynamic equilibrium with its environment, or emitted by a black body (an opaque and non-reflective body)

## Chapter 1

held at constant, uniform temperature. The radiation has a specific spectrum and intensity that depends only on the temperature of the body. The specific spectrum  $I$  is expressed by the Plank's equation as follows,

$$I(\lambda, T) = \frac{2\pi h C_0^2}{\lambda^5 (\exp(hC_0 / \lambda k T) - 1)}, \quad (1.2)$$

where  $T$  is absolute temperature,  $\lambda$  is wavelength of radiation,  $h$  is Plank's constant,  $C_0$  is the speed of light in vacuum,  $k$  is Boltzmann's constant. The specific spectrum of general objects  $I_{\lambda, T}$  becomes smaller than that of black-body by emissivity  $\varepsilon$ .

$$I_{\lambda, T} = \varepsilon I(\lambda, T), \quad (1.3)$$

where  $\varepsilon$  is the constant determined by the material, surface condition, and so on. For estimating the temperature from the spectrum, it is necessary to select the sensor with proper temperature range and to know the true values of the measurement targets. Even in Si substrates, the emissivity shows very complicate behaviors as functions of wavelength and temperature. Figure 1.10 shows the temperature and wavelength

## Chapter 1

dependences of Si emissivity.<sup>[40]</sup> From the figure, the emissivity has no dependence on temperature and wavelength in the range over 873 K, which implies that the infrared thermometry can estimate the Si substrate temperature over 873 K. However, the emissivity varies largely below 873K in the wavelength region over 1100 nm. On the other hand, the emissivity has little dependence below 873 K in the wavelength region below 1100 nm, but the specific spectrum shifts to long wavelength region and the intensity below 1100 nm becomes very low in eq. 1.2. Therefore, the infrared thermometry of Si has a critical problem for improving the measurement accuracy in the temperature region below 873 K. Moreover, in the case of the temperature measurement of the object in the vacuum chamber through a vacuum window, the emissivity is affected by the material of and the contamination on the window. In general, the infrared thermometry might lead to large temperature error in the presence of the strong background emission and higher temperature objects such as a heater in plasma processes.

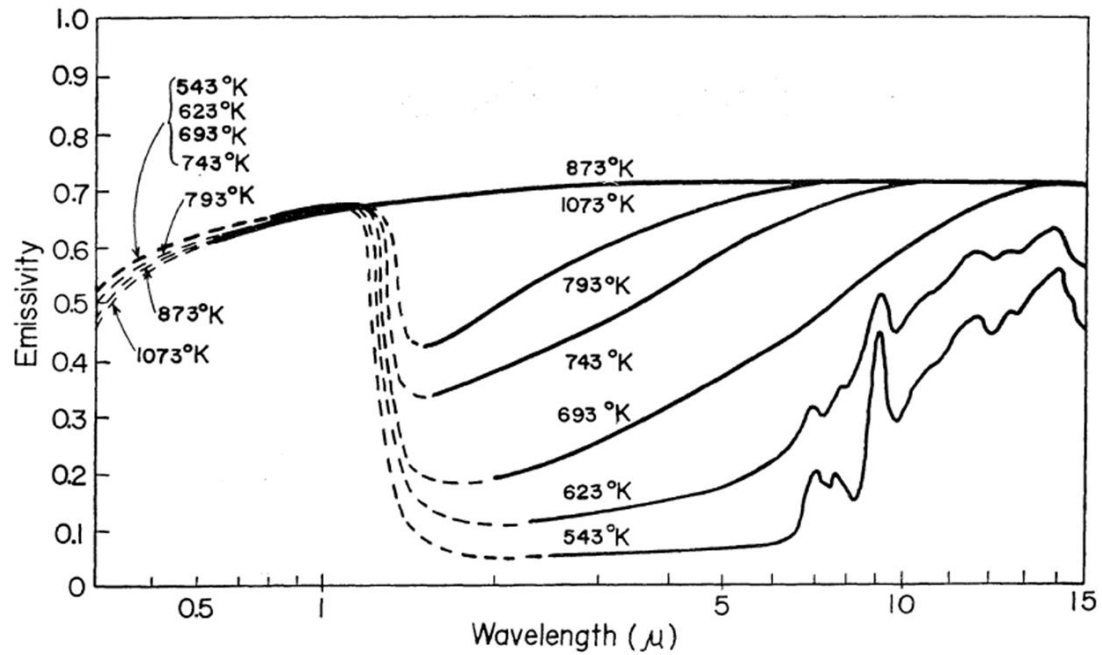


Fig. 1.10 Temperature and wavelength dependences of Si emissivity. <sup>[42]</sup>

### 1.3.1.4 Raman scattering thermometer

The Raman scattering thermometer is one of noncontact methods, and is based on the phenomena that the peak shift in Raman spectrum has temperature dependence. <sup>[46-49]</sup>

The temperature of substrate is directly derived from the shift. In the case of Si substrates, the shift is  $\pm 19$  nm and the coefficient of the shift due to the temperature is about  $0.02 \text{ cm}^{-1}/^{\circ}\text{C}$ , which is very small to detect the temperature variation of  $1^{\circ}\text{C}$  even using 1m-length large monochromator.

### **1.3.1.5 Substrate temperature monitoring using high-coherence interferometry**

The temperature monitoring of Si substrate itself was successfully measured by Donnelly et al. using a laser interferometry, namely, high-coherence interferometry in 1990.<sup>[50]</sup> They utilized the interference between reflection lights at the front and back surfaces of Si substrates. The optical path length between the front and back surfaces of Si substrate varies due to the thermal change of refractive index and physical thermal expansion. The temperature variation was derived from counting the fringes of continuous interference with the accuracy of 6.5 °C/fringe. This interferometry has merits of noncontact methods and tolerance for high electric field unlike thermocouples. However, the method cannot find the increase or the decrease in the temperature. They developed the method to distinguish between the increase and the decrease using double laser pass interferometry.<sup>[49]</sup> However, the method has shortcomings of low tolerance for mechanical vibrations because it must count the fringes continuously and fringe shifts due to vibrations are also counted and accumulated.

Kikuchi et al. developed another fringe counting method for distinguish between the increase and the decrease in temperature using pulsed laser diode in 1997.<sup>[52]</sup> According to the method, the increase or the decrease in Si substrate temperature corresponds to

the overshoot or the undershoot in the interference signal, respectively. Using this method, the counting mistake decreased, however, some counting mistakes remained for the top and bottom part of the fringe and for low-rate variation in temperature. The method also has the same difficulties of low tolerance for mechanical vibrations as mentioned above.

### **1.3.2 Problems in substrate temperature monitoring using conventional low-coherence interferometry**

The temperature monitoring method for multilayered substrate such as Si/SiO<sub>2</sub>/Si was developed using low-coherence interferometry (LCI) by Takeda et al. in 2004.<sup>[53]</sup> The principle is described in detail in Section 2.2. The method derives the optical path length between the front and rear surfaces of Si substrate from the peak positions of interference waveforms, therefore, there is no problem such as the accumulation of counting errors occurred in the continuous fringe-counting method employed in the high-coherence interferometry.

The noncontact measurement of the temperature of a Si substrate was demonstrated using the LCI during silicon dioxide (SiO<sub>2</sub>) plasma etching in a dual-frequency capacitively coupled Ar/C<sub>4</sub>F<sub>8</sub>/O<sub>2</sub> plasma by Koshimizu et al.<sup>[54]</sup> The Si temperature is

## Chapter 1

determined from the change in the optical path length between the interference waveforms of the front and back surfaces since the optical path length is changed by thermal expansion and variation in the refractive index depending on the Si substrate temperature. LCI has many advantages such as temperature measurement of the substrate itself, real-time response, wide measurement range, widely applicable plasma conditions, and high measurement accuracy. In the LCI, measurement accuracy and the minimum measurable thickness of a substrate depend on the coherent length of the light source. The coherent length of a typical superluminescent diode (SLD) with a wavelength of  $1.55\ \mu\text{m}$  and a FWHM of  $0.05\ \mu\text{m}$ , which is a typical light source for LCI, is about  $21.2\ \mu\text{m}$ . In low-coherence interferometry, a broadband light source is the key component. The maximum resolving power of the optical path length of the medium in low-coherence interferometry depends on the coherent length, which is defined by the spectrum profile and wavelength of the light source. The interferences at the front and back interfaces of the medium are combined into an overlapping interference when the optical path length of the medium is shorter than the coherence length of the light source. Then, the position of the overlapping interference is shifted from the actual position of the interface, resulting in an error in the measured temperature.

As described in Section 1.2, supercontinuum light (SC), which has a wide band spectrum, was firstly reported by Alfano and Shapiro, who used millijoule light pulses.<sup>[53]</sup> Recently, a low-noise, ultraflat, and highly coherent supercontinuum in an all fiber system has been generated using ultrashort laser pulses and optical fibers.<sup>[56-62]</sup> The SC has a broader spectrum than SLDs, resulting in having a coherent length of typically 3 to 7  $\mu\text{m}$ , which is shorter than that of SLDs (typically 20  $\mu\text{m}$ ). Thus, through the use of SC, the improvement of temperature measurement accuracy is expected.

### **1.4 High-Sensitive Monitoring for Biomaterials**

Recent progress in biological and medical field has been remarkable such as a development of induced pluripotent stem cell. In these fields, it is basic and indispensable procedure to analyze chemical composition of biomaterials, which usually consist of organic compounds.

One of the best ways to determine the composition of an organic compound is through the functional groups present in it, for example: aldehyde, amine, carboxyl, ester, halide, ketone, thionyl, and so on. There are several spectroscopic techniques used for characterizing functional groups such as: Ultra violet (UV)-Visible, Nuclear

## Chapter 1

Magnetic Resonance, and Mass Spectrometry. Infrared (IR) spectroscopy is one of these fundamental techniques.

Molecules are in constant motion, producing vibrations, such as bond stretching and bending. There are symmetric and asymmetric stretches and bends, and bending vibrations can be either in-plane or out-of-plane vibrations.

When the frequency of incoming IR radiation matches the frequency of the vibrations, energy is absorbed by the vibrating bonds. This causes the bonds to stretch and bend a bit more. In other words, the absorption of energy increases the amplitude of the vibration but does not change its frequency. This change in amplitude can be seen in an IR spectrum as a peak at the frequency of the chemical bond that absorbed the energy.

Conventional IR-Spectroscopy measurements are performed in solvents like chloroform, mineral oils, and so on. However, it is impossible to perform this analysis in the usual absorbance mode for samples that cannot transmit light such as opaque films or surfaces of solid samples. In these cases, the attenuated total reflectance (ATR) or infrared reflection absorption spectroscopy (IRRAS) mode of IR spectroscopy can be applied.

## Chapter 1

The absorptions observed in the near-infrared region ( 770 - 2500 nm ) are overtones or combinations of the fundamental stretching bands which occur in the 3000 - 6000 nm region. The bands involved are usually due to C-H, N-H or O-H stretching. The resulting bands in the near infrared are usually weak in intensity and the intensity generally decreases by a factor of 10 from one overtone to the next. The bands in the near infrared are often overlapped, making them less useful than the mid-infrared region for qualitative analysis.

However, there are important differences between the near-infrared positions of different functional groups and these differences can often be exploited for quantitative analysis.

Moreover, biomaterial samples are usually precious and their volumes are very small. Therefore, the high-sensitive monitoring or analytical tools are requested in the biological and medical fields.

Cavity ring-down spectroscopy (CRDS) is an extremely sensitive spectroscopic technique that is based on light absorption and has been applied for the measurement of weak optical transitions and low number densities in varying phases and structures such as gas, liquid, thin films, biomolecule and so on.<sup>[63, 64]</sup> The CRDS utilizes the light-intensity decay time or ring-down time of a high-finesse optical cavity as the

absorption-sensitive observable. Typically, the optical cavity is constructed using two ultrahigh-reflective coated mirrors that have appropriate spacing and radii of curvature to form a stable resonator as shown in Fig. 1.11. If the entrance mirror of the cavity has a reflectivity of  $R$ , a fraction  $(1-R)$  of light incident on the mirror is transmitted through it to enter the cavity. The transmitted light bounces back and forth between the two mirrors, losing  $(1-R)$  at each reflection. The intensity of the transmitted light for the rear mirror,  $I$ , is presented as follows:

$$I(t) = I_0 \exp\left[-(1-R)\frac{c_0 t}{L}\right] \quad (1.4)$$

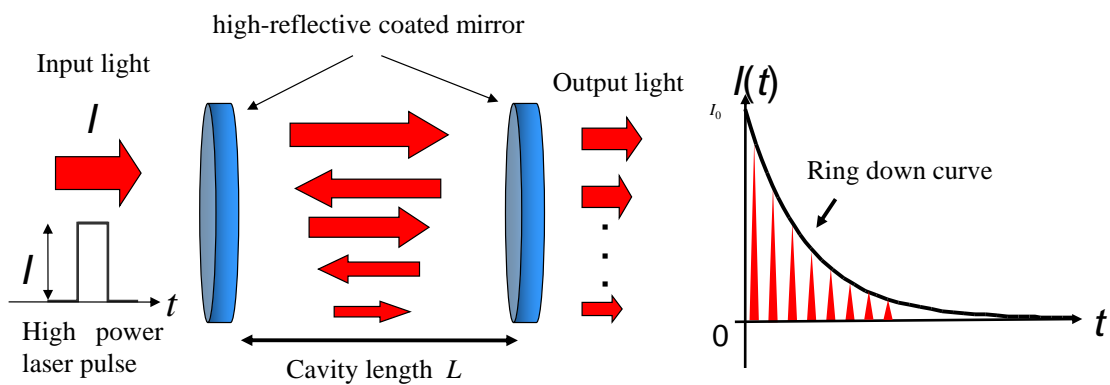


Fig. 1.11 Cavity ring-down spectroscopy. <sup>[63]</sup>

## Chapter 1

Here,  $I_0$  is the intensity of incident light;  $L$ , the length of the cavity;  $t$ , the time; and  $c_0$ , the speed of light. Light leaking out of the cavity after each incidence results in an exponential decay of light intensity, and the time taken for this intensity to decay up to is called the ring-down time ( $\tau_0$ ). When an absorber is present in the cavity, the ring-down time becomes shorter ( $\tau$ ). The concentration of sample can be directly derived from the measured  $\tau_0$  and  $\tau$  using the Lambert-Beer law as follows:

$$C = \frac{L}{c_0 \varepsilon(\lambda) d} \left( \frac{1}{\tau} - \frac{1}{\tau_0} \right) \quad (1.5)$$

Here,  $\varepsilon$  is the absorption coefficient of the sample and  $d$  is absorption length. Optical-Fiber Type cavity ring-down spectroscopy is a powerful technique suitable for very small liquid samples. The conventional types are shown in Fig. 1.12 (a) Fiber Bragg Grating type and (b) optical fiber coupler type. They are based on measurements of the ring-down time of laser intensity in a loop made of optical waveguide material.

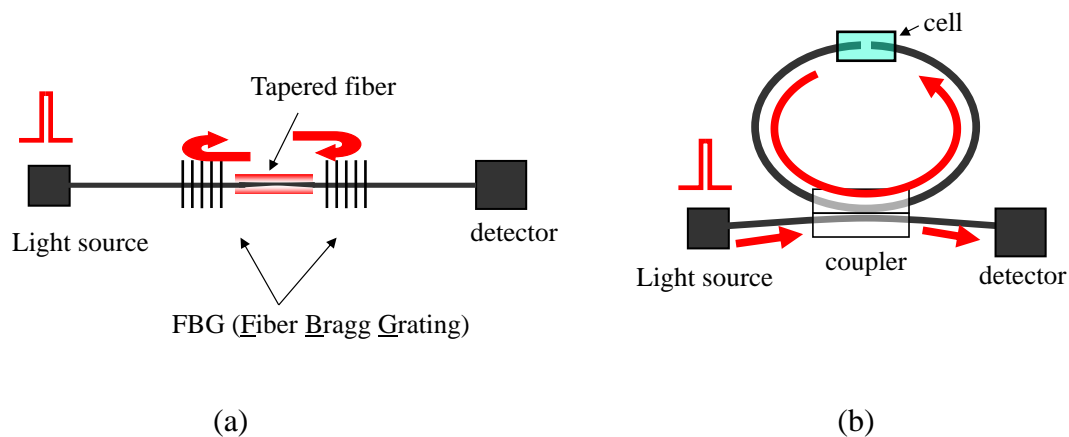


Fig. 1.12 Optical fiber-type CRDS. (a) Fiber Bragg Grating and tapered fiber<sup>[67]</sup> (b) coupler cavity and the gap between the fibers<sup>[70]</sup>

This ring-down time changes as small liquid samples containing absorbing species are introduced into the loop. Fiber and fiber components are designed to confine the signal light inside the fiber core with smaller loss in comparison with the conventional CRDS with high reflective mirrors due to elimination of the loss of the optical component. Various cavities of Optical-Fiber Type CRDS were reported as side-coupled into the core of the fiber with laser pulse<sup>[65, 66]</sup>, fiber Bragg grating<sup>[67, 68]</sup>, the gap between the fibers<sup>[69,70]</sup>, evanescent waveguide using prism<sup>[71,72]</sup> or tapered fiber<sup>[73]</sup>. Evanescent-waveguide cavity using tapered fiber eliminates the loss owing to the

coupling between laser pulse and cavity and realizes the high sensitivity measurement system.

Generally, high power laser having single-wavelength or narrow bandwidth, such as the tunable dye laser or the laser diode, has been used as a light source; cavity mirrors also cover a narrow bandwidth owing to ultrahigh reflection. Hence, when such lasers or mirrors are employed in a large measurement system or with several light sources of different wavelength, absorption spectra are achieved. As described in Section 1.2, compact, wavelength-tunable, ultra-short pulse light sources from 1.55 to 2.0  $\mu\text{m}$  have been demonstrated using femtosecond pulse laser and nonlinear fibers.<sup>[74-78]</sup> As the fiber input power is increased, the center wavelength of the generated soliton pulse is red-shifted continuously and monotonously. The generated pulses are clear  $\text{sech}^2$ -shaped ultra-short soliton light pulses. Thus, the wavelength can be changed by the intensity-modulation of femtosecond pulse laser and the absorption spectrum is obtained easily with no optical loss.

## 1.5 Purpose and Composition of This Thesis

The aim of this thesis is to extend the application of wavelength-tunable ultrashort-pulse laser and SC light to the accurate monitoring of substrate temperature during plasma processing under the new concept shown in Fig. 1.13. Application of wavelength-tunable ultrashort-pulse laser to the high-sensitive monitoring of biomaterials is also performed.

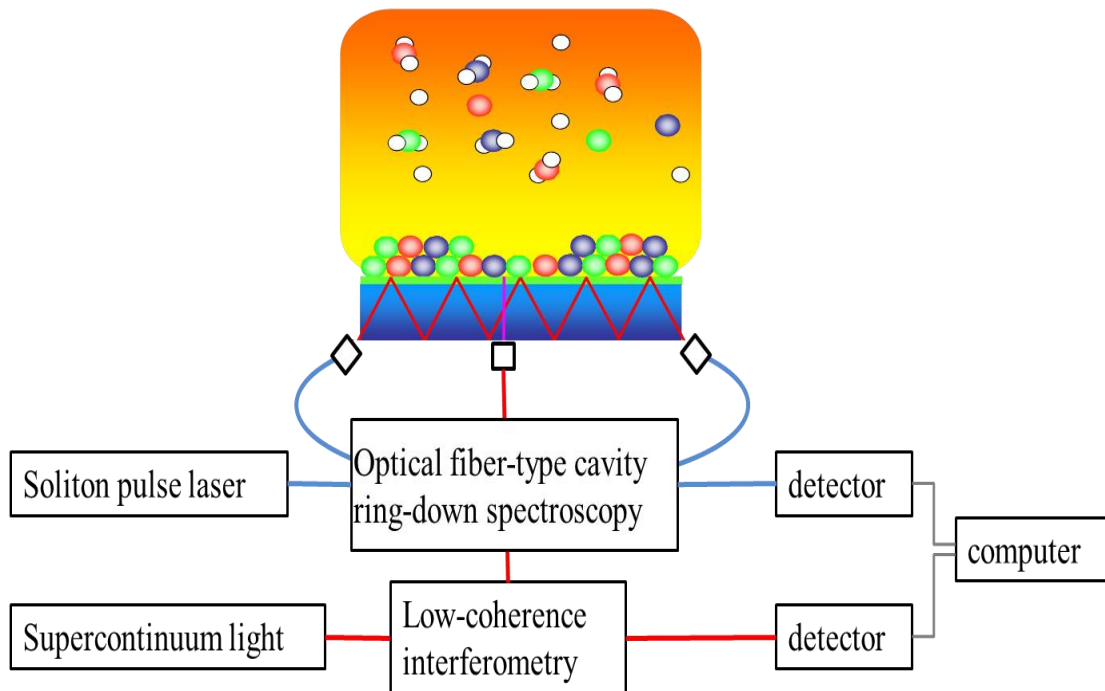


Fig. 1.13 Schematic diagram of the application of wavelength-tunable ultrashort-pulse laser and supercontinuum to the monitoring of plasma processing

## Chapter 1

The composition of this thesis is as follows;

In Chapter 2, the principles of low coherence interferometry, substrate temperature measurement, and cavity ring-down spectroscopy are presented.

In Chapter 3, a new technique for a high-resolution temperature measurement of Si wafer using optical low-coherence interferometer employing SC is proposed. To employ SC for in the interferometer, the wavelength-dispersion of SC on Si wafer is compensated using a Si mirror as a reference mirror. The simultaneous measurement of SiO<sub>2</sub> and Si temperatures on SiO<sub>2</sub>/Si substrate using the SC interferometer is demonstrated.

In Chapter 4, temperature measurements of Si substrate with CNWs layer using optical low-coherence interferometer employing SC and superluminescent diodes (SLDs) were demonstrated. The wavelength dependence on the optical path length, that is refractive index, was investigated by using SC and three SLDs having different wavelengths.

In Chapter 5, a novel optical-fiber-type broadband cavity ring-down spectroscopy system that employs wavelength-tunable ultrashort-pulse light is proposed. The high-sensitive absorption spectroscopy of glucose as a biomaterial was demonstrated in

## Chapter 1

the wavelength region from 1620 to 1690 nm by varying the wavelength using a wavelength-tunable ultrashort pulse light.

Finally, the content of this thesis is summarized and the future outlook is described in Chapter 6.

## References for Chapter 1

- [1] Irl N. Duling III, *Opt. Lett.*, **16**, 539 (1991).
- [2] H. Lim, F. Ö. Ilday, and F. W. Wise, *Opt. Lett.*, **28**, 660 (2003).
- [3] F. Ö. Ilday, H. Lim, J. R. Buckley, and F. W. Wise, *Opt. Lett.*, **28**, 1362 (2003).
- [4] F. Ö. Ilday, J. R. Buckley, L. Kuznetsova, and F. W. Wise, *Opt. Exp.*, **14**, 3550 (2003).
- [5] N. Nishizawa and T. Goto, *IEEE Photon. Technol. Lett.*, **11**, 325 (1999).
- [6] F. M. Mitschke and L. F. Mollenauer, *Opt. Lett.*, **11**, 659 (1986).
- [7] J. P. Gordon, *Opt. Lett.*, **11**, 662 (1986).
- [8] T. Hori, N. Nishizawa, H. Nagai, M. Yoshida, and T. Goto, *IEEE Photon. Technol. Lett.*, **13**, 13 (2001).
- [9] N. Nishizawa, R. Okamura, and T. Goto, *Jpn. J. Appl. Phys.*, **39**, L409 (2000).
- [10] R. R. Alfano, S. L. Shapiro, *Phys. Rev. Lett.*, **24**, 584 (1970).
- [11] I. Hartl, X. D. Li, C. Chudoba, R. K. Ghanta, T. H. Ko, J. G. Fujimoto, J. K. Ranka, and R. S. Windeler, *Opt. Lett.*, **26**, 608 (2001).
- [12] K. Isobe, W. Watanabe, S. Matsunaga, T. Higashi, K. Fukui and K. Itoh, *Jpn. J. Appl. Phys.*, **44**, L167 (2005).
- [13] Th. Udem, R. Holzwarth and T. W. Hänsch, *Nature*, **416**, 233 (2002).

## Chapter 1

- [14] H. Takara, T. Ohara, K. Mori, K. Sato, E. Yamada, Y. Inoue, T. Shibata, M. Abe, T. Morioka, and K. I. Sato, *Electron, Lett.*, **36**, 2089 (2000).
- [15] J. K. Ranka, R. S. Emdeler, and A. J. Stentz, *Opt. Lett.*, **25**, 25 (2000).
- [16] N. Nishizawa and T. Goto, *Jpn. J. Appl. Phys.*, **40**, L365 (2001).
- [17] International Technology Roadmap for Semiconductors, <http://www.itrs.net/>
- [18] M.Hori and T.Goto, *Appl. Surf. Sci.*, **192**, 135 (2002).
- [19] H.Nagai, S.Takashima, M.Hiramatsu, M.Hori, T.Goto, *J. Appl. Phys.*, **91**, 2615 (2002).
- [20] M. Hori and T. Goto, *Appl. Surf. Sci.*, **253**, 6657 (2007).
- [21] S. Takahashi, R. Kawauchi, S. Takashima, S. Den, T. Katagiri, H. Kano, T. Ohta, M.i Ito, T. Suzuki, K. Takeda, and M. Hori, *Jpn. J. Appl. Phys.*, **51**, 076502 (2012).
- [22] H. Yamamoto, 2011. Studies on Plasma Etching Process of Low Dielectrics for Fine Pattern Profile Control with Less Damage. PhD Thesis, Nagoya University.
- [23] H. Yamamoto, H. Kuroda, M. Ito, T. Ohta, K. Takeda, K. Ishikawa, H. Kondo, M. Sekine, and M. Hori, *Jpn. J. Appl. Phys.*, **51**, 016202 (2012).
- [24] H. Abe, M. Yoneda, and N. Fujiwara, *Jpn. J. Appl. Phys.*, **47**, 1435 (2008).

## Chapter 1

- [25] T. Ohiwa, K. Horioka, T. Aricado, I. Hasegawa, and H. Okano, *Jpn. J. Appl. Phys.*, **31**, 405 (1992).
- [26] M. Hori, H. Kuroda, M. Ito, T. Ohta, K. Takeda, and M. Sekine, *Proc. 19th Int. Symp. on Plasma Chemistry*, **O6.1** (2009).
- [27] H. Sugai, K. Nakamura, Y. Hikosaka, and M. Nakamura, *J. Vac. Sci. Technol. A* **13**, 887 (1995).
- [28] M. Schaepkens, R. C. M. Bosch, T. E. F. M. Standaert, G. S. Oehrlein, and J. M. Cook, *J. Vac. Sci. Technol. A*, **16**, 2099 (1998).
- [29] Y. Hikosaka, M. Nakamura, and H. Sugai, *Jpn. J. Appl. Phys.*, **33**, 2157 (1994).
- [30] H. Watanabe, H. Kondo, M. Sekine, M. Hiramatsu, and M. Hori, *Jpn. J. Appl. Phys.*, **51**, 01AJ07 (2012)
- [31] S. Kondo, H. Kondo, M. Hiramatsu, M. Sekine, and M. Hori, *Appl. Phys. Exp.*, **3**, 045102 (2010).
- [32] W. Takeuchi, H. Kondo, T. Obayashi, M. Hiramatsu, and M. Hori, *Appl. Phys. Lett.*, **98**, 123107 (2011)
- [33] W. Takeuchi, M. Ura, M. Hiramatsu, Y. Tokuda, H. Kano, and M. Hori, *Appl. Phys. Lett.*, **92**, 213103 (2008).

## Chapter 1

- [34] W. Takeuchi, K. Takeda, M. Hiramatsu, Y. Tokuda, H. Kano, S. Kimura, O. Sakata, H. Tajiri, and M. Hori, *Phys. Status Solidi A*, **207**, 139 (2009).
- [35] S. Kondo, S. Kawai, W. Takeuchi, K. Yamakawa, S. Den, H. Kano, M. Hiramatsu, and M. Hori, *J. Appl. Phys.*, **106**, 094302 (2009).
- [36] J. L. Booth, B. T. Beard, J. E. Stevens, M. G. Blain, and T. L. Meisenheimer, *J. Vac. Sci. Technol. A*, **14**, 2356(1996).
- [37] S. Shiambukuro, Y. Hatakeyama, M. Takeuchi, T. Itoh, S. Nonomura, *Jpn. J. Appl. Phys.*, **47**, 11 (2008)
- [38] H. G. Jain, 2012. Synthesis and Characterization of Carbon nanowalls by ICP-CVD using Aluminium-Acetylacetonate precursor. PhD Thesis, Universität Duisburg-Essen.
- [39] A. Cardoso and A. K. Srivastava, *J. Vac. Sci. Technol. B*, **19**, 397 (2001).
- [40] J. L. Cui, K. Amtmann, J. Ristein, and L. Ley, *J. Appl. Phys.*, **83**, 7929(1998).
- [41] U. J. Gibson and M. Chernuschenko, *Opt. Expr.*, **4**, 443 (1999).
- [42] T. Sato, *Jpn. J. Appl. Phys.*, **6**, 339 (1967).
- [43] K. Denpoh, *IEEE Transactions on Semiconductor Manufacturing*, **11**, 25 (1998) .
- [44] K. T. V. Grattan, A. W. Palmer, Infrared fluorescence “decay - time” temperature sensor, *Rev. Sci. Instrumen.*, **56**, 1784 (1985).

## Chapter 1

- [45] K. A. Wickersheim, M. h. Sun, *J. Microwave Power*, **22**, 85 (1987)
- [46] J. L. Cui, K. Amtmann, J. Ristein, and L. Ley, *J. Appl. Phys.*, **83**, 7929 (1998).
- [47] M. Balkanski, R. F. Wallis, E. Haro, *Phys. Rev. B*, **28** 1928 (1983).
- [48] Hubert H. Burke and Irving P. Herman, *Phys. Rev. B*, **48**, 15016 (1993).
- [49] 中 庸行, 佐竹 司、大槻 久仁夫, 半導体プロセス向けシリコンウエハの温度計測用ラマン分光システム, 第 117 回温度計測部会 9 (2005).
- [50] V. M. Donnelly and J. A. McCaulley, *J. Vac. Sci. Technol. A*, **8**, 84 (1990).
- [51] V. M. Donnelly, *Vac. Sci. Technol. A*, **11**, 66 (1993).
- [52] Kikuchi, S. Fujimura, R. Kurosaki, H. Yano, *J. Vac. Sci. Technol. A*, **15**, 2035 (1997).
- [53] K. Takeda, Y. Tomekawa, T. Shiina, M. Ito, Y. Okamura, and N. Ishii, *Jpn. J. Appl. Phys.*, **43**, 7737 (2004).
- [54] C. Koshimizu, T. Ohta, T. Matsudo, S. Tuchitani, and M. Ito, *Appl. Phys. Expr.*, **3**, 056201 (2010).
- [55] R. R. Alfano and S. L. Shapiro, *Phys. Rev. Lett.*, **24**, 592 (1970).
- [56] N. Nishizawa and T. Goto, *Jpn. J. Appl. Phys.*, **40**, L365 (2001).
- [57] T. Hori, N. Nishizawa, T. Goto, and M. Yoshida, *J. Opt. Soc. Am. B*, **21**, 1969 (2004).

## Chapter 1

- [58] T. Hori, J. Takayanagi, N. Nishizawa, and T. Goto, *Opt. Expr.*, **12**, 317 (2004).
- [59] J. Takayanagi and N. Nishizawa, *Jpn. J. Appl. Phys.*, **45**, L441 (2006).
- [60] N. Nishizawa and J. Takayanagi, *J. Opt. Soc. Am. B*, **24**, 1786 (2007).
- [61] N. Nishizawa and M. Hori, *Appl. Phys. Exp.*, **1**, 022009(2008).
- [62] N. Nishizawa, H. Mitsuzawa, J. Takayanagi, and K. Sumimura, *J. Opt. Soc. Am. B, Opt. Phys.*, **26**, 426 (2009).
- [63] G. Berden and R. Engeln, *Cavity Ring-Down Spectroscopy, Techniques and Applications*, Wiley-Blackwell, (2009).
- [64] G. Berden, G. R. Peeters and G. Meijer, *Int. Rev. Phys. Chem.*, **19**, 565 (2000).
- [65] B. A. Gibson and C. Vallance, *Boomerang Trans.*, **1**, 26 (2006).
- [66] R. S. Brown and I. Kozin, Z. Tong, R. D. Oleschuk, and H. -P. Loock, *J. Chem. Phys.*, **117**, 10444 (2002).
- [67] M. Gupta, H. Jiao, and A. O'Keefe, *Opt. Lett.*, **27**, 1878 (2002).
- [68] S. Pu and X. Gu, *Opt. Lett.*, **34**, 1774 (2009).
- [69] N. Trefiak, J. Barnes, R. Li, Z. Tong, R. D. Oleschuk and H. -P. Loock, *Anal. Chem.*, **76**, 6594 (2004).
- [70] Z. Tong, A. Wright, T. McCormick, Runkai Li, Richard D. Oleschuk, and Hans-Peter Loock, *IEEE LEOS NEWSLETTER*, **15**, 5 (2005).

## Chapter 1

- [71] L. van der Sneppen, F. Ariese, C. Gooijer, and W. Ubachs, *Annu. Rev. Anal. Chem.*, **2**, 13 (2009).
- [72] M. H.-Zadeh, and K. J. Vahala, *Opt. Expr.*, **14**, 10800 (2006).
- [73] P. B. Tarsa, A. D. Wist, P. Rabinowitz, and K. K. Lehmann, *Appl. Phys. Lett.*, **85**, 4523 (2004).
- [74] J. Takayanagi, T. Sugiura, M. Yoshida, and N. Nishizawa, *IEEE Photon. Technol. Lett.*, **18**, 2284 (2006).
- [75] N. Nishizawa, *IEEE J. Quantum Electron*, **45**, 1446 (2009).
- [76] N. Nishizawa, R. Okamura, and T. Goto, *Jpn. J. Appl. Phys.*, **39**, L409 (2000).
- [77] N. Nishizawa, and K. Takahashi, *Opt. Lett.*, **36**, 3780 (2011).
- [78] N. Nishizawa, R. Okamura, and T. Goto, *Jpn. J. Appl. Phys.*, **38**, 4768 (1999).

# Chapter 2

## Principles of Measurement Methods

### 2.1 Introduction

In this chapter, the principles of measurement methods performed in this study are described. Temperature measurement and high-sensitive absorption measurement are based on the low-coherence interferometry and cavity ring-down spectroscopy, respectively.

### 2.2 Substrate Temperature Measurement

#### 2.2.1 Michelson interferometry

Figure 2.1 shows the schematic of the Michelson interferometer. Light from the source is divided into reference and sample beams at a beam splitter. Light reflected from the reference and sample mirrors are recombined at the beam splitter and propagate in a detector. If the light is perfectly coherent, then reflected lights from the reference and sample mirrors produce a sum of the monochromatic electronic field components  $E_s$  and  $E_r$  at the detector. These field expressed by

$$E_s(r, t) = A_s \exp\{-j(k_0 l_s - \omega_0 t)\}, \quad (2.1)$$

## Chapter 2

$$E_r(r, t) = A_r \exp \{-j(k_0 l_r - \omega_0 t)\}, \quad (2.2)$$

where  $A$  is the optical amplitude,  $\omega_0$  is the optical frequency of the light, and  $k_0$  is the wavenumber. The  $l_s$  and  $l_r$  are the optical path lengths from beam splitter to the reference and to the sample mirror, respectively.

In general, the time-averaged photocurrent  $i_d$  is given by

$$i_d = \langle |E_d|^2 \rangle = \langle |E_s + E_r|^2 \rangle = i_{dc} + \tilde{i}_d, \quad (2.3)$$

$$i_{dc} = \frac{A_s^2 + A_r^2}{2}, \quad (2.4)$$

$$\tilde{i}_d = A_s A_r \cos(2k_0 \Delta l), \quad (2.5)$$

where  $\Delta l = l_r - l_s$  is optical path difference between the reference and sample optical path lengths.  $i_{dc}$  is the direct current (DC) offset term and  $\tilde{i}_d$  is the variation of the photocurrent. Equation (2.5) shows that the photocurrent contains a sinusoidally varying term representing the interference between the reference and sample fields. The interference has a period of  $1/2$  relative to the length  $\Delta l$ . The example of interference waveform of coherent light is shown in Fig. 2.2(a).

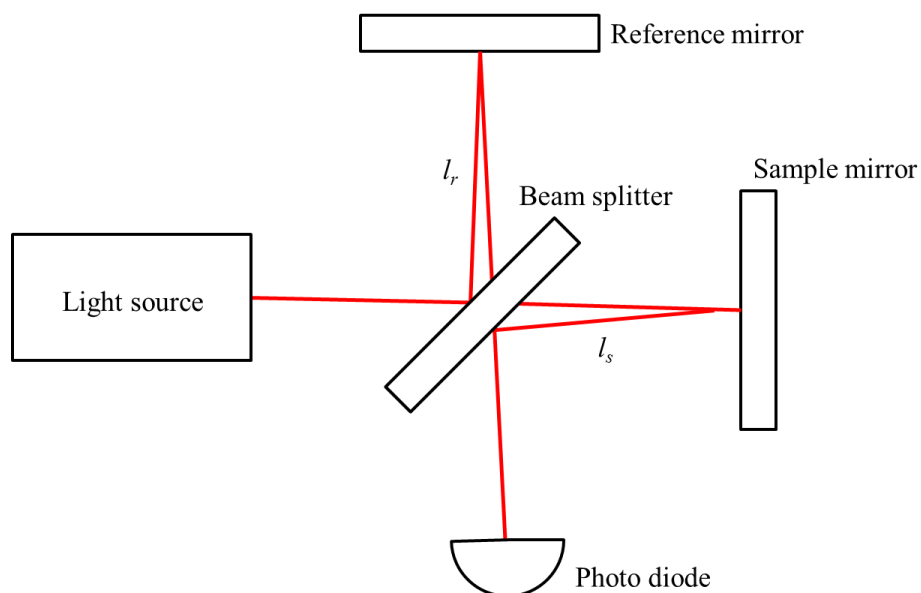
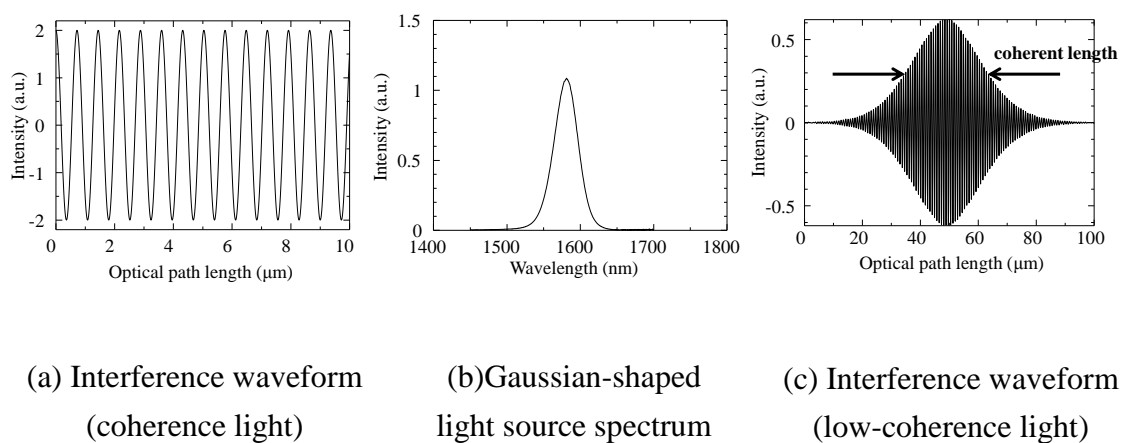


Fig. 2.1 Michelson interferometry.



(a) Interference waveform  
(coherence light)

(b) Gaussian-shaped  
light source spectrum

(c) Interference waveform  
(low-coherence light)

Fig. 2.2 Interference waveform.

## 2.2.2 Low-Coherence Interferometry

In the low-coherence interferometry (LCI), the light source has the electric field amplitude  $s(k, \omega)$  as a function of the wavenumber  $k = 2\pi/\lambda$  and angular frequency  $\omega = 2\pi\nu$ , which are respectively the spatial and temporal frequencies of each spectral component of the field having wavelength  $\lambda$ . A Gaussian-shaped light source spectrum as shown in Fig. 2.2(b) is convenient to use in modeling LCI because it approximates the shape of actual light sources. The normalized Gaussian function  $S(k) = \langle |s(k, \omega)|^2 \rangle$  is substituted, which encodes the power spectrum dependence of the light source. The power spectrum  $S(k)$  is given by

$$S(k) = \frac{2\sqrt{\ln 2}}{\Delta k \sqrt{\pi}} \exp \left\{ - \left[ \frac{k - k_0}{\left( \frac{\Delta k}{2\sqrt{\ln 2}} \right)} \right]^2 \right\}, \quad (2.6)$$

where  $k_0$  is the central wavenumber of the light source spectrum and  $\Delta k$  is its spectral bandwidth, corresponding to the half-width of the spectral 1/e of its maximum. The interference term is described as

$$\begin{aligned} I(\Delta l) &= \int_0^\infty S(k) \exp \{ -jk \cdot 2\Delta l \} dk \\ &= \exp \left\{ - \left[ \frac{\Delta l}{\frac{2\sqrt{\ln 2}}{\Delta k}} \right]^2 \right\} \cos(2k_0 \Delta l) \end{aligned} \quad (2.7)$$

The coherence length of the light source  $l_c$  is an explicit function of the light source bandwidth and stated both in wavenumber and wavelength term as

$$l_c = \frac{4 \ln 2}{\Delta k} = \frac{2(\ln 2)\lambda_0^2}{\pi\Delta\lambda}, \quad (2.8)$$

where  $\lambda_0 = 2\pi/k_0$  is the center wavelength of the light source and  $\Delta\lambda$  is its wavelength bandwidth defined as the full width of half maximum (FWHM) of its wavelength spectrum. The example of interference waveform of low-coherence light is shown in Fig. 2.2(c).

Figure 2.3 shows the waveform of the low-coherence interferometry in the case of (a) Si and (b) SiO<sub>2</sub>/Si substrates. When the electric fields of the reflected light from the sample and reference arm interfere at a detector, the interference term of the interference intensity is given by<sup>[1]</sup>

$$I(\Delta l) = E_1 E_2 \sqrt{R} \cos(2k_0 \Delta l), \quad (2.9)$$

where  $E_1$  and  $E_2$  are the electric fields of the sample and reference arms, respectively.  $\Delta l$  is the optical path difference ( $\Delta l = 0$  defines the SiO<sub>2</sub>/Si interface position),  $k_0$  is the center wave number of the light source, and  $R$  is the reflectance of the medium (the reflectance of the mirror is assumed to be 100 %). Assuming a light source with a broadband spectrum, the interference intensity is given by

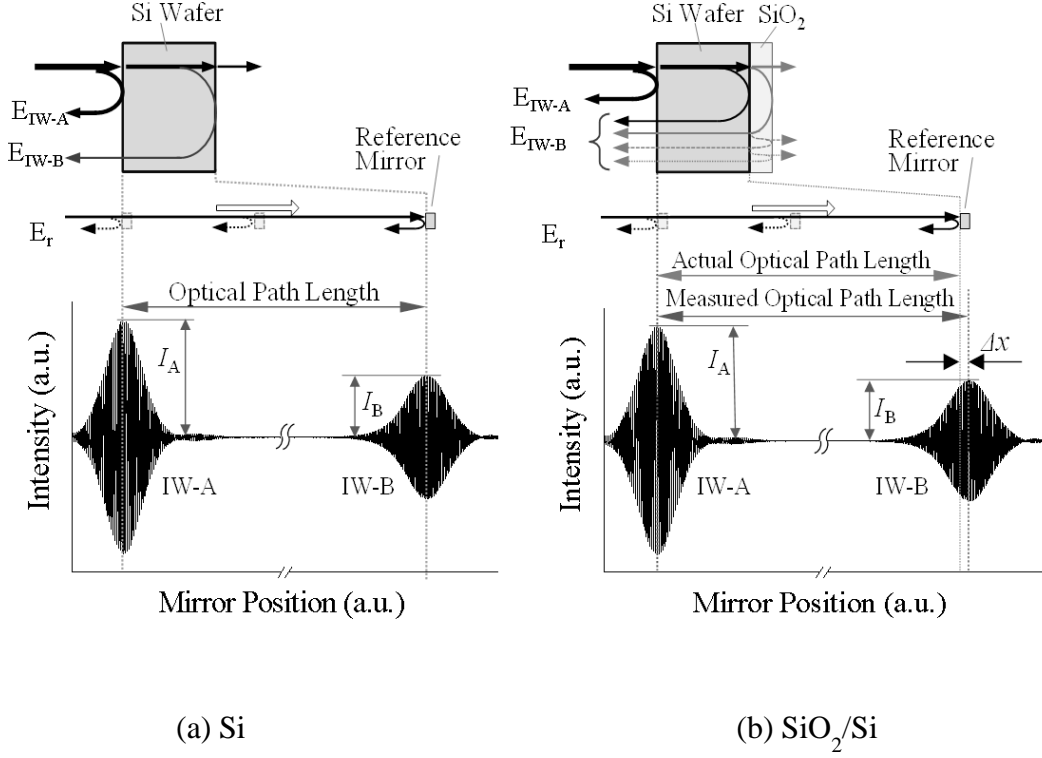


Fig. 2.3 Interference signals with mirror and sample.

$$I(\Delta l) = \int E_1 E_2 \cos \sqrt{R} (2k_0 \Delta l) S(k) dk, \quad (2.10)$$

where  $S(k)$  is the power spectral density of the light source. When the incident light to the sample is reflected many times at the SiO<sub>2</sub>/air and SiO<sub>2</sub>/Si interfaces, the total amplitude reflection coefficient  $\rho$  is given by

$$\rho = \frac{\rho_2 + \rho_1 \exp(-i2\delta)}{1 + \rho_1 \rho_2 \exp(-i2\delta)}, \quad (2.11)$$

$$\delta = kn_{SiO_2} d_{SiO_2}, \quad (2.12)$$

where  $\delta$  is the phase difference between the reflections at the SiO<sub>2</sub>/Si and SiO<sub>2</sub>/air

## Chapter 2

interfaces,  $d_{\text{SiO}_2}$  is the  $\text{SiO}_2$  thickness, and  $n_{\text{SiO}_2}$  is the refractive index of  $\text{SiO}_2$ .  $\rho_1$ , the Fresnel reflection coefficient at the  $\text{SiO}_2/\text{air}$  interface, is given by

$$\rho_1 = \frac{n_{\text{SiO}_2} - n_{\text{air}}}{n_{\text{SiO}_2} + n_{\text{air}}}, \quad (2.13)$$

and  $\rho_2$ , the Fresnel reflection coefficient at the  $\text{Si}/\text{SiO}_2$  interface, is given by

$$\rho_2 = \frac{n_{\text{Si}} - n_{\text{SiO}_2}}{n_{\text{Si}} + n_{\text{SiO}_2}}, \quad (2.14)$$

where  $n_{\text{Si}}$  and  $n_{\text{air}}$  are the refractive indexes of Si and air, respectively. The coefficients of eqs. (2.13) and (2.14) were calculated from the refractive indexes reported in the literature.<sup>[2-6]</sup> Using eq. (2.11), the reflectance ( $R$ ) and the phase difference ( $\varphi$ ) at the  $\text{SiO}_2/\text{Si}$  interface are given by

$$R(k, d_{\text{SiO}_2}) = \frac{\rho_1^2 + \rho_2^2 + 2\rho_1\rho_2 \cos 2\delta}{1 + \rho_1^2\rho_2^2 + 2\rho_1\rho_2 \cos 2\delta}, \quad (2.15)$$

$$\varphi(k, d_{\text{SiO}_2}) = \tan^{-1} \frac{\rho_1(\rho_2^2 - 1)\sin 2\delta}{\rho_2(1 + \rho_1^2) + \rho_1(1 + \rho_2^2)\cos 2\delta}. \quad (2.16)$$

Taking the multiple reflections into account, the overlapping interference waveform at the  $\text{SiO}_2/\text{Si}$  interface (IW-B) becomes

$$I(\Delta l) = \int E_1 E_2 \sqrt{R(k, d_{\text{SiO}_2})} \cos\{2k\Delta l + \varphi(k, d_{\text{SiO}_2})\} S(k) dk . \quad (2.17)$$

This equation indicates that the interference intensity depends on the optical path difference, the wavelength of the light source, and the SiO<sub>2</sub> thickness, which means that the SiO<sub>2</sub> thickness can be determined by measuring the overlapping interference intensity ( $I_B$ ). IW-B, which was calculated by eq. (2.17), is shown in Fig. 2.3(b). When the light is scattered at surface or interface of substrate, the interference intensity becomes smaller due to decrease in the  $E_1$  in eq. (2.17). Moreover, the light is absorbed by media so that the interference intensity becomes smaller. However, the shape of the interference waveform is not varied due to no change in the phase difference in eq. (2.17).

### 2.2.3 Theory of Substrate Temperature Measurement

The substrate temperature was calculated from the change of optical thickness of media measured by an optical fiber-type low-coherence interferometer. Schematic diagram of temperature measurement system is shown in Fig. 2.4. The measurement system is based on a Michelson interferometer, which consists of a super luminescent diode (SLD), a scanning reference mirror, a collimation lens, an optical fiber and so on. The SLD light is divided into two beams by the fiber coupler. One beam irradiates the substrate. The other beam goes to a scanning reference mirror. In the substrate, the SLD light is reflected on the substrate backside and surface. In the scanning reference mirror scanner side, the reference-optical-path length is changed by moving reference the mirror. The lights reflected at the substrate go back to the fiber coupler through the fiber

collimator, and then interfered with the light reflected at the scanning reference mirror within the range of coherence length. The position of interferogram was changed by the thermal expansion and the change of refractive index with increasing the substrate temperature.

The change of temperature was measured by the shift of the peak position of interferogram. By using this measurement system, we can measure the substrate temperature in the real time.<sup>[7, 8]</sup>

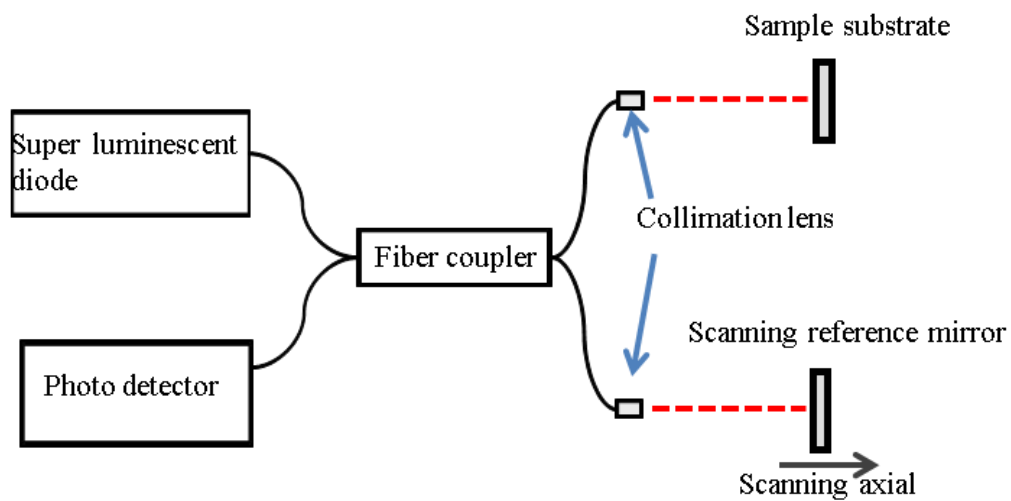


Fig. 2.4 Schematic diagram of simplified substrate temperature measurement system.

The optical-path length  $L$  of a certain substance is

$$L = n(\lambda) \cdot d, \quad (2.19)$$

where  $n$  is the index of refraction and  $d$  is the thickness of the substance. The SLD used in this article has a 48-nm bandwidth at the central wavelength of 1.55  $\mu\text{m}$ . Under these conditions, the effect of group index on the interference signal was negligibly small. Therefore, we can discuss the principle without the effect. If the temperature of the substance varies from  $T$  to  $T + \Delta T$ , the index of refraction and the thickness vary as follows;

$$d \rightarrow d(1 + \alpha\Delta T), \quad (2.20)$$

$$n(\lambda) \rightarrow n(\lambda)(1 + \beta(\lambda)\Delta T), \quad (2.21)$$

where  $\alpha$  and  $\beta(\lambda)$  are the coefficients of thermal expansion and the temperature dependence of the refractive index, respectively.  $\alpha$  is independent of optical wavelength while  $\beta(\lambda)$  is dependent on it. The optical-path length  $L'$  of the substance under the temperature shift  $\Delta T$  is

$$\begin{aligned} L' &= n(\lambda)(1 + \beta(\lambda)\Delta T) \cdot d(1 + \alpha\Delta T) \\ &= n(\lambda) \cdot d \{1 + (\alpha + \beta(\lambda))\Delta T\} \end{aligned} \quad (2.22)$$

The shift of optical-path length is given by

$$\begin{aligned} L' - L &= n(\lambda)\{1 + (\alpha + \beta(\lambda))\Delta T\}d - n(\lambda) \cdot d \\ &\cong n(\lambda) \cdot d(\alpha + \beta(\lambda))\Delta T \end{aligned} \quad (2.23)$$

If  $\alpha$ ,  $\beta$  and the initial optical-path length (that is,  $n \cdot d$ ) are known, we can obtain the temperature shift ( $\Delta T$ ) of the substance from eq. (2.23). The  $\alpha$  and  $\beta$  of silicon are well investigated experimentally. The  $\alpha$  and  $\beta$  of silicon, denoted by  $\alpha_{\text{Si}}$  and  $\beta_{\text{Si}}$ , are approximately expressed as

$$\alpha_{\text{Si}}(T) \cong -7.06 \times 10^{-11} T^2 + 6.83 \times 10^{-8} T + 2.38 \times 10^{-6} \quad (2.24)$$

$$\beta_{\text{Si}}(T) \cong -3.33 \times 10^{-11} T^2 + 6.76 \times 10^{-8} T + 5.01 \times 10^{-5} \quad (2.25)$$

The  $\alpha$  and  $\beta(\lambda)$  of the quartz ( $\alpha_{\text{SiO}_2}$ ,  $\beta_{\text{SiO}_2}$ ) are not known experimentally; therefore, the

$\alpha_{\text{SiO}_2}$  and  $\beta_{\text{SiO}_2}$  were assumed to be constant.

$$\alpha_{\text{SiO}_2} = 5.0 \times 10^{-7} \quad (2.26)$$

$$\beta_{\text{SiO}_2} = 7.0 \times 10^{-6} \quad (2.27)$$

Using these values or the values derived from the optical path lengths measured at different known temperatures in advance, we can find the temperature shift of layers from eq. (2.23).

## 2.3 Cavity Ring-Down Spectroscopy

Direct absorption spectroscopy is a simple, noninvasive, *in-situ* observation technique for obtaining information on the species in the gas, liquid or solid phase. From an absorption spectrum, quantitative or absolute concentrations, or absolute frequency-dependent cross-sections can be extracted. In a direct absorption experiment, the attenuation of light traveling through a sample is measured. The transmitted intensity follows the Beer–Lambert law.

$$I(t) = I_0 \exp(-\alpha d) \quad (2.28)$$

where  $I_0$  is the intensity of the incident light,  $d$  the length of the sample, and  $\alpha$  the absorption coefficient of the sample.<sup>[9]</sup> In case of the absorption being caused by a single species,  $\alpha(\nu) = N\sigma(\nu)$  with  $N$  being the number density (molecules per unit volume) of the absorber,  $\sigma(\nu)$  the absorption cross-section, and  $\nu$  the frequency of the light. More generally, one must sum over all the absorption and scattering losses that contribute to  $\sigma(\nu)$ .

In a simple model, where the duration of the laser pulse width is shorter than the round-trip time of the pulse in the cavity, the detector will see a train of pulses, each only slightly less intense than the previous one. The separation between adjacent pulses is equal to the round trip time  $t_r = 2L/c$ , where the length of the cavity is  $L$  and  $c$  is velocity of light. The intensity of the pulses will decrease due to absorption by the species in the cavity and the losses at the mirrors. Let us calculate the intensity at the detector. A laser pulse with an intensity  $I_{\text{laser}}$  is injected into a cavity. The two mirrors of

the cavity are identical and have a reflectivity  $R$  and a transmission  $T$ . For ideal mirrors, without absorption or scattering losses,  $T = 1 - R$ . However,  $T$  equals to 0.1 – 0.5 times of  $(1 - R)$ , which is typical for mirrors used in CRDS. After one pass through the cavity, the intensity of the first optical pulse at the detector is obtained from Beer–Lambert’s law in eq. (2.28):

$$I_0 = I_{laser} T^2 \exp(-\alpha(\nu)d) \quad (2.29)$$

where  $\alpha$  is the frequency-dependent absorption coefficient of the medium in the cavity. Here it is assumed that the sample is only present over a length  $d$  of the cavity. The intensity of the second pulse is then given by:

$$I_1 = I_0 R^2 \exp(-2\alpha(\nu)d), \quad (2.30)$$

where  $R^2 \exp(-2\alpha d)$  accounts for the loss due to the additional complete round trip through the cavity. Therefore, after  $n$  complete round trips, the pulse intensity behind the cavity will be

$$I_n = I_0 R^{2n} \exp(-2n\alpha(\nu)d). \quad (2.31)$$

Because the loss per pass is small, it is easy to pick a bandwidth of the electronics such that the individual pulses circulating in the cavity are not seen, but do not significantly distort the cavity decay. In the previous formula this means that the discrete number of

round trips  $n$  is replaced by the continuous parameter of time,  $t = n \times \frac{2L}{c}$ . Furthermore,

$R^{2n}$  can be written as  $\exp(2n \ln R)$ , which leads to

$$I(t) = I_0 \exp\left(\frac{tc}{L} (\ln R - \alpha(\nu)d)\right). \quad (2.32)$$

Since the mirrors used in cavity ring-down spectroscopy have a reflectivity  $R$  close to 1,

$\ln R \approx -(1 - R)$ , this can be rewritten as

$$I(t) = I_0 \exp\left(-\frac{tc}{L} (1 - R + \alpha(\nu)d)\right). \quad (2.33)$$

The  $1/e$  decay time of this exponentially decaying light intensity is called the ring-down time  $\tau$  and is defined as

$$\tau = \frac{L}{c(1 - R + \alpha(\nu)d)} \quad (2.34)$$

In a CRDS experiment, the ring-down time,  $\tau$  is measured as a function of laser frequency  $\nu$ . There are various ways in which the cavity decay rate can be extracted from the observed signal (these will be discussed in more detail below), but very often  $\tau$  is obtained from a weighted least-squares fit to the light intensity decay transient. An absorption spectrum is obtained by plotting the cavity decay rate  $k = \frac{1}{\tau}$  or the cavity losses  $\frac{1}{c\tau}$  as a function of frequency:

$$\frac{1}{c\tau(\nu)} = \frac{1-R}{L} + \alpha(\nu)\frac{d}{L} \quad (2.35)$$

This cavity loss is the sum of two terms, one is the mirror loss and determines the baseline of the CRD spectrum, i.e.  $\frac{1-R}{L}$ , and the other term includes the absorption, i.e.

$\alpha(\nu)\frac{d}{L}$ . Therefore, the absorption due to the sample in the cavity is obtained by subtracting the off-resonance loss  $k_0 = \frac{1}{\tau_0} = c\frac{1-R}{L}$  from the on-resonance loss:

$$\alpha(\nu)\frac{d}{L} = \frac{k-k_0}{c} = \frac{1}{c\tau} - \frac{1}{c\tau_0} \quad (2.36)$$

Thus, the concentration of sample in eq. (1.4) can be obtained.

## 2.4 Summary

In this chapter, the theory of the low-coherent interferometry, which is based on the Michelson interferometer, and cavity ring-down spectroscopy used in this study were presented. At first, the principle of the interferometry with high and low temporal coherence light was described. Next, the theory of substrate temperature measurement was presented. Finally, the principle of CRDS and introduce the earlier study of fiber-type CRDS were presented.

## References for Chapter 2

- [1] J. A. Izatt, M. D. Kulkarni, H.-W. Wang, K. Kobayashi, and M. V. Sivak, Jr., *IEEE J. Sel. Top. Quant. Electron.*, **2**, 1017 (1996).
- [2] V. M. Donnelly and J. A. McCaulley, *J. Vac. Sci. Technol. A*, **8**, 84 (1990).
- [3] J. A. McCaulley, V. M. Donnelly, M. Vernon, and I. Taha, *Phys. Rev. B*, **49**, 7408 (1994).
- [4] H.-S. Choi, H. F. Taylor, and C. E. Lee, *Opt. Lett.*, **22**, 1814 (1997).
- [5] S. Adachi, *Phys. Rev. B*, **38**, 12966 (1988).
- [6] I. H. Malitson, *J. Opt. Soc. Am.*, **55**, 1205 (1965).
- [7] K. Takeda, Y. Tomekawa, T. Shina, M. Ito, Y. Okamura, and N. Ishii, *J. Appl. Phys.* **43**, 7737 (2004).
- [8] C. Koshimizu, T. Ohta, T. Matsudo, S. Tuchitani, and M. Ito, *Appl. Phys. Expr.*, **3**, 056201 (2010).
- [9] A. M. Shaw, T. E. Hannon, F. P. Li, R. N. Zare, *J. Phys. Chem. B*, **107**, 7070 (2003).
- [10] A. O'Keefe, D. A. G. Deacon, *Rev. Sci. Instrum.*, **59**, 2544 (1988).

## Chapter 3

# Temperature Measurement of Si Substrate Using Optical-Fiber-Type Low-Coherence Interferometry Employing Supercontinuum Light

### 3.1 Introduction

As described in Section 1.3, temperature management technology in semiconductor fabrication processes, including the monitoring or controlling of the temperatures of the Si substrate and chamber, is important to achieve processes with high precision and reproducibility. According to ITRS, the manufacturing variations of gate must be controlled from 3 to 2 nm ( $3\sigma$ ) in the 45 nm generation and will be less than 1 nm in 20 nm generation which is scheduled in 2015. In near future, temperature fluctuation control or substrate with precise temperature measurement less than 1 °C will be necessary.

There are various methods for measuring temperature during plasma processing.<sup>[1-4]</sup> Typical methods in commercial chambers employ thermocouples, pyrometers, and optical-fiber type fluorescence temperature sensors.<sup>[2, 5]</sup> However, these techniques have

some problems, such as poor reliability, repeatability, measurement range and so on as described in Section 1.3.1.

A non-contact measurement of the temperature of a silicon (Si) substrate by using low-coherence interferometry (LCI) was demonstrated during silicon dioxide (SiO<sub>2</sub>) plasma etching in a dual-frequency capacitively coupled Ar/C<sub>4</sub>F<sub>8</sub>/O<sub>2</sub> plasma.<sup>[6]</sup>

As described in Section 1.3.2 and 2.2, in low-coherence interferometry, a broadband light source is the key component. The maximum resolving power of the optical path length of the media on the low-coherence interferometry depends on the coherent length, which defined by the wavelength bandwidth of its spectrum profile ( $\Delta\lambda$ ) and wavelength of the light source ( $\lambda_0$ ). The coherent length of light source is given by

$$l_c = \frac{2 \ln 2 \lambda_0^2}{\pi \Delta \lambda} . \quad (3.1)$$

The interferences at the front and back interfaces of the media are combined into an overlapping interference when the optical path length of the media is shorter than the coherence length of the light source. Then, the position of the overlapping interference is shifted from the actual position of the interface, resulting in an error in the measured temperature.

As described in Section 1.2, supercontinuum (SC) light has a broader spectrum than superluminescent diodes (SLDs), resulting in having the coherent length of typically several  $\mu\text{m}$ , which is shorter than that of SLD (typically 20  $\mu\text{m}$ ). Thus, using SC, the improvement of accuracy on temperature measurement is expected.

In this chapter, a high-resolution temperature measurement of Si wafer using optical low-coherence interferometer employing SC is presented. To employ SC for in the interferometer, the wavelength-dispersion of SC on Si wafer using a Si mirror as a reference mirror was compensated. Moreover, the simultaneous measurement of SiO<sub>2</sub> and Si temperatures on SiO<sub>2</sub>/Si substrate using the SC interferometer is demonstrated at the first time.

### 3.2 Experimental

The experimental system for measuring the Si temperature is shown in Fig. 3.1. The SLD and SC were used as low-coherence light sources. The spectra of SLD and SC are shown in Fig. 3.2(a) and 3.2(b), respectively. The coherent lengths of SLD or SC, assuming that the power spectrum is Gaussian profile, were estimated to be about 21.2 or 4.0  $\mu\text{m}$  from eq. (3.1), respectively. The collimated SLD light was irradiated to Si substrate in the black body furnace. Si substrate temperature was measured using thermocouples placed on the Si surface. A laser-type linear encoder was used for measuring the position of the reference mirror in order to compensate for the fluctuation of its scanning speed. The resolution of the pulse signal of the encoder was 40 nm, and this signal was used as a sampling clock for an analog/digital converter. The reference mirror was scanned at a speed of 60 mm/s. Al or Si mirror was used as a scanning reference mirror. Si is transparent for near infrared light, so the light is reflected by top and bottom surfaces while the light is reflected by the only top surface for Al mirror. The procedures for digitizing electric signal and for detecting the peak positions of the interference fringes were reported in the previous paper.<sup>[7]</sup> The interference fringes were

fitted by a least-squares approximation method and then the fringe peaks were obtained. The obtained fringe peaks were fitted by the least-squares approximation method again to detect the peak positions of the envelopes of the interference fringes.

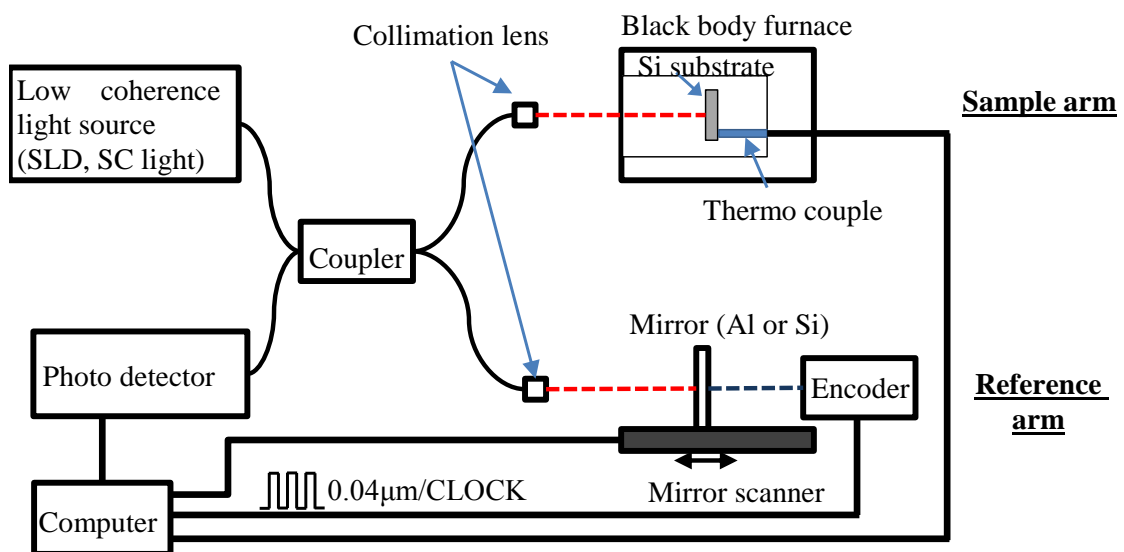
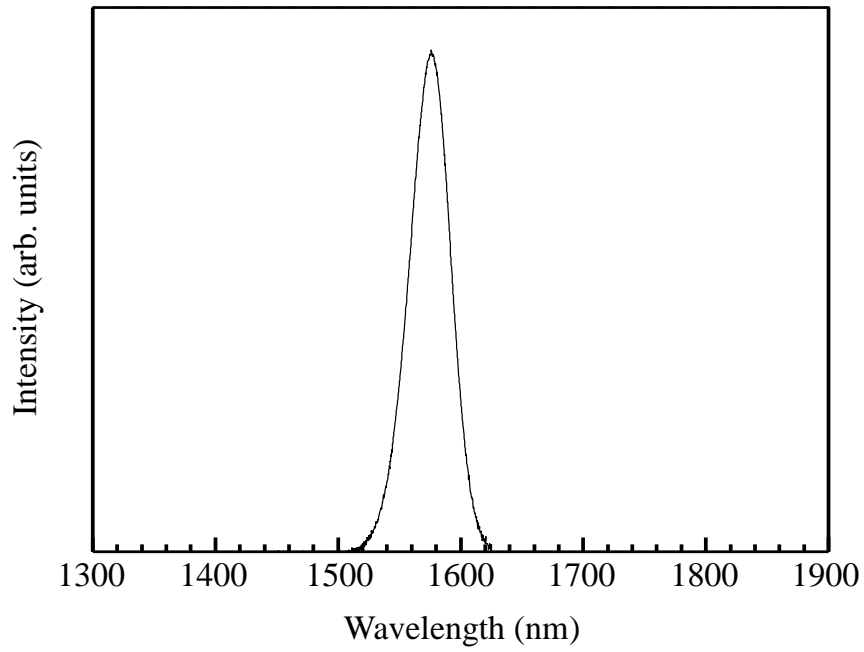
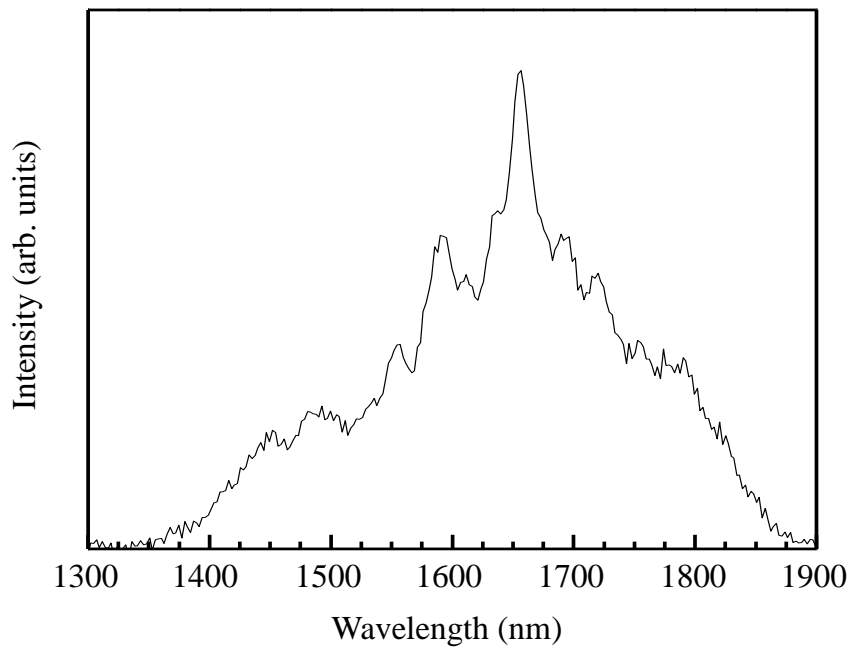


Fig. 3.1 Experimental system for measuring the temperature of Si substrate.



(a)



(b)

Fig. 3.2 Optical spectra of (a) SLD (b) SC.

## 3.3 Results and Discussion

### 3.3.1 Interference waveform

Figure 3.3 shows interference waveforms on the Si substrate measured by low-coherence interferometry employing SC. The thickness of the Si substrate was 800  $\mu\text{m}$ . The interference waveforms A (IW-A) and B (IW-B) correspond to the front and back surfaces of Si substrate, respectively. The temperature of Si is determined from the change in optical path length between IW-A and IW-B since the optical path length changes by the variation in refractive index depending on the Si wafer temperature and by the thermal expansion of Si wafer.

The interference waveforms of IW-A and IW-B using SC were shown in Figs. 3.4(a) and (b), and the interference waveforms of SLD (1.55  $\mu\text{m}$ ) were shown in Figs 3.4(c) and (d). The full width at half maximum (FWHM) at front surface for SC or SLD was 4.1  $\mu\text{m}$  or 28.8  $\mu\text{m}$ , respectively, as shown in Table 3.1.

In this paper, the FWHMs are used for the discussion of the envelope-widths of interference waveforms, which are referred to as coherence lengths. These values correspond with theoretical values assuming that the power spectrum of light source is Gaussian.

The FWHM of interference waveform at Si back surface for SC was expanded to be 37.9  $\mu\text{m}$  while that for SLD was not changed. This is caused by the wavelength dispersion in Si substrate, because the bandwidth of SC is approximately 500 nm while that of SLD is 50 nm. The refractive index of Si (25°C) is 3.542 to 3.500 in the range from 1300 to 1800 nm.<sup>[8]</sup>

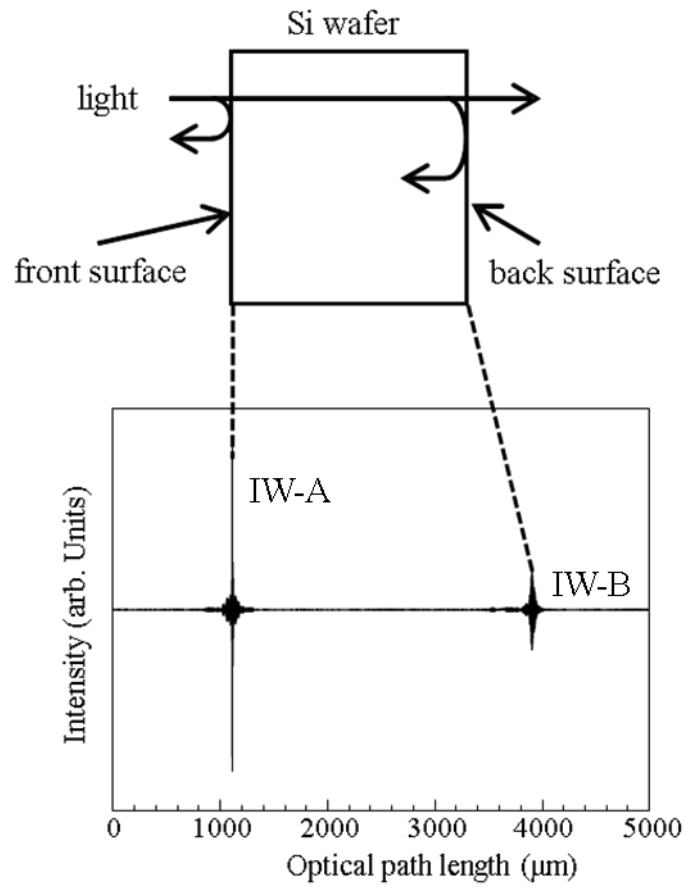


Fig. 3.3 Interference waveforms on the Si substrate using SC.

Table 3.1 FWHM of interference waveform.

	SLD 1576 nm	SC light
Theory	29.1 μm	-
Experimental	IW-A	4.1 μm
	IW-B	37.9 μm

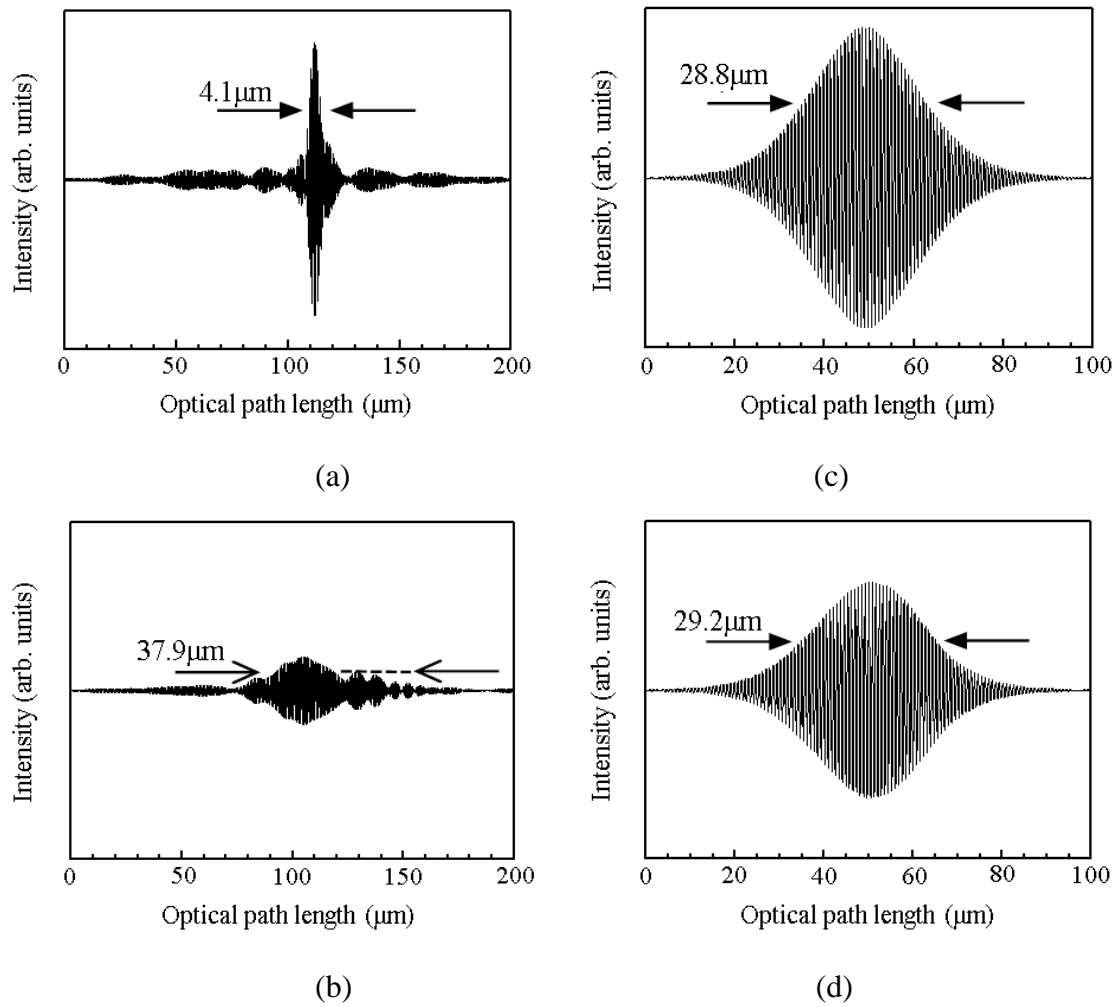


Fig. 3.4 Interference waveforms on the Si substrate (a) IW-A(SC) (b) IW-B (SC) (c) IW-A (SLD) (d) IW-B(SLD).

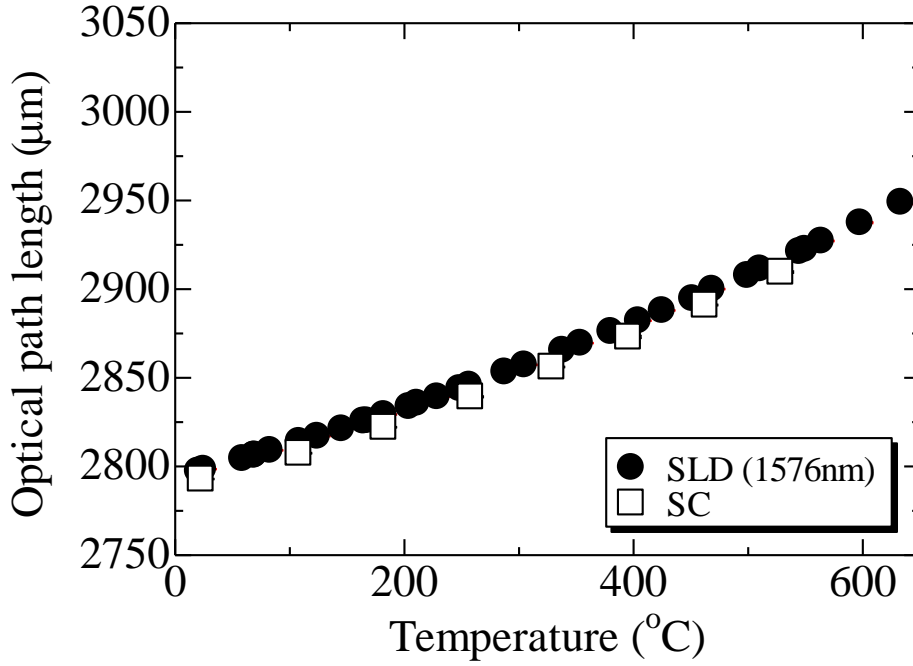


Fig. 3.5 Optical path length changes as a function of temperature.

Figure 3.5 shows optical path length of Si using SLD or SC as a function of the temperature. The temperature was controlled by a black body furnace and the temperature was measured by the thermocouples. The optical path lengths of Si monotonically increased with the temperature. The temperature parameter  $n(\lambda)(\alpha + \beta(\lambda))$  on SLD and SC calculate calculated from Fig. 3.4, which are given by

$$n(\lambda)(\alpha + \beta(\lambda))_{SLD} = 2.243 \times 10^{-4} + 1.335 \times 10^{-7} T + 4.725 \times 10^{-11} T^2 \text{ [}^\circ\text{C}^{-1}] \quad (3.2)$$

$$n(\lambda)(\alpha + \beta(\lambda))_{SC} = 1.921 \times 10^{-4} + 2.597 \times 10^{-7} T - 1.428 \times 10^{-11} T^2 \text{ [}^\circ\text{C}^{-1}] \quad (3.3)$$

The standard deviation of temperature calculated to substitute eq. (3.2) and (3.3) into the

eq. (2.23). The standard deviation of the optical path length and temperature were  $0.13 \mu\text{m}$  and  $\pm 1.0^\circ\text{C}$  for SLD. On the other hands, the optical path length and the temperature for SC were  $0.35 \mu\text{m}$  and  $\pm 1.7^\circ\text{C}$ . Thus, the multiple peaks of interferences were observed and interference waveform became round-shape as shown in Fig. 3.4(b), and resulting in the failure of temperature measurement.

### 3.3.2 Numerical simulation of interference waveforms

The interference waveform of SC shown in Fig. 3.4(b) is not Gaussian profile due to wavelength dispersion. Si mirror was used as a reference mirror to compensate the wavelength dispersion. In order to select the thickness of the Si mirror to obtain appropriate dispersion, interference waveforms as a function of the thickness of Si substrate were numerically simulated.

As shown in Fig. 3.6(a), the incident lights are reflected many times in Si substrate and Si mirror, because Si is transparent for the near infrared light. The electric fields of the reflected lights from the sample and reference arms interfere and are observed at a detector. Taking the multiple reflections in Si and the broadband spectrum of light source into account, the interference waveform is given by<sup>[9]</sup>

$$\tilde{I} \approx \int [E_1 E_2 \sqrt{R_1(\lambda, r) R_2(\lambda, d)} \times \cos\{2k\Delta l + \Phi_1(\lambda, r) - \Phi_2(\lambda, d)\} \cdot S(\lambda)] d\lambda, \quad (3.4)$$

where  $E_1$  and  $E_2$  are the electric fields of the sample and reference arms, respectively.  $\Delta l$  is the optical path difference,  $k$  is the wave number of the light source, and  $S(\lambda)$  is the power spectral density of the light source. The reflectance ( $R_1$ ) and the phase difference

$(\Phi_1)$  of Si substrate having the thickness  $r$  are given by

$$R_1(\lambda, r) = \frac{\rho_0^2 + \rho_1^2 + 2\rho_0\rho_1 \cos 2\delta}{1 + (\rho_0\rho_1)^2 + 2\rho_0\rho_1 \cos 2\delta} \quad (3.5)$$

$$\Phi_1(\lambda, r) = \tan^{-1} \frac{\rho_0(\rho_1^2 - 1) \sin 2\delta}{\rho_1(1 + \rho_0^2) + \rho_0(1 + \rho_1^2) \cos 2\delta} \quad (3.6)$$

$$\delta = \frac{2\pi}{\lambda} n_1(\lambda)r \quad (3.7)$$

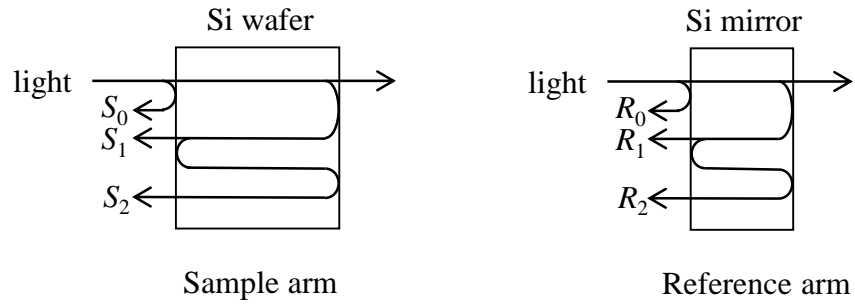
where  $\delta$  is the phase difference between the reflections at the Air/Si and Si/Air interfaces,  $n_1$  is refractive index of Si,  $\rho_0$  and  $\rho_1$  are the Fresnel reflection coefficients at the Air/Si and Si/Air interfaces, respectively.

In the same way, the reflectance ( $R_2$ ) and the phase difference ( $\Phi_2$ ) of Si mirror having the thickness  $d$  are given by

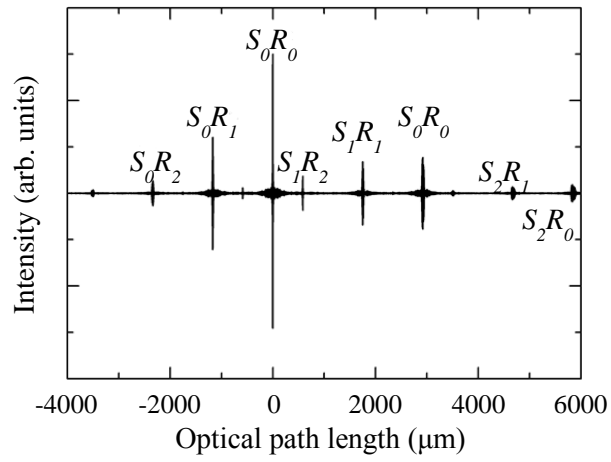
$$R_2(\lambda, d) = \frac{\rho_0^2 + \rho_1^2 + 2\rho_0\rho_1 \cos 2\varphi}{1 + (\rho_0\rho_1)^2 + 2\rho_0\rho_1 \cos 2\varphi} \quad (3.8)$$

$$\Phi_2(\lambda, d) = \tan^{-1} \frac{\rho_0(\rho_1^2 - 1) \sin 2\varphi}{\rho_1(1 + \rho_0^2) + \rho_0(1 + \rho_1^2) \cos 2\varphi} \quad (3.9)$$

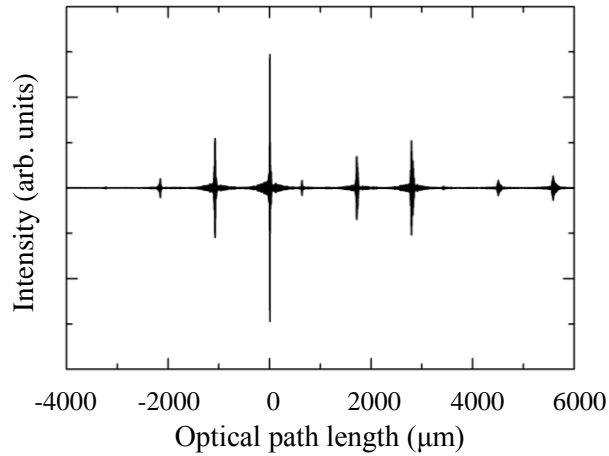
$$\varphi = \frac{2\pi}{\lambda} n_1(\lambda)d \quad (3.10)$$



(a)



(b)



(c)

Fig. 3.6 Interference waveforms for 800- $\mu\text{m}$ -thickness Si wafer with 320- $\mu\text{m}$ -thickness Si mirror (a) schematic illustration of light reflected by Si wafer or Si mirror, (b) simulation (c) experimental result.

Figure 3.6(b) shows the interference waveform calculated by eq. (3.4). The power spectrum of SC is shown in Fig. 3.2(b) and the thicknesses of Si wafer and Si mirror are 800 and 320  $\mu\text{m}$ , respectively. Multi-interference waveforms are observed because the incident lights for sample and reference arms are reflected at front and back surfaces of Si substrate and Si mirror as shown in Fig. 3.5(b). The position of interference caused by reflected light at front surfaces of Si substrate and Si mirror ( $S_0R_0$ , which indicates the interference waveform generated by the reflected lights  $S_0$  and  $R_0$  shown in Fig. 3.6(a)) is defined to be optical path length of zero.

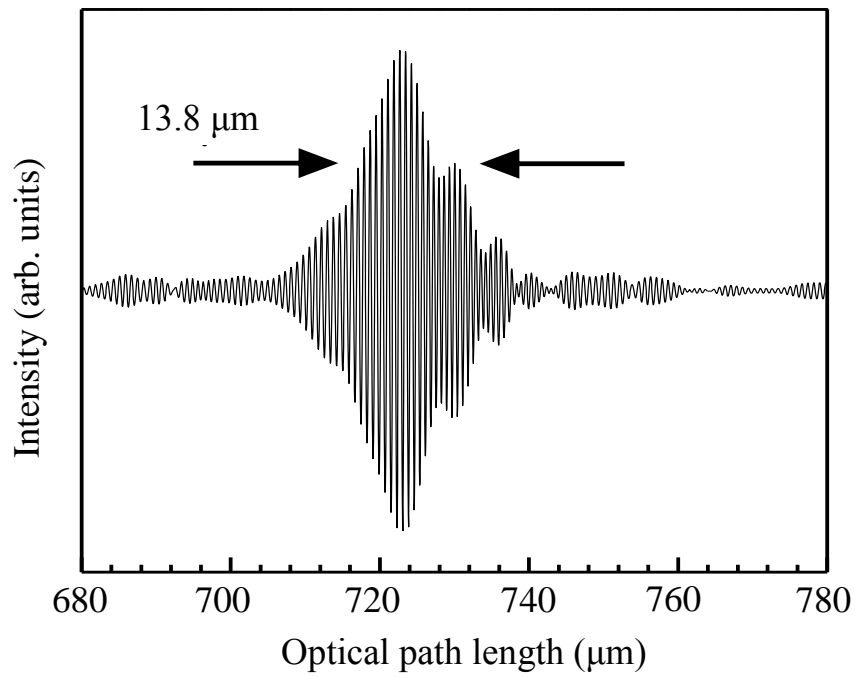
Figure 3.6(c) shows the interference waveform measured by low-coherence interferometry using SC for the thickness of Si substrate of 800  $\mu\text{m}$  with 320- $\mu\text{m}$ -thickness Si mirror. The simulated interference waveforms corresponded to the measured interference waveforms very well.

Figures 3.7 show simulated waveforms interfered by back surfaces of Si substrate and Si mirror ( $S_1R_1$ ) in the cases of thicknesses of Si mirror (a) 600  $\mu\text{m}$ , (b) 700  $\mu\text{m}$ , (c) 785  $\mu\text{m}$ , and (d) 795  $\mu\text{m}$ . The shape of interference waveform  $S_1R_1$  became Gaussian-like sharp waveform and the position of interference waveform approached to  $S_0R_0$  with increasing the thickness of Si mirror. The FWHMs of waveforms in Fig.3.7 were (a) 13.8  $\mu\text{m}$ , (b) 5.5  $\mu\text{m}$ , (c) 3.9  $\mu\text{m}$ , and (d) 4.0  $\mu\text{m}$ , respectively.

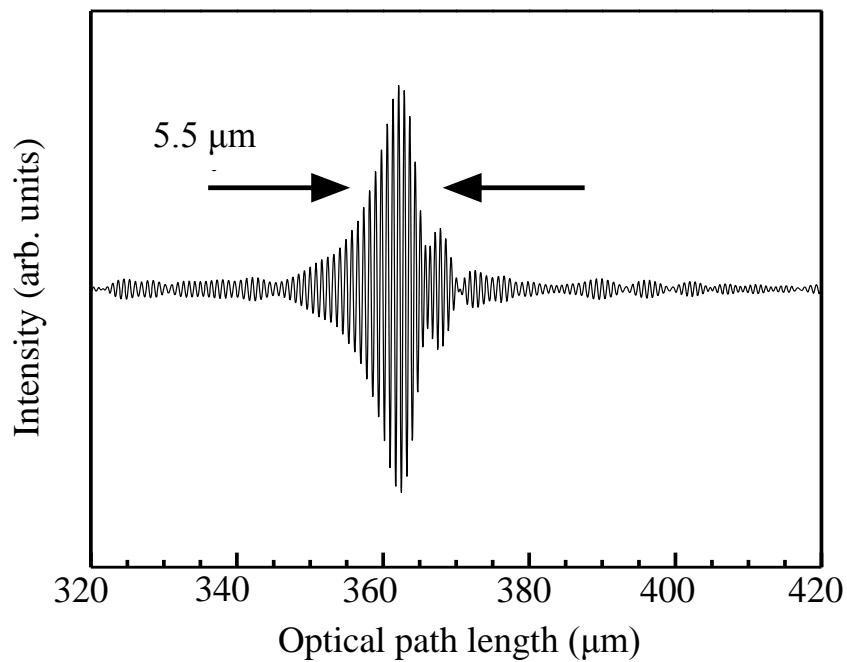
Figure 3.7 shows the FWHM of interference waveform  $S_1R_1$  as a function of thickness of Si mirror. The FWHM decreased with increasing the thickness of Si mirror. This is because the wavelength dispersion is compensated as the thickness of Si mirror close to that of Si wafer. However, in the case of 795  $\mu\text{m}$ , interference waveforms of  $S_0R_0$  and  $S_1R_1$  were overlapped, resulting in the lower signal to background ratio and the FWHM slightly become larger as shown in Fig. 3.7(d). From these results, we

concluded that the appropriate thickness of Si mirror was 785  $\mu\text{m}$  for 800  $\mu\text{m}$  Si wafer.

Figure 3.8 shows the experimental interference waveforms in the case of the Si mirror was 785  $\mu\text{m}$  for 800  $\mu\text{m}$  Si wafer. The FWHMs of  $S_0R_0$  and  $S_1R_1$  were 5.9  $\mu\text{m}$  and 4.1  $\mu\text{m}$ , respectively. The wavelength dispersion was compensated and the FWHMs of front and back surface are smaller than those by SLD.

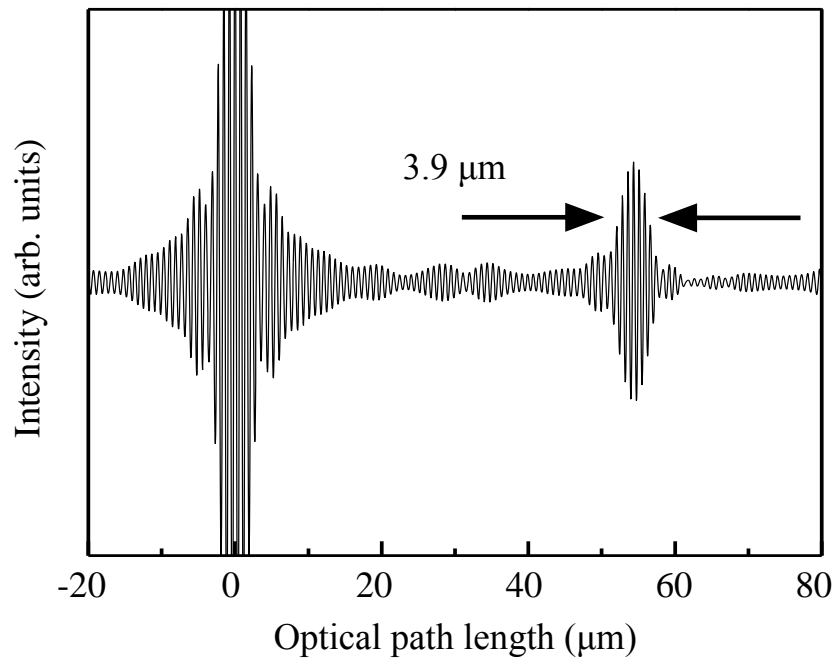


(a)

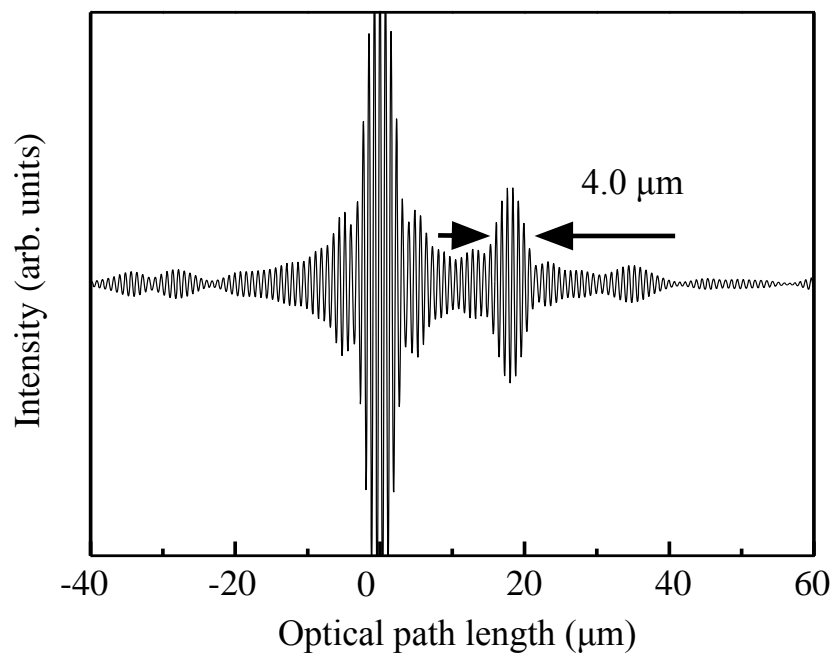


(b)

Fig. 3.7 Simulated waveforms interfered by back surfaces of Si substrate and Si mirror ( $S_1R_1$ ) in the case of thickness of Si mirror (a) 600  $\mu\text{m}$ , (b) 700  $\mu\text{m}$ .



(c)



(d)

Fig. 3.7 Simulated waveforms interfered by back surfaces of Si substrate and Si mirror ( $S_1R_1$ ) in the case of thickness of Si mirror (c) 785  $\mu\text{m}$  (d) 795  $\mu\text{m}$ .

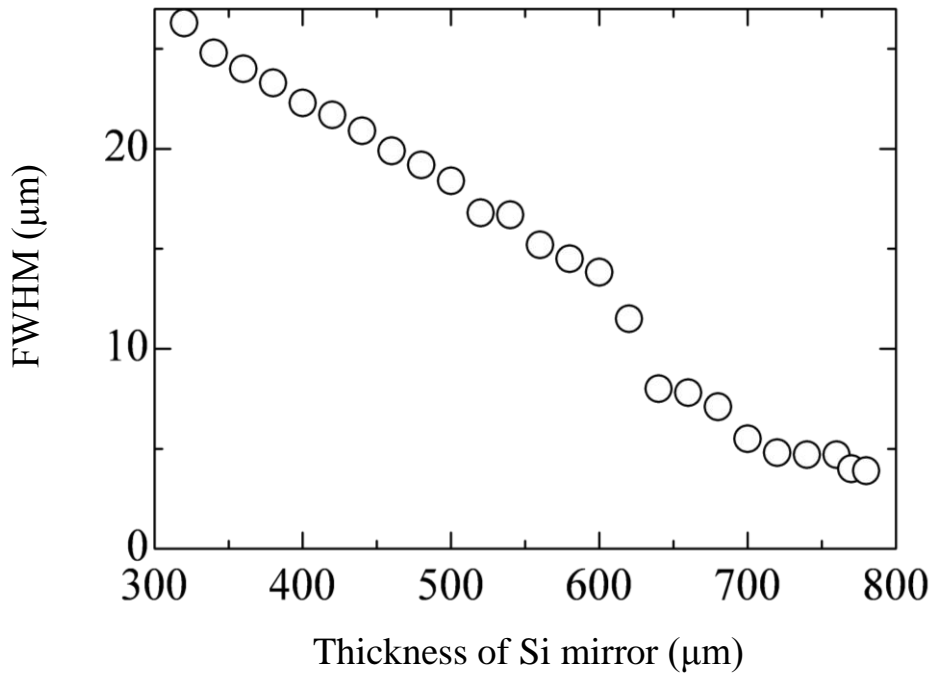


Fig. 3.8 FWHM of interference waveform ( $S_1R_1$ ) as a function of thickness of Si mirror.

The measurement accuracy using SC was compared with SLD for 800  $\mu\text{m}$ -thickness Si wafer. Table 3.2 is shown standard deviation of optical path length and temperature using SC and SLD. In the case of SC, the deviation on the optical path length was 0.08  $\mu\text{m}$  and this is equivalent to  $\pm 0.4$   $^\circ\text{C}$  on the temperature. On the other hand, the optical path length and the temperature for SLD were 0.13  $\mu\text{m}$  and  $\pm 1.0$   $^\circ\text{C}$ , respectively.

The optical path length is measured from the peak positions of interference waveforms. The accuracy of temperature measurement depends on the detection of the peak-position. The coherence lengths of SC lights (less than 6  $\mu\text{m}$ ) were shorter than those of SLD lights (around 29  $\mu\text{m}$ ) and then the interference waveforms of SC lights at front and back surfaces are sharper than the those of SLD lights as shown in Figs. 3.4(c),

3.4(d), and 3.9. Thus, the measurement accuracy was successfully improved by using SC.

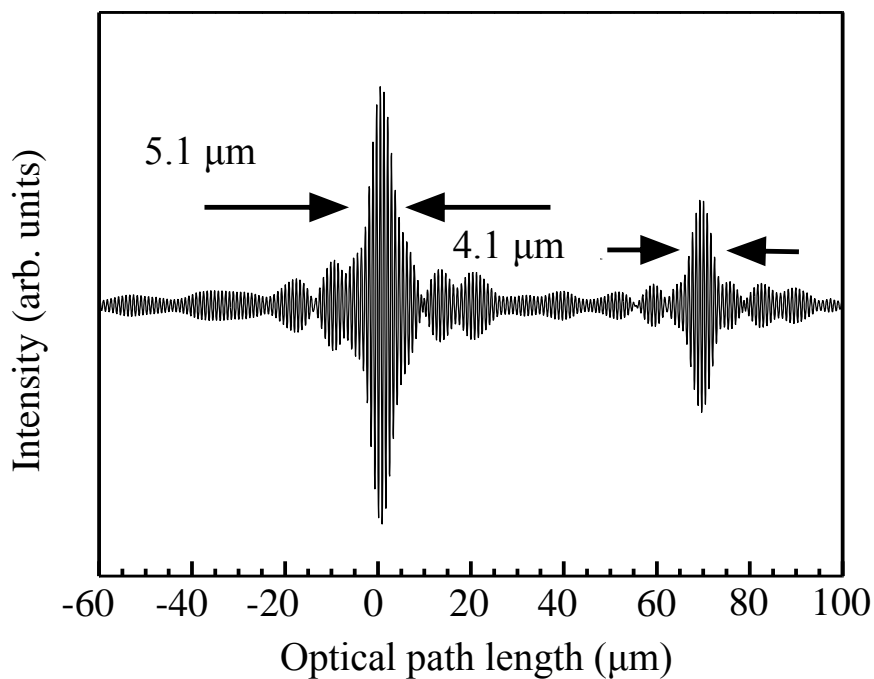


Fig. 3.9 Interference waveforms for 785- $\mu\text{m}$ -thickness-Si mirror and 800- $\mu\text{m}$ -thickness Si wafer.

Table 3.2 Standard deviation of optical path length and temperature.

	SLD1576 nm	SC light
Optical path length deviation ( $\mu\text{m}$ )	0.13	0.08
Temperature deviation ( $^{\circ}\text{C}$ )	$\pm 1.0$	$\pm 0.4$

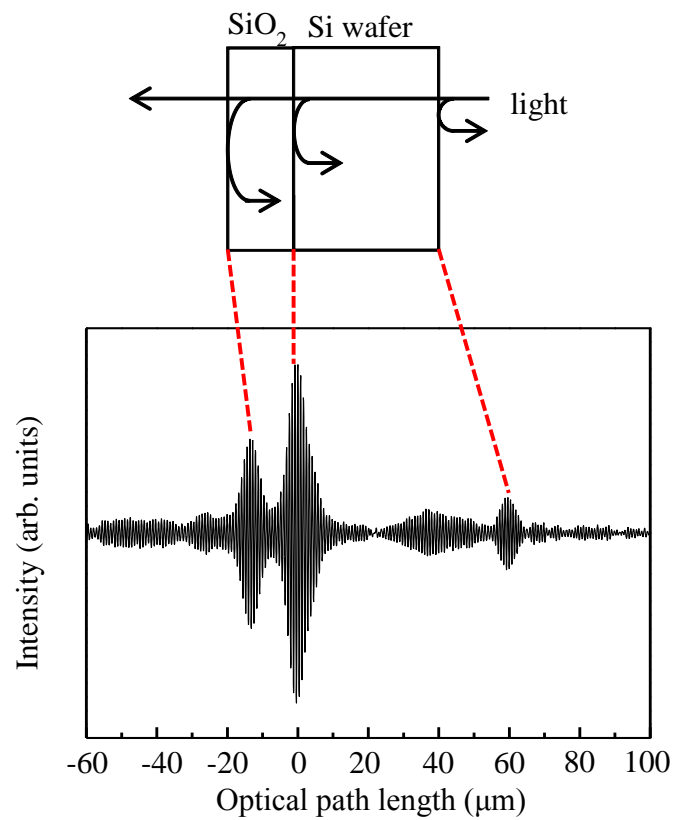
### 3.3.3 Temperature measurement of SiO<sub>2</sub>/Si substrate

The temperatures of SiO<sub>2</sub> and Si layers of SiO<sub>2</sub>/Si substrate were simultaneously measured. The SiO<sub>2</sub>/Si substrate has 8.55- $\mu\text{m}$ -thickness SiO<sub>2</sub> layer on Si substrate with thickness of 800  $\mu\text{m}$ . Figures 3.10 show the interference waveforms of SiO<sub>2</sub>/Si substrate using (a) SC with compensation and (b) SLD (center wavelength: 1325 nm). In the case of SC, the interference waveforms at SiO<sub>2</sub>/air and SiO<sub>2</sub>/Si were separated while those were overlapped in the case of SLD. These results show that the measurement of optical-path length of the film thinner than 20  $\mu\text{m}$  is difficult by using SLD while that is capable by using SC. Figure 3.11 shows optical path length of Si and SiO<sub>2</sub> using SC as a function of the temperature. The temperature was controlled by a black body furnace and the temperature was measured by the thermocouples. In this measurement, the temperature was well stabilized in the black body furnace for each measurement. The optical path lengths of Si and SiO<sub>2</sub> monotonically increased with the temperature. These results indicate that Si and SiO<sub>2</sub> temperatures can be simultaneously measured by using low-coherence interferometry with SC. In the case of Si layer, the deviation on the optical path length was 0.185  $\mu\text{m}$ , which is equivalent to  $\pm 0.9^\circ\text{C}$  on the temperature. On the other hand, the optical path length and the temperature for SiO<sub>2</sub> were 0.108  $\mu\text{m}$  and  $\pm 11.6^\circ\text{C}$ , respectively.

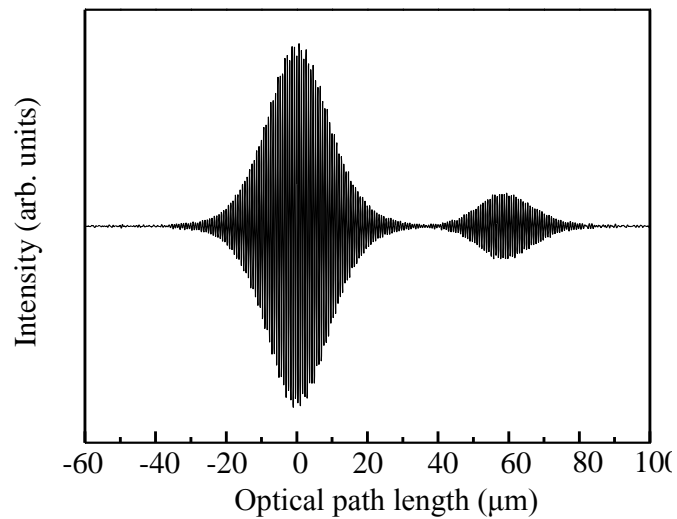
The deviation of Si was slightly larger than that of Si wafer without SiO<sub>2</sub> layer, which seems to be from the deterioration of interference waveform at SiO<sub>2</sub>/Si due to the slight overlapping of waveform at SiO<sub>2</sub>/air. The temperature deviation of SiO<sub>2</sub> was larger than that of Si because the thickness and refractive index of SiO<sub>2</sub> were smaller than those of Si, and then the change on the optical length of SiO<sub>2</sub> against temperature

## Chapter 3

variation is much smaller than that of Si. Further study is necessary for improving the accuracy for measuring the temperature of SiO<sub>2</sub> thin layer, however, a simultaneous measurement of SiO<sub>2</sub> film thickness and Si wafer temperature has been successfully carried out using SC interferometry, which will be a powerful tool for monitoring and controlling future semiconductor fabrication processes.



(a)



(b)

Fig. 3.10 Interference waveform of SiO<sub>2</sub>/Si substrate using (a) SC with compensation and (b) SLD.

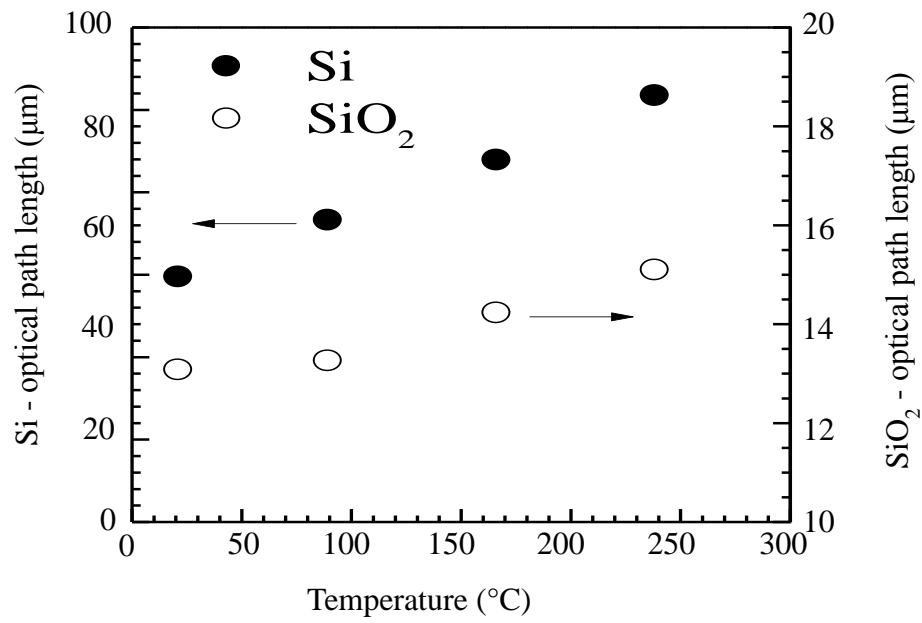


Fig. 3.11 Optical path lengths of Si and SiO<sub>2</sub> using SC as a function of the temperature.

### 3.4 Summary

In this study, the high-resolution temperature measurement of Si wafer was presented using optical low-coherence interferometer employing SC. The measurement accuracy on wafer temperature is improved by achieving higher resolution of optical path length of wafer. The maximum resolving power of the optical path length of the media on the low-coherence interferometry depends on the coherent length which determined by the spectrum profile and wavelength of the light source. The interferences at the front and back interfaces of the media are combined into an overlapping interference when the optical path length of the media is shorter than the coherence length of the light source. We focused on low-noise, ultra-flat, and highly coherent SC generated using ultra-short laser pulse and optical fibers as the light source. The SC has a broader spectrum than SLDs, which leads that the coherent length of SC is typically several  $\mu\text{m}$  while that of SLD is 20  $\mu\text{m}$ . To employ SC for in this system, we compensated the wavelength-dispersion of SC in Si wafer using a Si mirror as a reference mirror and the interference waveforms of SC lights at front and back surfaces of Si wafer are sharper than those of SLD lights. The measurement accuracy on the temperature using SC was improved to be  $\pm 0.4^\circ\text{C}$  from  $\pm 1.0^\circ\text{C}$  for SLD. The temperatures of Si wafer and  $\text{SiO}_2$  thin film wafer were simultaneously measured by using SC on 8.55- $\mu\text{m}$ -thickness  $\text{SiO}_2$  film/800- $\mu\text{m}$ -thickness Si substrate. Measurement deviations of temperature were  $\pm 0.9^\circ\text{C}$  for Si and  $\pm 11.6^\circ\text{C}$  for  $\text{SiO}_2$ . The change on the optical length of  $\text{SiO}_2$  against temperature variation is smaller than that of Si due to smaller refractive index and thinner thickness of  $\text{SiO}_2$  layer. These results show that a simultaneous measurement of  $\text{SiO}_2$  film thickness and Si wafer temperature has been

## Chapter 3

successfully carried out using a SC interferometry. A semiconductor manufacturing process could be controlled more accurately using this monitoring system.

## References for Chapter 3

- [1] J. L. Booth, B. T. Beard, J. E. Stevens, M. G. Blain, and T. L. Meisenheime, *J. Vac. Sci. Technol. A*, **14**, 2356 (1996).
- [2] A. Cardoso and A. K. Srivastava, *J. Vac. Sci. Technol. B*, **19**, 397 (2001).
- [3] J. L. Cui, K. Amtmann, J. Ristein, and L. Ley, *J. Appl. Phys.*, **83**, 7929 (1998).
- [4] U. J. Gibson and M. Chernuschenko, *Opt. Exp.*, **4**, 443 (1999).
- [5] T. Sato, *Jpn. J. Appl. Phys.*, **6**, 339 (1967).
- [6] C. Koshimizu, T. Ohta, T. Matsudo, and S. Tuchitani, M. Ito, *Appl. Phys. Expr.*, **3**, 056201 (2010).
- [7] T. Ohta, C. Koshimizu, K. Kawasaki, K. Takeda, and M. Ito, *J. Appl. Phys.*, **105**, 13110 (2009).
- [8] K. Takeda, Y. Tomekawa, T. Shiina, M. Ito, Y. Okamura, and N. Ishii, *Jpn. J. Appl. Phys.*, **43**, 7737 (2004).
- [9] J. A. Izatt, M. D. Kulkarni, H.-W. Wang, K. Kobayashi, and M. V. Sivak, Jr., *IEEE J. Sel. Top. Quantum Electron.*, **2**, 1017 (1996).

## Chapter 4

# Temperature Measurement of Silicon Substrate with Carbon Nanowalls Using Optical Low-Coherence Interferometry

### 4.1 Introduction

Carbon nanowalls (CNWs) are one of carbon nanostructures, which comprise stacks of graphene layers standing vertically on a substrate and successfully synthesized by plasma enhanced chemical vapor deposition (PECVD).<sup>[1-6]</sup> They have excellent electrical conductivity and chemical strength derived from the features of their graphene sheets. Therefore, electronic channels, interconnects, and electrodes in logical devices, electron field emitters, catalytic electrodes of fuel cells, electric double-layer capacitors, biosensing elements, and other devices are expected to be realized using CNWs. As described in Section 1.3 and Chapter 3, the substrate temperature during processing is one of important parameters to control CNWs structures and it is essential to measure the temperature in the high-temperature range for controlling the structures and characteristics of CNWs precisely.

The non-contact measurement of the temperature of a silicon (Si) substrate by using low-coherence interferometry (LCI) was reported by Takeda et al. [7] The LCI has many advantages such as temperature measurement of substrate itself, real-time response, wide measurement range, wide applicable plasma conditions, and high measurement accuracy. Many applications has been realized such as temperature measurements of Si substrate in silicon-dioxide (SiO<sub>2</sub>) plasma etching<sup>[8]</sup> and organic-film plasma etching<sup>[9]</sup>, demonstration of an autonomously controllable plasma etching system<sup>[10]</sup>, simultaneous measurement of Si substrate temperature and SiO<sub>2</sub> thickness on SiO<sub>2</sub>/Si substrate<sup>[11, 12]</sup>, and improvement of measurement accuracy using supercontinuum light (SC).<sup>[13]</sup>

The Si temperature is determined from the change in optical path length between interference waveform of the front and back surfaces since the optical path length is changed by thermal expansion and the variation in refractive index depending on the Si substrate temperature.

$$L'-L = n(\lambda)d(\alpha + \beta(\lambda))\Delta T, \quad (4.1)$$

where  $d$  and  $n(\lambda)$  are respectively the thickness and the refractive index of the Si substrate at the initial temperature.  $L$  is the optical path length at the initial temperature,  $L'$  is the optical path length after the temperature change.  $\Delta T$  is the temperature variation from the initial temperature.  $\alpha$  is the coefficient of linear thermal expansion and  $\beta(\lambda)$  is the coefficient of temperature dependence of the refractive index. Here, the  $n$  and the  $\beta(\lambda)$  are functions of wavelength of the light source.

From view points of the measurement accuracy, a broadband light source is a key factor. The maximum resolving power of the optical path length of the media on the

low-coherence interferometry depends on the coherent length, which defined by the spectrum profile and wavelength of the light source. We have reported the improvement of accuracy with SC, which is low-noise, ultraflat, and highly coherent laser pulse generated by using ultrashort laser pulse and optical fibers. <sup>[14-20]</sup> The change in the optical path length depends on the wavelength as described in eq. (4.1) while SC contains the broadband wavelength. It is essential to investigate the wavelength characteristics on temperature measurement using LCI in order to enhance the measurement accuracy.

In this study, we demonstrate temperature measurements of Si substrate with CNWs layer using optical low-coherence interferometer employing SC and superluminescent diodes (SLDs). The wavelength dependence on the optical path length, that is refractive index, was investigated by using SC and three SLDs having different wavelengths.

## 4.2 Experimental

The experimental system for measuring the temperature is shown in Fig. 4.1. SC was generated using ultrashort laser pulse and highly nonlinear fibers. <sup>[14-20]</sup> The output pulses from a passively mode-locked erbium-doped fiber laser were used as pump pulses. The laser generated 260-fs-sech<sup>2</sup>-shaped ultrashort pulses, which were introduced into a normal dispersive highly nonlinear fiber (ND-HNLF), resulting in the generation of SC pulses with a pulse width of 10 ps due to the monotonous positive chirp pulse along the group-delay curve of the ND-HNLF. <sup>[17, 18]</sup> The coherent length of SC, assuming that the power spectrum has Gaussian profile, was estimated to be about 4.0  $\mu\text{m}$ . Moreover, three SLDs with 1325 nm (a full width at half maximum (FWHM))

of 38.0 nm, coherent length of 20.4  $\mu\text{m}$ ), 1576 nm (FWHM of 37.6 nm, coherent length of 29.1  $\mu\text{m}$ ), and 1661 nm (FWHM of 42.4 nm, coherent length of 28.3  $\mu\text{m}$ ) were used.

The collimated SLD light was irradiated to a substrate in the black-body furnace. Temperature was measured using thermocouples placed on the substrate surface. A laser-type linear encoder was used for measuring the position of the reference mirror in order to compensate for the fluctuation of its scanning speed. Al mirror was used as a scanning reference mirror. The measurement on each temperature was performed after the temperature in black-body furnace become constant. Thus, in this study, the temperature measured by the thermocouple in the black-body furnace was defined as the true value of the substrate temperature because the probe of the thermocouple and the substrate were at thermal equilibrium in the black-body furnace.

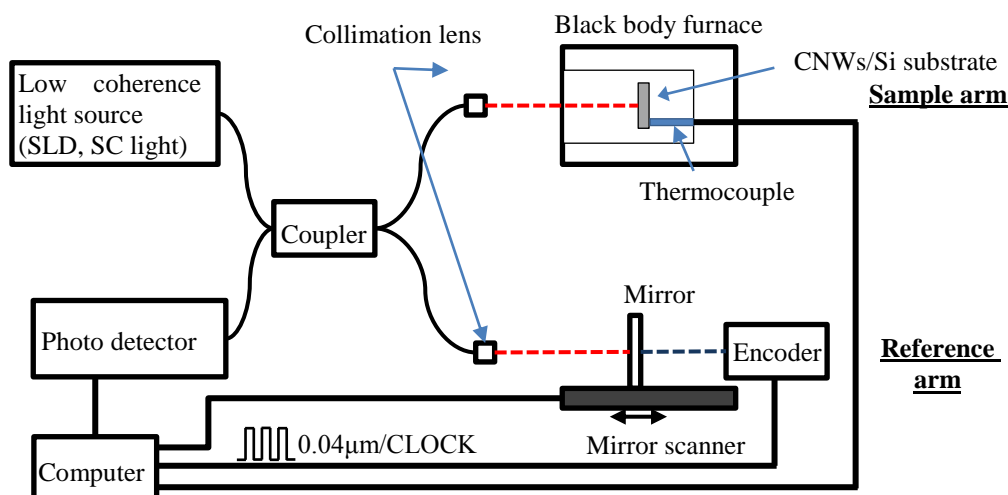


Fig. 4.1 Experimental system for measuring the CNWs/Si or Si temperature.

## 4.3 Results and Discussion

### 4.3.1 Fabrication of Carbon nanowalls

CNWs were synthesized by radical injection PECVD as shown in Fig. 4.2.<sup>[6]</sup> This system consists of a parallel-plate very high frequency (VHF) capacitively coupled plasma (CCP) region and a surface-wave microwave excited H<sub>2</sub> plasma (SWP) as a radical source installed in the CCP region. The powers of 400 W with VHF 100 MHz for VHF-CCP and of 500 W with 2.45 GHz for SWP were respectively applied. The flow rates of CH<sub>4</sub> and H<sub>2</sub> were maintained at 100 and 50 standard cubic centimeters per minute, respectively. The total pressure was 5 Pa and the substrate surface temperature was 580 °C using an optical pyrometer. Growth time was 15 min and resulting in CNWs with the height of ~ 500 nm on 450- $\mu$ m-thick Si substrates. The SEM images of CNWs are shown in Fig. 4.3.

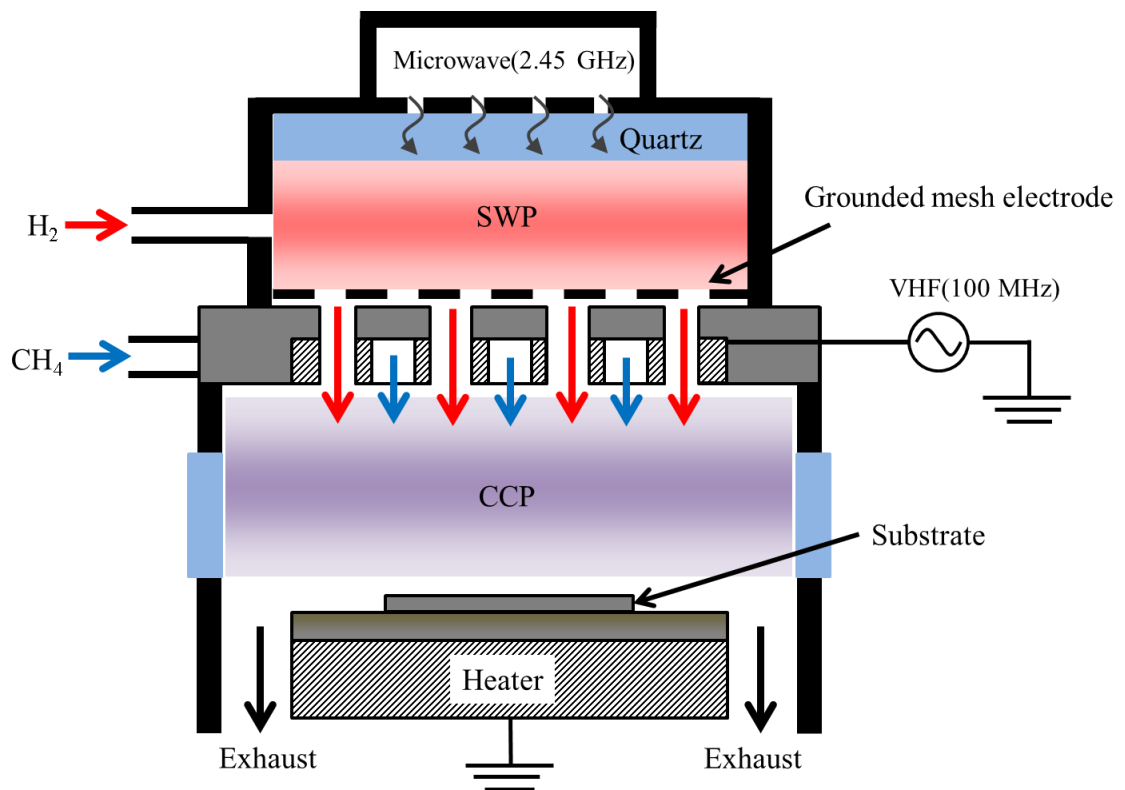
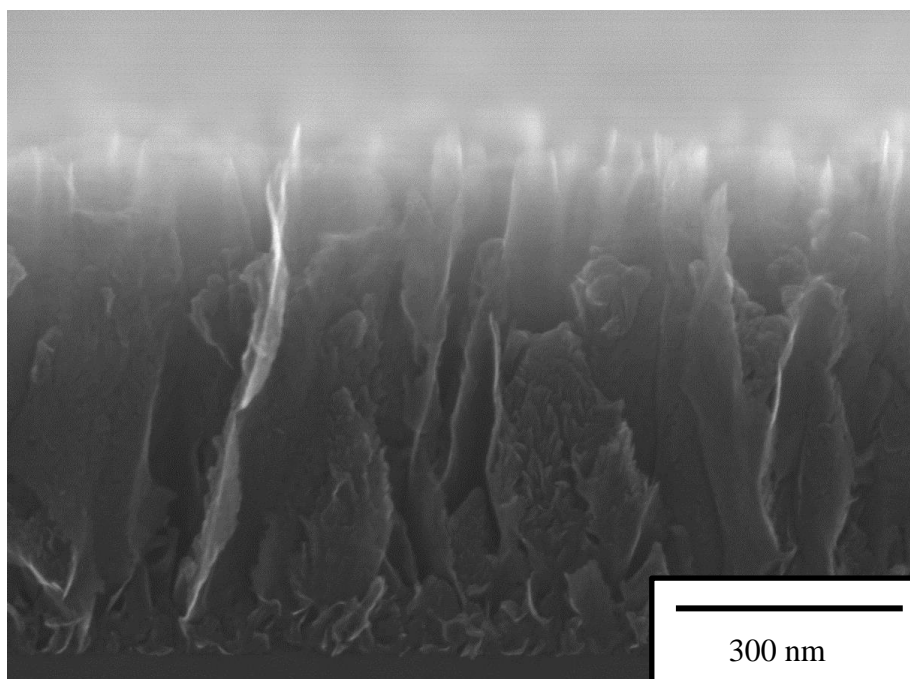
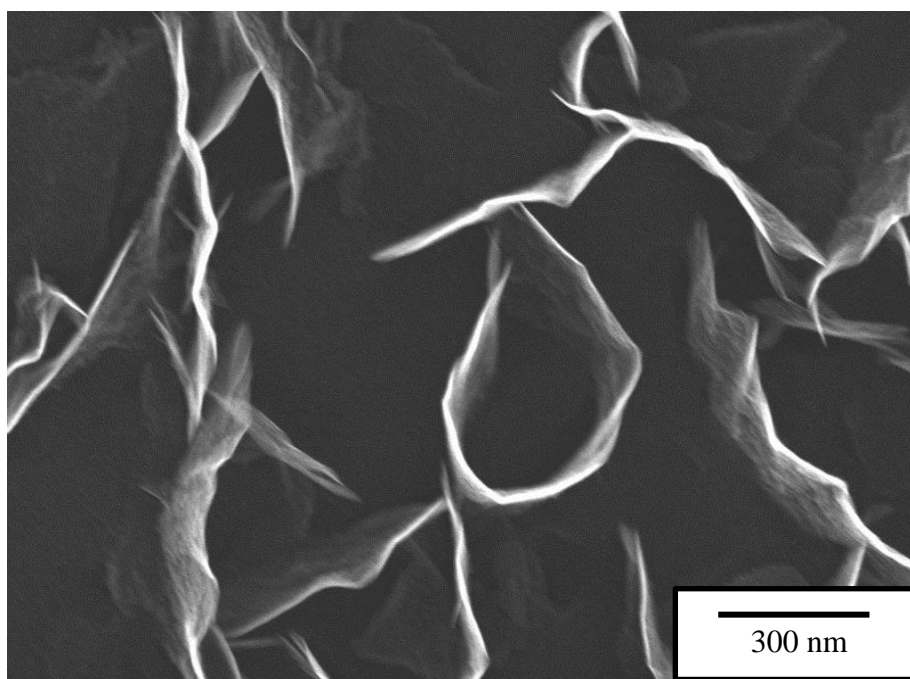


Fig. 4.2 Schematic diagram of radical injection plasma enhanced chemical vapor deposition (RI-PECVD) system.



(a)

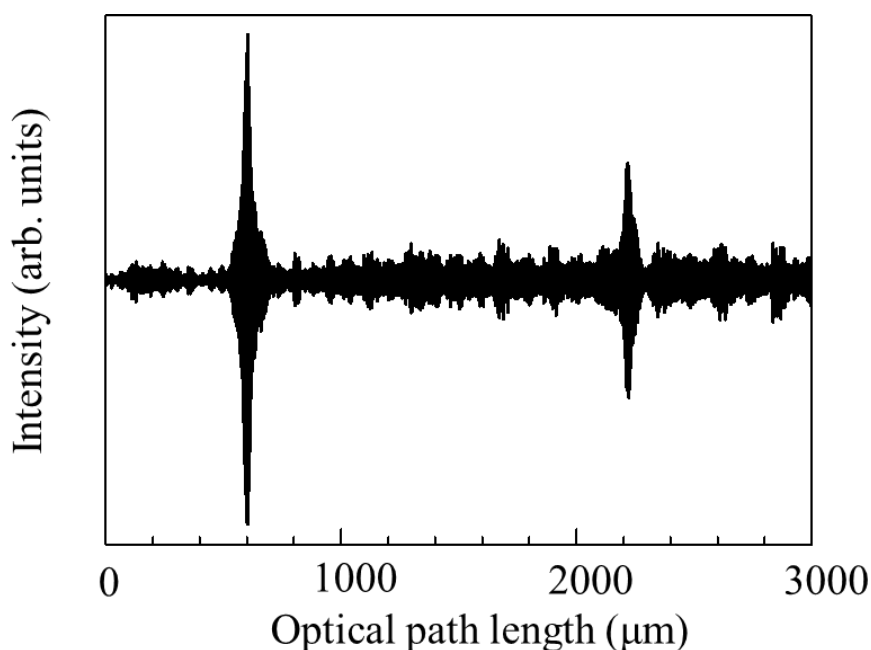


(b)

Fig. 4.3 SEM image of CNWs, (a) cross-sectional view, (b) top view.

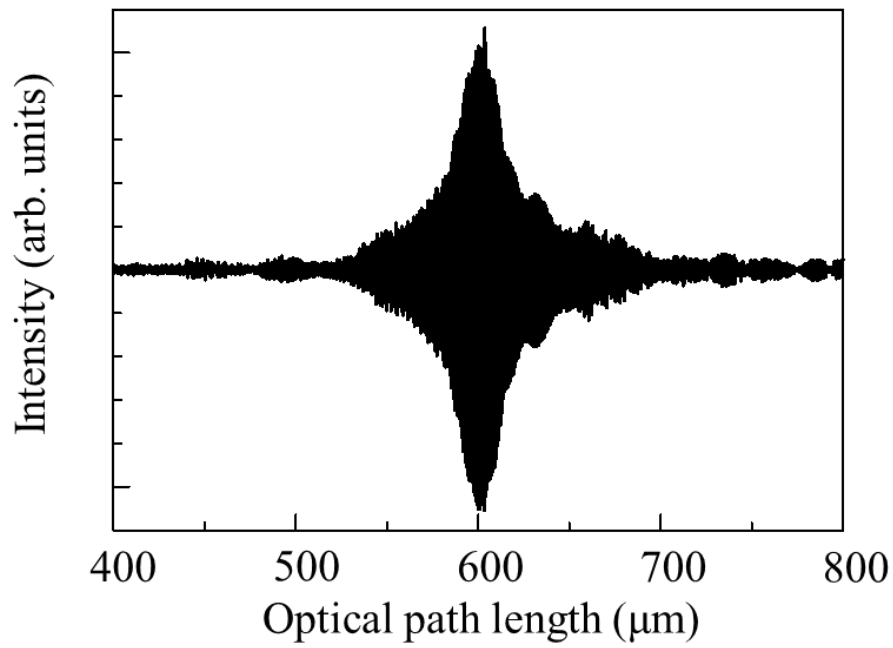
### 4.3.2 Interferogram of CNWs/Si substrate using SLDs and SC

Figure 4.4 show an interference waveform of the CNWs/Si substrate using SC as a light source, (a) whole waveform, (b) enlarged waveform of bottom surface, and (c) enlarged waveform of top surface. The light was introduced to the CNWs/Si substrate from the bottom surface. As shown in Fig. 4.4(c), one interference waveforms was observed for the bottom surface despite containing Si/CNWs and CNWs/air interfaces because the coherent lengths of the light sources was much larger than the thickness of CNWs resulting in the waveforms originated from the CNWs/Si and CNWs/air interfaces were superimposed.

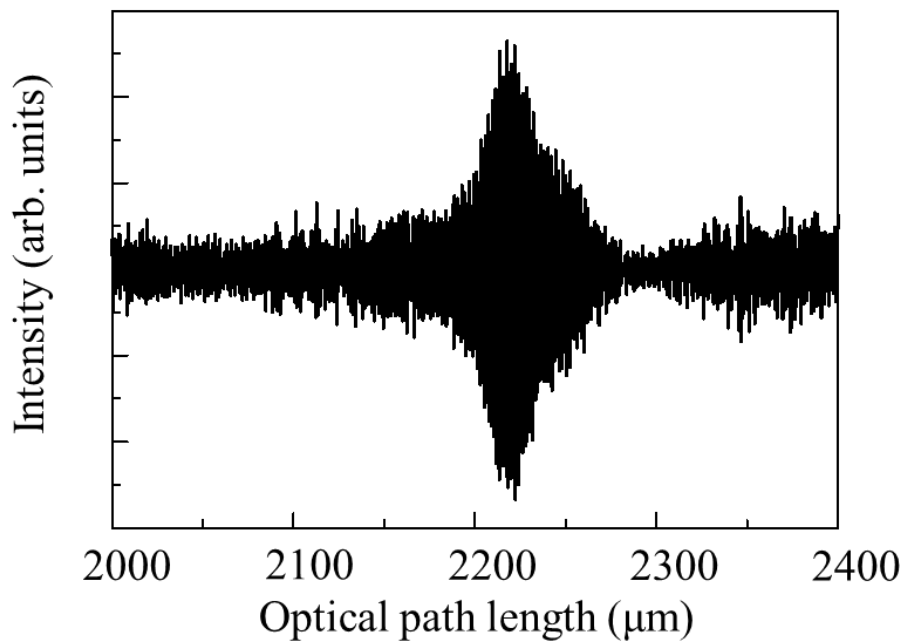


(a)

Fig. 4.4 Interference waveforms on the CNWs/Si substrate using SC (a) whole waveform.



(b)



(c)

Fig. 4.4 Interference waveforms on the CNWs/Si substrate using SC (b) enlarged waveform of bottom surface, and (c) enlarged waveform of top surface.

### 4.3.3 Measurement of temperature parameters of CNWs/Si substrate

Figure 4.5 shows the optical path length of CNWs/Si substrate as a function of temperature measured by thermocouples. Optical path length was deduced from the distance between the peaks of the interferences at the bottom and top surface as shown in Fig. 4.4. The optical path lengths monotonically increased with the temperature. These results indicate that the temperature of CNWs/Si substrate can be measured by using low-coherence interferometry.

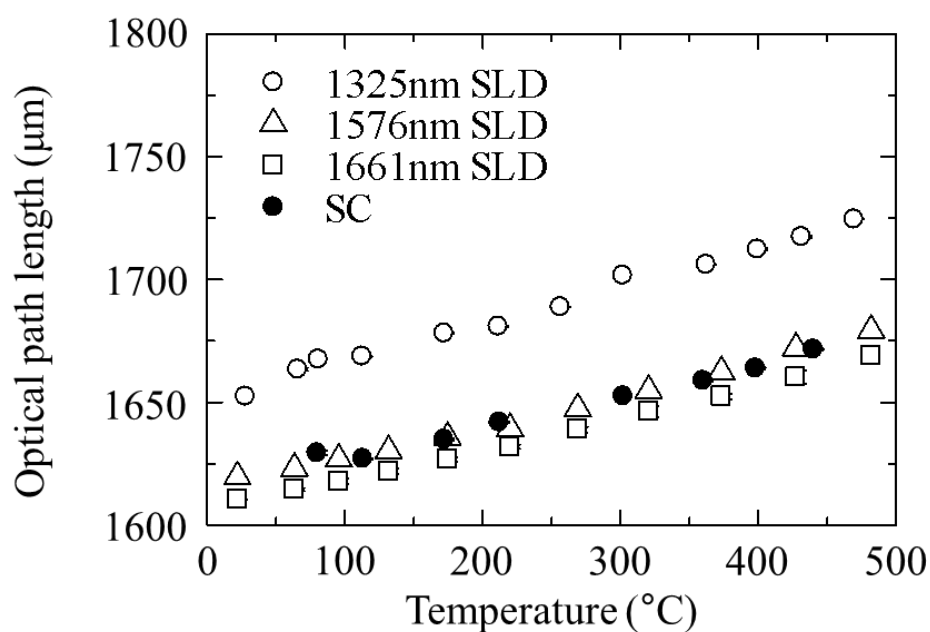
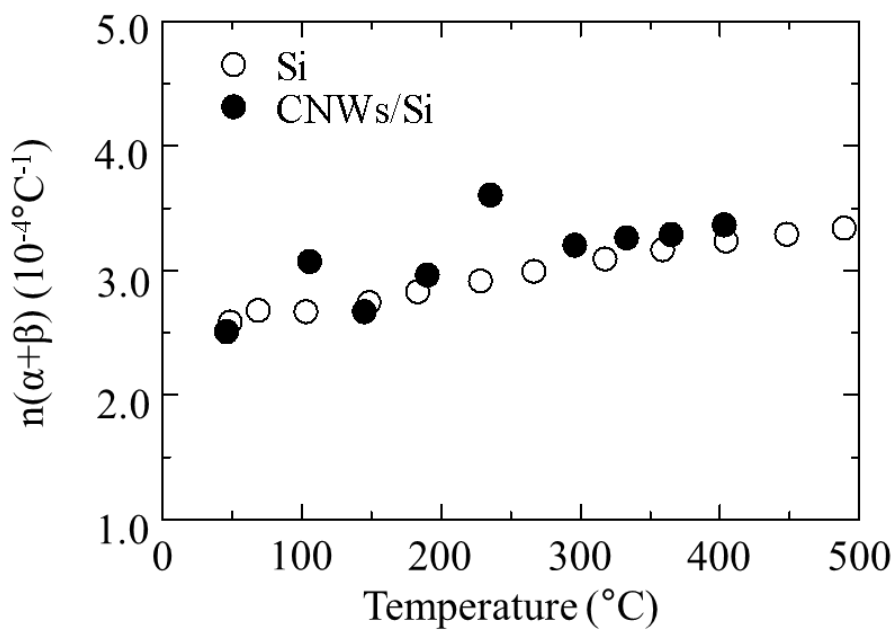
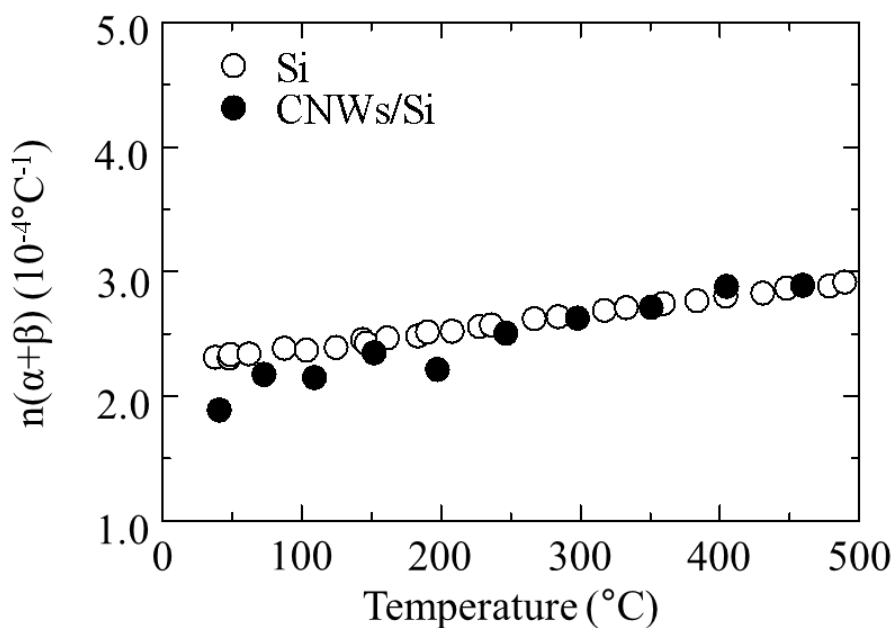


Fig.4.5 Optical path length of CNWs/Si as a function of temperature.

In order to evaluate the characteristics of optical path length against wavelengths, the  $n(\lambda)(\alpha + \beta(\lambda))$  of CNWs/Si was deduced from the result of Fig. 4.4 using eq. (4.1) and is shown in Fig. 4.6 ( (a) 1325 nm, (b) 1576 nm, (c) 1661 nm, and (d) SC). The  $n(\lambda)(\alpha + \beta(\lambda))$  for Si measured from the 800  $\mu\text{m}$ -thick Si substrate was also denoted in Fig. 4.6. The  $n(\lambda)(\alpha + \beta(\lambda))$ s of CNWs/Si were well corresponded to those of Si. These results indicate that the effect of the CNWs layer on temperature measurement was almost negligible for CNWs/Si. In our previous report on  $\text{SiO}_2/\text{Si}$  substrate, the peak position of the interference waveform of  $\text{SiO}_2/\text{Si}$  interface sinusoidally oscillated as the waveform was affected by that of  $\text{SiO}_2/\text{air}$  interface when  $\text{SiO}_2$  thickness changed.<sup>[18,19]</sup> On the other hand, in the case of CNWs, there would be no interference at CNWs/air because the light was absorbed by the CNWs or reflectance was low owing to poor surface roughness. Further work is required to clarify the influence of thickness or structure of CNWs on temperature measurement, but the position of interference of CNWs/Si interface was not affected by that of CNWs/air interface. In the cases of the SLDs, the optical path length increased with decreasing the wavelength at the same temperature. This is because the optical path length is multiplication of refractive index and thickness of medium, and the refractive index of silicon increases with decreasing the wavelength.<sup>[21]</sup> The values of optical path length for SC were close with those for 1576 and 1661 nm. The spectrum of SC was the center wavelength of approximately 1650 nm and FWHM of 500 nm.<sup>[13]</sup> Thus, the optical path length of SC would be decided by the center wavelength and the wideband FWHM affects to the coherent length, that is the width of the interference waveform. The slope of optical path length against temperature slightly increased with decreasing wavelength.

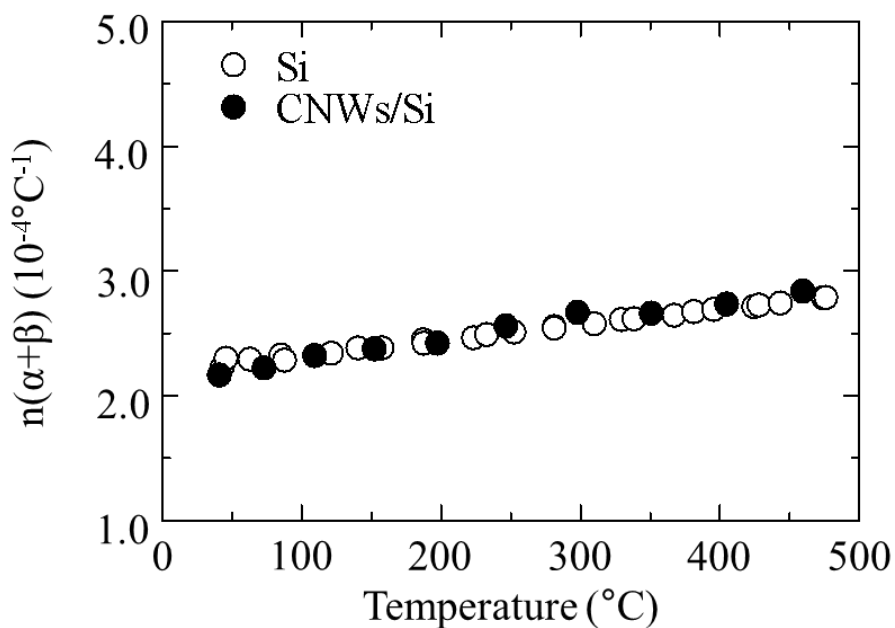


(a)

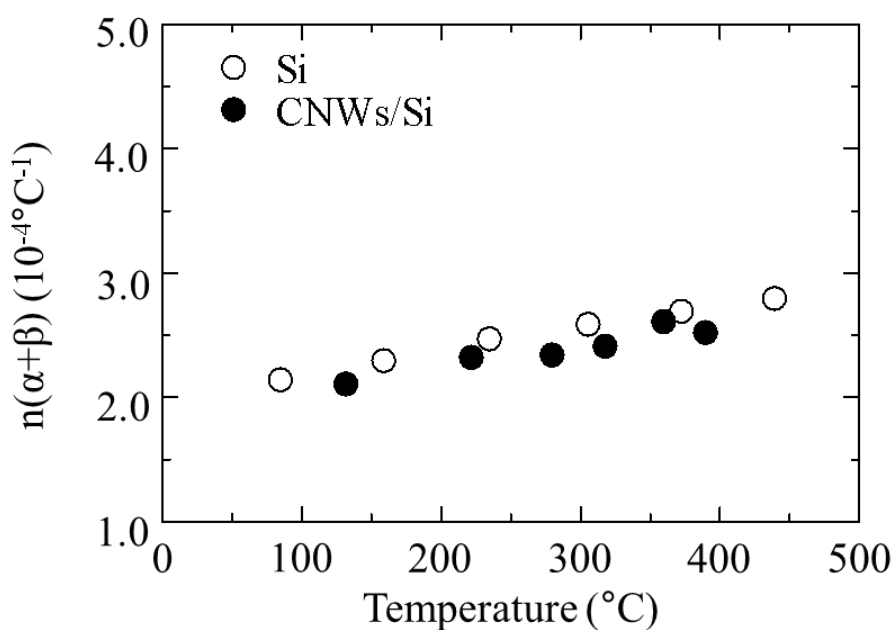


(b)

Fig. 4.6  $n(\lambda)(\alpha + \beta(\lambda))$  of CNWs/Si (a) SLD: 1325 nm (b) SLD: 1576 nm.



(c)



(d)

Fig. 4.6  $n(\lambda)(\alpha + \beta(\lambda))$  of CNWs/Si (c) SLD: 1661 nm (d) SC.

The  $n(\lambda)(\alpha+\beta(\lambda))$  calculated from Fig. 4.6 (d) is given by

$$n(\lambda)(\alpha + \beta(\lambda))_{\text{Si(SC)}} = -1.4 \times 10^{-11}\Delta T^2 + 2.6 \times 10^{-7}\Delta T + 1.9 \times 10^{-4} \quad (4.2)$$

$$n(\lambda)(\alpha + \beta(\lambda))_{\text{CNWs/Si(SC)}} = -7.3 \times 10^{-11}\Delta T^2 + 2.1 \times 10^{-7}\Delta T + 1.8 \times 10^{-4} \quad . \quad (4.3)$$

In the same way, the  $n(\lambda)(\alpha + \beta(\lambda))$  was calculated as shown in Table 4.1. The coefficient of temperature dependence of the refractive index  $\beta(\lambda)$  is larger as decreasing the wavelength while no change in the thermal expansion  $\alpha$  is against wavelengths.<sup>[21]</sup> The measurement accuracy was evaluated that the changes in optical path length per 1 °C were calculated to be 202 nm for 1325 nm, 180 nm for 1576 nm, and 176 nm for 1661 nm for 800  $\mu\text{m}$ -thickness Si substrate. These results indicate that the high accuracy on the temperature measurement is achieved as decreasing the wavelength because the resolving power of the optical path length is constant.

Table 4.1 the  $n(\lambda)(\alpha+\beta(\lambda))$  of Si and CNWs/Si ( $10^{-4} \text{ }^\circ\text{C}^{-1}$ )

	SC	SLD 1325 nm	SLD 1376 nm	SLD 1661 nm
Si	1.92	2.49	2.24	2.20
CNWs/Si	1.74	2.19	1.75	1.96

## 4.4 Summary

In this study, the temperature measurements of 450- $\mu\text{m}$ -thickness Si substrate with 500-nm-height-CNWs were demonstrated using optical low-coherence interferometer. SC and three SLDs at the center wavelengths of 1325 nm, 1576 nm, and 1661 nm were used as light sources. Optical path length monotonically increased with the temperature and it is found that the temperature of CNWs/Si substrate was successfully measured from the optical path length. In order to evaluate the characteristics of optical path length against wavelengths, the  $n(\lambda)(\alpha + \beta(\lambda))$  of CNWs/Si was deduced. The  $n(\lambda)(\alpha + \beta(\lambda))$ s of CNWs/Si were well corresponded to those of Si. These results indicated that the effect of the CNWs layer on temperature measurement was almost negligible for CNWs/Si. The wavelength dependence on the optical path length was also investigated. The optical path length increased with decreasing the wavelength at the same temperature. The values of optical path length for SC were close to those for 1576 and 1661 nm. The results indicated that the optical path length of SC was decided by its center wavelength and the coherent length was affected by the wideband FWHM. These results indicate that the high accuracy on the temperature measurement is achieved as decreasing the wavelength.

## References for Chapter 4

- [1] H. Watanabe, H. Kondo, M. Sekine, M. Hiramatsu, and M. Hori, *Jpn. J. Appl. Phys.*, **51**, 01AJ07 (2012).
- [2] S. Kondo, H. Kondo, M. Hiramatsu, M. Sekine, and M. Hori, *Appl. Phys. Exp.*, **3**, 045102 (2010).
- [3] W. Takeuchi, H. Kondo, T. Obayashi, M. Hiramatsu, and M. Hori, *Appl. Phys. Lett.*, **98**, 123107 (2011).
- [4] W. Takeuchi, M. Ura, M. Hiramatsu, Y. Tokuda, H. Kano, and M. Hori, *Appl. Phys. Lett.*, **92**, 213103 (2008).
- [5] W. Takeuchi, K. Takeda, M. Hiramatsu, Y. Tokuda, H. Kano, S. Kimura, O. Sakata, H. Tajiri, and M. Hori, *Phys. Status Solidi A* **207**, 139 (2009).
- [6] S. Kondo, S. Kawai, W. Takeuchi, K. Yamakawa, S. Den, H. Kano, M. Hiramatsu, and M. Hori, *J. Appl. Phys.*, **106**, 094302 (2009).
- [7] K. Takeda, Y. Tomekawa, T. Shiina, M. Ito, Y. Okamura, and N. Ishii, *Jpn. J. Appl. Phys.*, **43**, 7737 (2004).
- [8] C. Koshimizu, T. Ohta, T. Matsudo, and S. Tsuchitani, M. Ito, *Appl. Phys. Express* **3**, 056201 (2010).
- [9] H. Yamamoto, H. Kuroda, M. Ito, T. Ohta, K. Takeda, K. Ishikawa, H. Kondo, M. Sekine, and M. Hori, *Jpn. J. Appl. Phys.*, **51**, 016202 (2012).
- [10] S. Takahashi, R. Kawauchi, S. Takashima, S. Den, T. Katagiri, H. Kano, T. Ohta, M. Ito, T. Suzuki, K. Takeda, and M. Hori, *Jpn. J. Appl. Phys.*, **51**, 076502 (2012).
- [11] T. Ohta, C. Koshimizu, K. Kawasaki, K. Takeda, and M. Ito, *J. Appl. Phys.*, **105**, 13110 (2009).

## Chapter 4

- [12] C. Koshimizu, T. Ohta, T. Matsudo, S. Tsuchitani, and M. Ito, *Jpn. J. Appl. Phys.*, **51**, 046201 (2012).
- [13] T. Hiraoka, T. Ohta, M. Ito, N. Nishizawa, and M. Hori, *Jpn. J. Appl. Phys.*, (2013) . accept for publication.
- [14] N. Nishizawa and T. Goto, *Jpn. J. Appl. Phys.*, **40**, L365 (2001).
- [15] T. Hori, N. Nishizawa, T. Goto, and M. Yoshida, *J. Opt. Soc. Amer. B*, **21**, 1969 (2004).
- [16] T. Hori, J. Takayanagi, N. Nishizawa, and T. Goto, *Opt. Expr.*, **12**, 317 (2004).
- [17] J. Takayanagi and N. Nishizawa, *Jpn. J. Appl. Phys.*, **45**, L441 (2006).
- [18] N. Nishizawa and J. Takayanagi, *J. Opt. Soc. Amer. B*, **24**, 1786 (2007).
- [19] N. Nishizawa and M. Hori, *Appl. Phys. Exp.*, **1**, 022009 (2008).
- [20] N. Nishizawa, H. Mitsuzawa, J. Takayanagi, and K. Sumimura, *J. Opt. Soc. Amer. B*, **26**, 426 (2009).
- [21] J. A. McCaulley, V. M. Donnelly, M. Vernon, and I. Taha, *Phys. Rev. B*, **49**, 7408 (1994).

## Chapter 5

# Optical-Fiber-Type Broadband Cavity Ring-Down Spectroscopy Using Wavelength-Tunable Ultrashort Pulsed Light

### 5.1 Introduction

As described in Section 1.4, high-sensitive absorption spectroscopy is strongly requested in biological and medical fields. Optical-fiber-type cavity ring-down spectroscopy (CRDS) is a powerful technique suitable for very small liquid samples. It is based on measurements of the ring-down time of laser intensity in a loop made of optical waveguide material. This ring-down time changes as small liquid samples containing absorbing species are introduced into the loop. Fiber and fiber components are designed to confine the signal light inside the fiber core with smaller loss in comparison with the conventional CRDS with high reflective mirrors due to elimination of the loss of the optical component.

Various cavities of Optical-fiber-type CRDS have been reported as side-coupled into the core of the fiber with laser pulse<sup>[1,2]</sup>, fiber Bragg grating<sup>[3,4]</sup>, the gap between the fibers<sup>[5,6]</sup>, evanescent waveguide using prism<sup>[7,8]</sup> or tapered fiber.<sup>[9]</sup> An

evanescent-waveguide cavity using a tapered fiber eliminates the loss owing to the coupling between laser pulse and cavity and realizes the high sensitivity measurement system.

Generally, a high-power laser with a single-wavelength or narrow bandwidth, such as the tunable dye laser or the laser diode, has been used as the light source; cavity mirrors also cover a narrow bandwidth owing to ultrahigh reflection. Hence, when such lasers or mirrors are employed in a large measurement system or with several light sources of different wavelength, absorption spectra are achieved.

The wavelength tunable soliton pulse generated in fibers using soliton self-frequency shift (SSFS) is attractive light source. The theoretical discovery of soliton in fibers was demonstrated by Zakharov and Shabat, and Hasegawa and Tappert in the 1970s.<sup>[10,11]</sup> The SSFS was experimentally demonstrated and then the theory of SSFS was established.<sup>[12,13]</sup> Firstly, Beaud et al. demonstrated the 1.37–1.49  $\mu\text{m}$  wavelength-tunable sources using SSFS.<sup>[14]</sup> The center wavelength of the generated soliton pulse is red shifted continuously and monotonically as the fiber input power is increased, and many generation method of wavelength tunable soliton pulses using various fibers have been reported.<sup>[15-18]</sup>

Recently, compact, wavelength-tunable, ultrashort pulse light sources from 1.55 to 2.0  $\mu\text{m}$  have been demonstrated using a femtosecond pulse laser and nonlinear fibers.<sup>[19-23]</sup> As the fiber input power is increased, the center wavelength of the generated soliton pulse is red-shifted continuously and monotonously. The generated pulses are clear  $\text{sech}^2$ -shaped ultrashort soliton light pulses. Thus, the wavelength can be changed by the intensity-modulation of the femtosecond pulse laser and the absorption spectrum is obtained easily with no optical loss.

## Chapter 5

In this chapter, an optical-fiber-type broadband CRDS system that uses wavelength-tunable ultrashort pulsed light and an evanescent-waveguide using a tapered fiber as a sensing component is proposed to measure the absorption spectra without optical loss and construct the all optical fiber measurement system.

It is well known that diabetes is a disease that is severely harmful for human health. Intensive blood glucose control is very important technique in proper diabetes management. Blood glucose measurement methods using near-infrared spectroscopy are expected as a noninvasive technique for the management of diabetes. The key issue for the practical use is to improve the signal to noise ratio so that very low glucose absorption can be detected. As a first step, water containing glucose from 1 to 20% was measured by the CRDS system to demonstrate its broadband-spectral feature.

## 5.2 Experimental

Figure 5.1 shows the optical setup of the optical-fiber-type CRDS system. This system employs the Mach–Zehnder interferometer for enhancing the signal-to-noise ratio. A passively mode-locked, Er-doped, ultrashort pulse fiber laser was used as a pulse light source. It generates 100 fs ultrashort pulses at a repetition rate of 50 MHz. The center wavelength is 1556 nm. The power-controlled pulses were coupled into a polarization maintaining fiber (PMF) with slightly high nonlinearity. Owing to the soliton self-frequency shift in this PMF, the center wavelengths of the output pulses could be monotonically tuned as a function of the fiber input power.

Figure 5.2 shows the wavelength tunability light source using soliton self-frequency shift at output of ND-HNLF. It has been realized the tunability of center wavelength from 1620nm to 1690 nm with input pulse power modulation at the half wavelength plate and polarization beam splitter in Fig. 1.1.

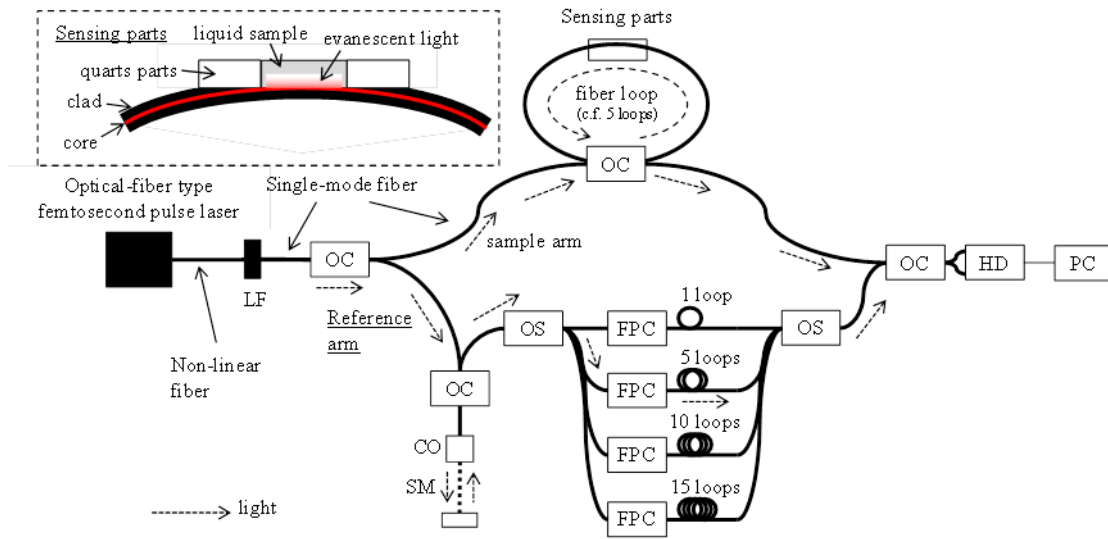


Fig. 5.1 Optical setup of optical-fiber type cavity ring-down spectroscopy system; dotted arrow denotes light pathway in the case of 5 loop. (LF: optical low pass filter, OC: optical fiber coupler, CO: collimator lens, SM: scanning mirror, OS: automatic optical switching module, FPC: optical fiber-type polarization controller: HD: homodyne-type photo detector, PC: personal computer).

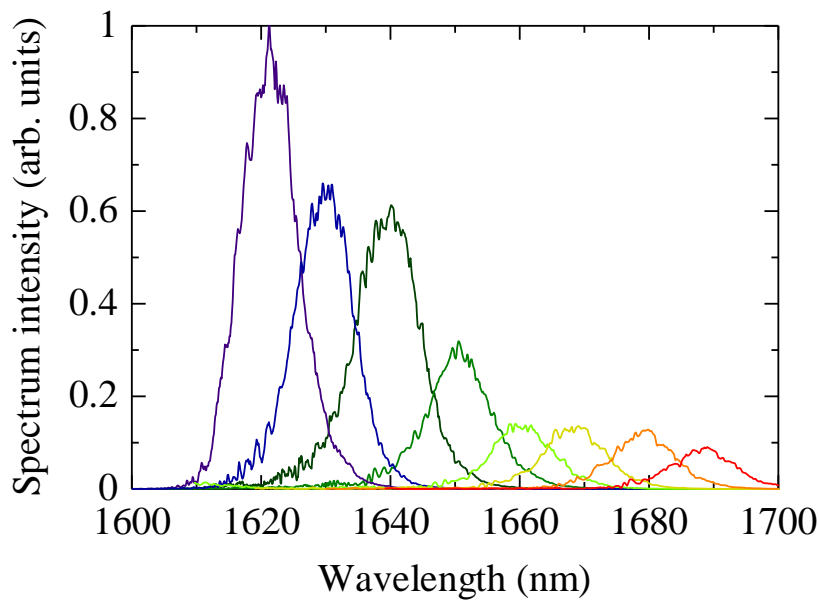


Fig. 5.2 Wavelength tunability of center wavelength of soliton pulse

The output pulses were coupled into a fiber coupler and were divided into a signal arm and a reference arm. The sensing component was made of single-mode optical fiber, which photograph is shown in Fig. 5.3, the clad part of which was stripped off to expose samples to the evanescent wave of the light propagating in the core. The sample was placed on the stripped core. This sensing component has no significant wavelength dependence in the single-mode wavelength region and is suitable for miniaturizing the system. A scanning mirror was used to obtain the interference waveform between signal and reference beams. In this system, loop fibers in the reference beam with different optical delay lengths were selected by using an optical switching module to obtain the ring-down plot. The optical delay lengths of the loop fibers were set to be 1, 5, and 10 times as long as that of a fiber loop in the signal beam to obtain interference waveforms. A homodyne photo detector was used to enhance the signal-to-noise ratio.

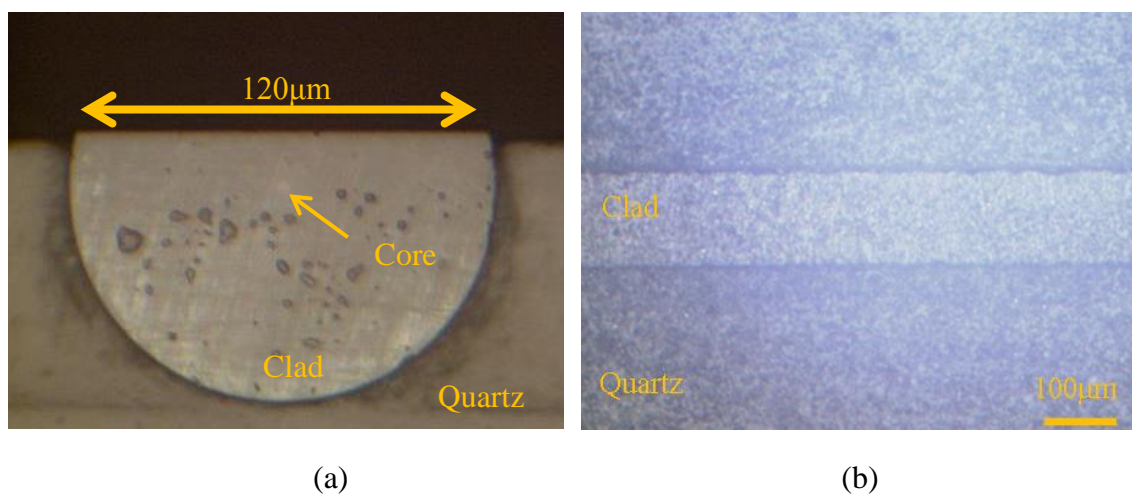
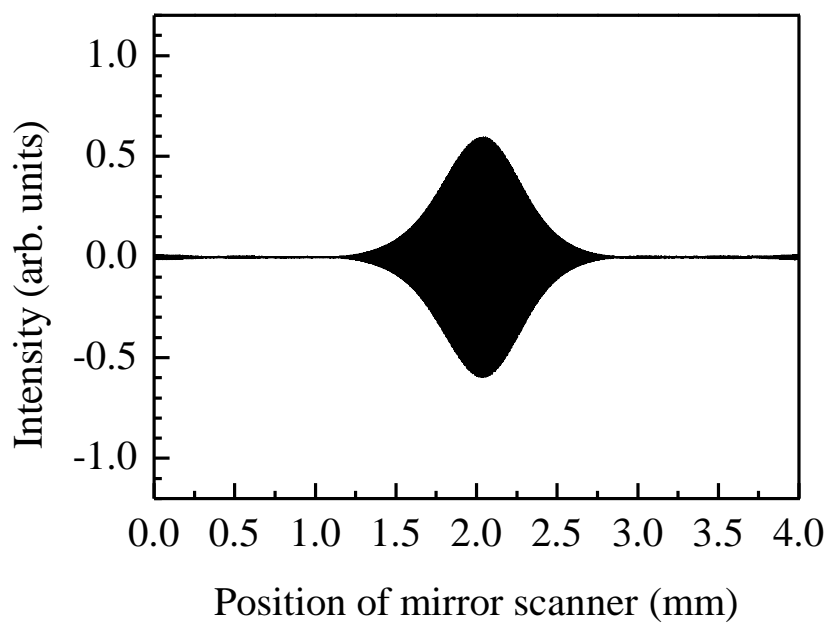


Fig. 5.3 Photograph of the sensing component. (a) cross section, (b) top view.

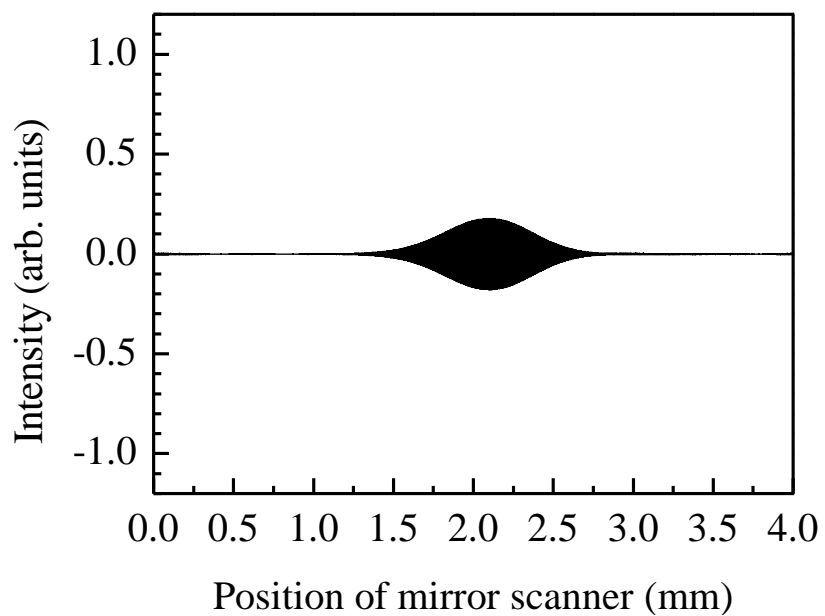
## 5.3 Results and Discussion

### 5.3.1 Ring-down measurement on single-wavelength

Figure 5.4 shows the interference waveforms without a sample, at a wavelength of 1630 nm in the cases of (a) 1-loop path, (b) 5-loop path, (c) 10-loop path. When the optical delay line of the 1-loop path in the reference arm is selected using the optical switching module and the reference mirror is scanned, an interference waveform is obtained as shown in Fig. 5.4(a). The waveform is obtained because the optical path length of the reference arm with a 1-loop path delay length corresponds to that of a round fiber loop being propagated by a pulse 1 time in the signal arm. Interference waveforms as shown in Fig. 5.4 (b) and (c) were obtained by changing optical delay lines with 5 and 10-loop paths using the optical switching module. Thus, ring-down plots are derived from the peak intensities of the waveforms as a function of the optical delay length.

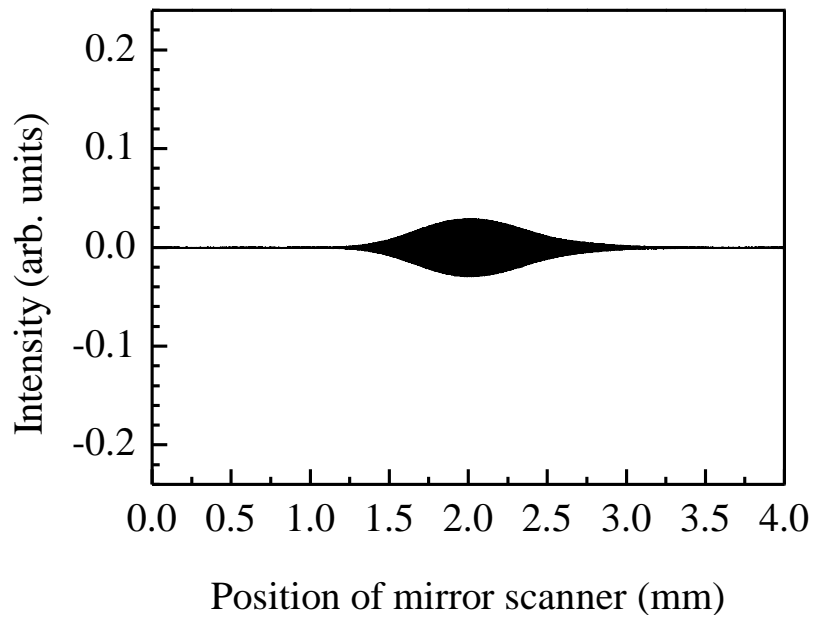


(a)



(b)

Fig. 5.4 Interference waveform without a sample at a wavelength of 1630 nm, (a) 1-loop path, (b) 5-loop path



(c)

Fig. 5.4 Interference waveform without a sample at a wavelength of 1630 nm, (c) 10-loop path.

Figure 5.5 shows the ring-down plot for various concentrations of glucose diluted by water at a wavelength of 1630 nm, obtained from the intensities of the interference waveforms. The ring-down plot for diluted water was also measured as a reference sample. The interference intensity decreased exponentially with the increase in the number of propagation times around the fiber loop; the optical path length of the round trip was approximately 3 m. The absorption length  $d$  in eq. (1.5) was evaluated to be 1.3 mm. From eq. (1.5), the absorbance of 5% glucose was estimated to be 0.013 against the diluted water as a reference sample; this value is in good agreement with that measured using the absorption spectrophotometer. The correlation coefficient of the calibration curve was estimated to be 0.997 in the glucose concentration range of 0–20%.

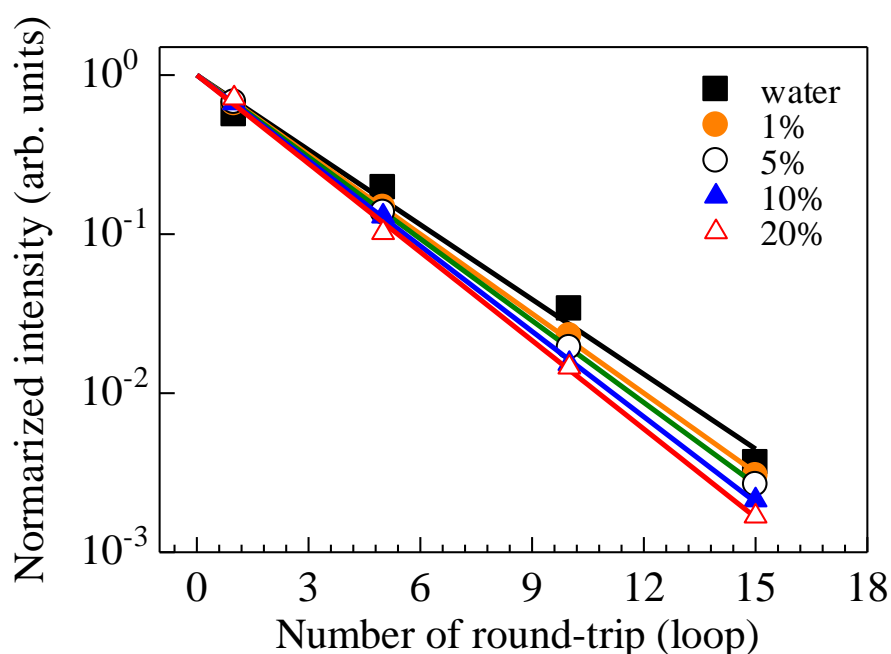


Fig. 5.5 Ring-down plot for various concentrations of glucose.

### 5.3.2 Absorption measurement of glucose on multi-wavelength

Plots from 1620 to 1690 nm in Fig. 5.6 show the absorption spectra for several concentrations of glucose, measured using the broadband CRDS. The solid line denotes the absorption spectra measured by the absorption spectrophotometer. Figure 5.7 shows the calibration curve from 1620nm to 1690nm. In addition, the regression equation of glucose concentration  $C_g$  in the multi-wavelength is calculated by a multiple regression analysis using the calibration curve,

$$C_g = 251A_{1620} + A_{1630} - 47A_{1640} - 29A_{1650} - 149A_{1660} + 220A_{1670} - 299A_{1680} + 1487A_{1690} + 6 \times 10^{-3} \quad (5.1)$$

Here,  $A_x$  represents the absorbance at each wavelength. Table 5.1 shows the standard deviation of the concentration of glucose solution was measured using a single-wavelength and multi-wavelength. The measurement error for 20% glucose was improved from 1.1%, estimated from the absorbance of single-wavelength, to 0.6%, estimated using multiple linear regression analysis. The sensitivity of this system can be further improved by increasing the number of propagation times around the fiber loop.

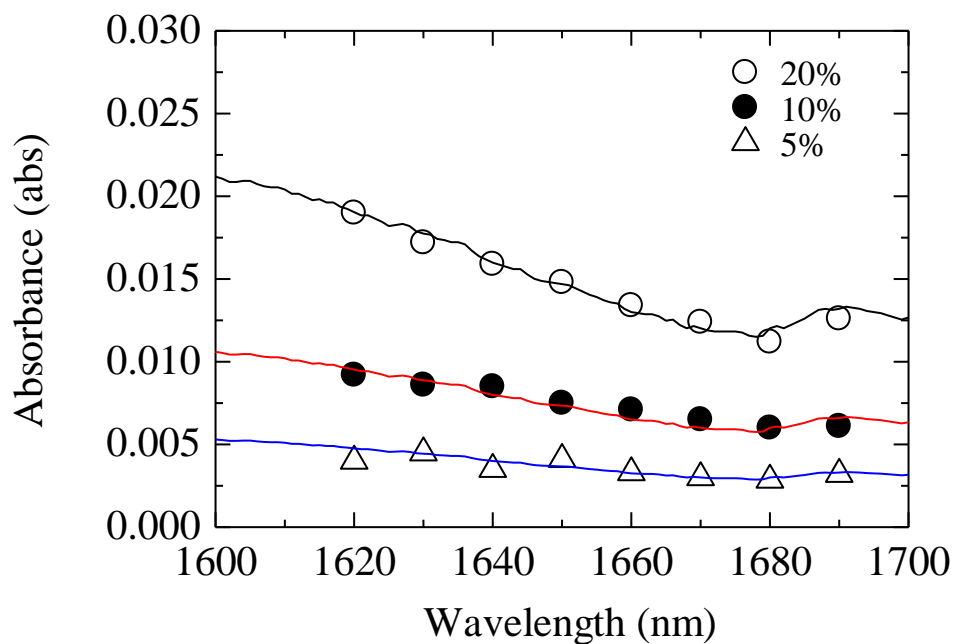


Fig. 5.6 Absorption spectra of various concentrations of glucose.

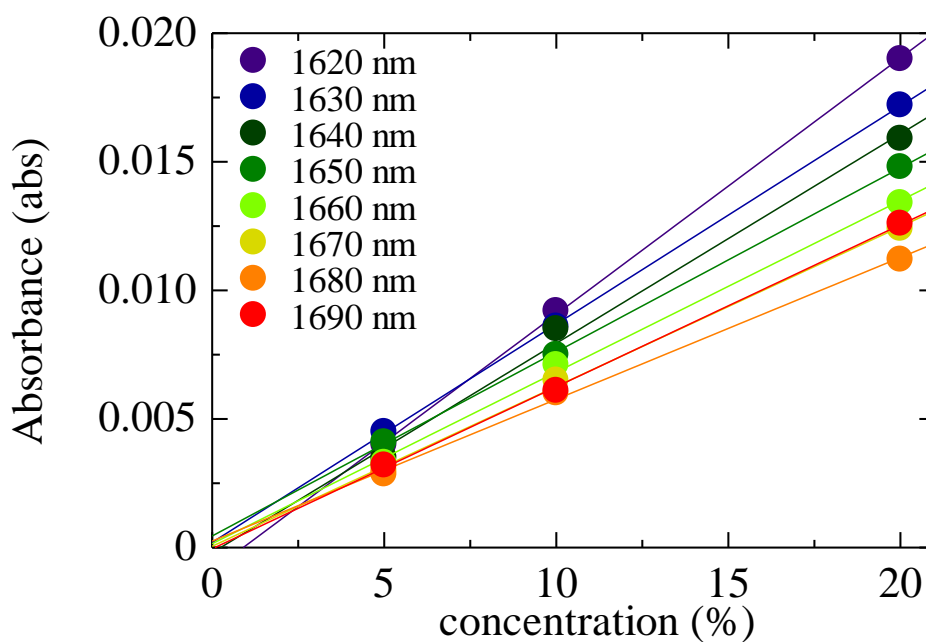


Fig. 5.7 Absorption spectra of various concentrations of glucose.

Table 5.1 Standard deviation of concentration of glucose.

Concentration (%)	Single-wavelength (%)	Multi-wavelength (%)
5	1.357	0.754
10	1.122	0.604
20	1.085	0.573

## 5.4 Summary

An optical-fiber-type broadband cavity ring-down spectroscopy system that employs wavelength-tunable ultrashort pulsed light was presented. The absorption spectrum of glucose was successfully obtained in the wavelength region from 1620 to 1690 nm by varying the wavelength using a wavelength-tunable ultrashort pulsed light. The measurement deviation of concentration was improved by using multiple linear regression analysis of absorption spectra.

These results demonstrate that the optical-fiber type cavity ring-down spectroscopy system has a potential to measure the broadband absorption spectra with high sensitivity. The proposed system will be a powerful tool for analyzing precious bio-samples etc. because of its broadband, high-sensitive, and compact features.

## References for Chapter 5

- [1] B. A. Gibson and C. Vallance, *Boomerang Trans.*, **1**, 26 (2006).
- [2] R. S. Brown and I. Kozin, Z. Tong, R. D. Oleschuk, and H.-P. Loock, *J. Chem. Phys.*, **117**, 10444 (2002).
- [3] M. Gupta, H. Jiao, and A. O'Keefe, *Opt. Lett.*, **27**, 1878 (2002).
- [4] S. Pu and X. Gu, *Opt. Lett.*, **34**, 1774 (2009).
- [5] N. Trefiak, J. Barnes, R. Li, Z. Tong, R. D. Oleschuk and H.-P. Loock, *Anal. Chem.*, **76**, 6594 (2004).
- [6] N. Trefiak, Z. Tong, T. McCormick, J. Barnes, R. Li, R. D. Oleschuk and H.-P. Loock, *IEEE LEOS NEWSLETTER*, **195**, 5 (2005).
- [7] L. van der Sneppen, F. Ariese, C. Gooijer, and W. Ubachs, *Annu. Rev. Anal. Chem.*, **2**, 13 (2009).
- [8] M. H.-Zadeh, and K. J. Vahala, *Opt. Expr.*, **14**, 10800 (2006).
- [9] P. B. Tarsa, A. D. Wist, P. Rabinowitz, and K. K. Lehmann, *Appl. Phys. Lett.*, **85**, 4523 (2004).
- [10] V. E. Zakharov and A. B. Shabat, *Sov. Phys. JETP*, **34**, 62 (1972).
- [11] A. Hasegawa and F. Tappert, *Appl. Phys. Lett.*, **23**, 142 (1973).
- [12] F. M. Mitschke and L. F. Mollenauer, *Opt. Lett.*, **11**, 659 (1986).
- [13] J. P. Gordon, *Opt. Lett.*, **11**, 662 (1986).
- [14] P. Beaud, W. Hodel, B. Zysset, and H. P. Weber, *IEEE J. Quantum Electron.*, **QE-23**, 1938 (1987).
- [15] J. H. Lee, J. V. Howe, C. Xu, and X. Liu, *IEEE J. Sel. Topics Quantum Electron.*, **14**, 713 (2008).

## Chapter 5

- [16] M.-C. Chan, S.-H. Chia, T.-M. Liu, T.-H. Tsai, M.-C. Ho, A. A. Ivanov, A. M. Zheltikov, J.-Y. Liu, H.-L. Liu, and C.-K. Sun, *IEEE Photon. Technol. Lett.*, **20**, 900 (2008).
- [17] N. Ishii, C. Y. Teisset, S. Köhler, E. E. Serebryannikov, T. Fuji, T. Metzger, F. Krausz, A. Baltuška, and A. M. Zheltikov, *Phys. Rev. E*, **74**, 036617 (2006).
- [18] M. E. Masip, A. A. Rieznik, P. G. König, D. F. Grosz, A. V. Bragas, and O. E. Martinez, *Opt. Lett.*, **34**, 842 (2009).
- [19] J. Takayanagi, T. Sugiura, M. Yoshida, and N. Nishizawa, *IEEE Photon. Technol. Lett.*, **18**, 2284 (2006).
- [20] N. Nishizawa, *IEEE J. Quantum Electron.*, **45**, 1446 (2009).
- [21] N. Nishizawa, R. Okamura, and T. Goto, *Jpn. J. Appl. Phys.*, **39**, L409 (2000).
- [22] N. Nishizawa, and K. Takahashi, *Opt. Lett.*, **36**, 3780 (2011).
- [23] N. Nishizawa, R. Okamura, and T. Goto, *Jpn. J. Appl. Phys.*, **38**, 4768 (1999).

# Chapter 6

## Conclusions

### 6.1 Summary of This Thesis

In this thesis, the accurate temperature monitoring of substrates and the high sensitive monitoring of biomaterials was investigated aiming to extend the application of wavelength-tunable ultrashort-pulse laser and supercontinuum (SC) light to the monitoring of plasma processes and bio-sensing processes.

In Chapter 1, ultrashort-pulse laser, wavelength-tunable ultrashort-pulse laser, and SC light were introduced as backgrounds for novel light sources. Moreover, backgrounds for monitoring of substrate temperature for plasma processing and high sensitive monitoring and analysis for biomaterials were introduced as novel applications of those lights. Finally, the purpose and overview of this thesis were presented.

In Chapter 2, the theory of the low-coherent interferometry, which is based on the Michelson interferometer, and cavity ring-down spectroscopy (CRDS) used in this study were presented. At first, the principle of the interferometry with high and low temporal coherence light was described. Next, the theory of substrate temperature measurement was presented. Finally, the principle of CRDS and introduce the earlier study of fiber-type CRDS were presented.

In Chapter 3, the high-resolution temperature measurement of Si wafer was presented using optical low-coherence interferometer employing SC. The measurement accuracy on wafer temperature is improved by achieving higher resolution of optical path length of wafer. The maximum resolving power of the optical path length of the media on the low-coherence interferometry depends on the coherent length which determined by the spectrum profile and wavelength of the light source. The interferences at the front and back interfaces of the media are combined into an overlapping interference when the optical path length of the media is shorter than the coherence length of the light source. I focused on low-noise, ultra-flat, and highly coherent SC generated using ultra-short laser pulse and optical fibers as the light source. The SC has a broader spectrum than superluminescent diodes (SLDs), which leads that the coherent length of SC is typically several  $\mu\text{m}$  while that of SLD is 20  $\mu\text{m}$ . To employ SC for in this system, we the wavelength-dispersion of SC in Si wafer was compensated using a Si mirror as a reference mirror. It was confirmed that the interference waveforms of SC lights at front and back surfaces of Si wafer are sharper than those of SLD lights.

The measurement accuracy on the temperature using SC was improved to be  $\pm 0.4^\circ\text{C}$  from  $\pm 1.0^\circ\text{C}$  for SLD. The temperatures of Si wafer and  $\text{SiO}_2$  thin film wafer were simultaneously measured by using SC on 8.55- $\mu\text{m}$ -thickness  $\text{SiO}_2$  film / 800- $\mu\text{m}$ -thickness Si substrate. Measurement deviations of temperature were  $\pm 0.9^\circ\text{C}$  for Si or  $\pm 11.6^\circ\text{C}$  for  $\text{SiO}_2$ . The change on the optical length of  $\text{SiO}_2$  against temperature variation is smaller than that of Si due to smaller refractive index and thinner thickness of  $\text{SiO}_2$  layer. These results showed that a simultaneous measurement

of SiO<sub>2</sub> film thickness and Si wafer temperature has been successfully carried out using a SC interferometry.

In Chapter 4, the temperature measurements of 450- $\mu\text{m}$ -thick Si substrate with 500-nm-height-CNWs were demonstrated using optical low-coherence interferometer. SC and three SLDs at the center wavelengths of 1325 nm, 1576 nm, and 1661 nm were used as light sources. Optical path length monotonically increased with the temperature and it is found that the temperature of CNWs/Si substrate was successfully measured from the optical path length.

The characteristics of optical path length against wavelengths were investigated. The results indicated that the effect of the CNWs layer on temperature measurement was almost negligible for CNWs/Si. The wavelength dependence on the optical path length was also investigated. The optical path length increased with decreasing the wavelength at the same temperature. The values of optical path length for SC were close to those for 1576 and 1661 nm. The results indicated that the optical path length of SC was decided by its center wavelength and the coherent length was affected by the wideband FWHM. These results indicated that the high accuracy on the temperature measurement is achieved as decreasing the wavelength.

In Chapter 5, An optical-fiber-type broadband cavity ring-down spectroscopy system that employs wavelength-tunable ultrashort pulsed light was presented. The absorption spectrum of glucose was successfully obtained in the wavelength region from 1620 to 1690 nm by varying the wavelength using a wavelength-tunable ultrashort pulsed light. The measurement deviation of concentration was improved by using multiple linear regression analysis of absorption spectra. These results demonstrated that the optical-fiber type cavity ring-down spectroscopy system has a potential to

measure the broadband absorption spectra with high sensitivity. Therefore, the system would be applied to in-situ monitoring tool with ultra-high sensitivity for surface reactions in plasma processes as well as bio-applications.

## 6.2 Scopes of Future work

In this thesis, the accurate temperature monitoring tool of substrates was presented using SC light. The accurate monitoring of substrate temperature will be a powerful tool for realize autonomous plasma nano-fabrication processes. As described in Section 1.3, according to ITRS, the manufacturing variations of gate must be controlled from 3 to 2 nm ( $3\sigma$ ) in the 45 nm generation and will be less than 1 nm in 20 nm generation which is scheduled in 2015. In the generation, temperature fluctuation control or autonomous radical-density control with precise temperature measurement less than 1°C will be necessary. The temperature monitoring system will be a key technology for satisfying the next generation requirement in the plasma etching process. Moreover, besides the etching process, the system will be more powerful tool in plasma enhanced plasma chemical vapor deposition (PECVD) processes. In this thesis, the system was successfully applied to CNW thin films on Si substrates as a PECVD process but will be applicable to various kinds of thin film deposition processes. Thus, the system will be a key tool for realizing autonomously controlled plasma etching and deposition processes. Moreover, it will be suitable for not only plasma processes but also various processes to control the substrate temperature, for example, molecular beam epitaxy, deep level transient spectroscopy and so on. Semiconductor-manufacturing processes could be controlled more accurately using this monitoring system.

Furthermore, the high-sensitive monitoring tool of biomaterials was presented using a compact wavelength-tunable ultrashort-pulse laser. The tool will be a powerful tool for not only analyzing precious bio-samples but also monitoring the quality of thin film fabricated in plasma process because of its broadband, high-sensitive, and compact features. If the system is applied to the CNWs deposition process, the absorption of the CNWs will be obtained even in the initial stage of the deposition. The control of quality in the initial stage is a key issue for improving the CNWs quality and the morphological structure.<sup>[1]</sup> To apply the system to the deposition process, there are some problems such as light absorption caused by the heat of the substrate and change in the refractive index due to the deposited film. To improve this system, more broaden light source and high-sensitive detector and more information that thin film has effect on interference waveform are demanded. From the observations of the initial stages, the control of the qualities and morphologies of CNWs films will be also realized using the CRDS system. Thus, the monitoring tools of substrate temperatures and surface reactions as well as radical densities will be indispensable for realizing autonomously controlled plasma nanofabrication processes.

Recently, more broadband and high-resolution wavelength-tunable ultrashort-pulse lasers have been developed. Using these lasers and this system, high-sensitive, high-resolution, ultrafast spectroscopy in the visible to infrared region will be realized for detecting and analyzing substances with very small volume and very low density or for monitoring the quality of very thin film fabricated in various processes as well as plasma ones.

## Reference for Chapter 6

- [1] M. Hiramatsu, M. Hori, “Carbon Nanowalls, Synthesis and Emerging Applications”, Springer-Verlag (2010).

# Acknowledgements

The present research has been performed in Prof. Hori and Prof. Sekine Laboratory, Department of Electrical Engineering and Computer Science, Nagoya University. The research results presented in this thesis could not have been obtained without the support of the following people.

First and foremost, I would like to express my deep appreciation to Prof. Masaru Hori, Department of Electrical Engineering and Computer Science, Nagoya University, for having given me the opportunity to pursue a Ph. D. in his group. I could not progress rapidly in my understanding of this research without His guidance, valuable advices, and encouragements. I would also like to deeply appreciate my co-supervisor, Prof. Makoto Sekine, Plasma Nanotechnology Research Center, Nagoya University, for providing his wealth of experience and wonderful discussions.

I would like to express my gratitude to Prof. Kodo Kawase, Department of Electrical Engineering and Computer Science, Nagoya University and Prof. Noritsugu Umehara, Department of Mechanical Engineering, Nagoya University for valuable comments and guidance in this thesis.

I would like to express my gratitude to Prof. Masafumi Ito, Department of Electrical and Electronic Engineering, Meijo University, Prof. Mineo Hiramatsu, Department of Electrical and Electronic Engineering, Meijo University, Associate Prof. Takayuki Ohta, Department of Electrical and Electronic Engineering, Meijo University, and Prof. Norihiko Nishizawa, Department of Electrical Engineering and Computer Science, Nagoya University.

I am also grateful to the entire staff in Hori and Sekine's Lab., Prof. Kenji Ishikawa,

## Acknowledgements

Associate Prof. Hiroki Kondo, Associate Prof. Satomi Tajima, Assistant Prof. Keigo Takeda, Associate Prof. Noboru Ebizuka, and Dr. Fengdong Jia, Dr. Jagath Kularatne , Dr. Hiromasa Tanaka, Ms. Hiroko Mizuno, Dr. Hiroshi Hashizume, Meijo University, Ms. Mari Inoue, Wakayama University for their fruitful discussion and valuable comments.

I would like to acknowledge Dr. Shoji Den, Dr. Koji Yamakawa, Dr. Shunji Takahashi in Katagiri Engineering Co., Ltd., Dr. Hiroyuki Kano in NU Eco-Engineering Co., Ltd., for constructing and modifying the experimental equipments.

I appreciate Prof. Bill Graham, School of Mathematics and Physics, Queen's University Belfast, Belfast, and Prof. Timo Gans, Prof. Deborah O'Connell, Department of Physics, University of York, Dr. Kari Niemi, Dr. Joao Santos Sousa, Dr. Qais Al-Gwari, Mr. Mahmoud Alkawareek, Ms. Laura Cox, Ms. Lucy Graham, Mr. Arthur Greb, Mr. Colin Kelsey, Mr. Colm O'Neill, Mr. Lucas Schaper, Mr. Mujahid Zaka-ul-Islam, Mr. Andrew Gibson, Dr. Charlie Mahony, School of Engineering, University of Ulster and Assistant Prof. Tomoyuki Murakami, Department of Energy Sciences, Interdisciplinary Graduate School of Science and Engineering, Tokyo Institute of Technology for giving me the opportunity to study in his group. To whom it concerns with Japan Society for the Promotion of Science International Training Program, I am heartily grateful for having given me unforgettable opportunity to experience the motivation for world-wide research area and constantly sufficient supports. I believe that every experience that I have had in Prof. Graham's laboratory will help promote my study in the future.

The author thanks sincerely Mr. Tetsunori Kageyama, Mr. Kouichi Yamamoto, Mr. Takayoshi Tsutsumi, Mr. Atsushi Ando, Mr. Ryuhei Kokuo, Mr. Tetsuya Yamada, Mr.

## Acknowledgements

Yoshiro Fukushima, Mr. Jun Yoshimi, Mr. Syun Inukai, Mr. Kazutaka Nishimura, Mr. Masatoshi Natsume, Mr. Kyohei Shibata, Mr. Tsubasa Kotetsu and Mr. Hiroto Kato who aided their experimental works carried out in this thesis and also expressed their valuable suggestions and discussions.

A big thanks to my colleagues in Prof. Horii and Prof. Sekine's Lab, Dr. Tsuyoshi Yamaguchi, Dr. Hiroto Inui, Dr. Hiroshi Yamamoto, Dr. Arkadiusz Malinowski, Ms. Sachiko Iseki, Dr. Shang Chen, Mr. Hyung Jun Cho, Mr. Hitoshi Watanabe, Mr. Takuya Takeuchi, Mr. Yusuke Abe, Mr. Yudai Miyawaki, Mr. Yi Lu, Mr. Toshiya Suzuki, Mr. Hironao Shimoeda, Mr. Sho Kawashima, Mr. Tokushige Kino, Mr. Koji Yasuda, Mr. Leyong Yu, Mr. Masanori Kato, Mr. Naoya Sumi, Mr. Tatsuya Hagino, Mr. Shinpei Amasaki, Mr. Takayuki Kanda, Mr. Yusuke Kondo, Mr. Jong Yun Park, Ms. Ya Lu, Mr. Minyoung Ahn, Mr. Kohei Asano, Mr. Jun Kuki, Mr. Ryosuke Kometani, Mr. Atsushi Fukushima, Mr. Takeyoshi Horibe, Mr. Tomohiro Takahashi, Mr. Jiadong Cao, Mr. Kuangda Sun, Mr. Zecheng Liu, Mr. Haoran Wang, Mr. Makoto Isobe, Mr. Takashi Kako, Mr. Ryo Gonda, Mr. Masayuki Nakamura, Mr. Hiroki Nagano, Mr. Keita Miwa, for giving the big pleasure in life and creating a most enjoyable work atmosphere. I also appreciate the enough secretarial supports to Ms. Megumi Oshigane, Ms. Azusa Ohta, Ms. Mitsuko Era, Ms. Naoko Kataoka, and Ms. Masako Takahashi for helping me to concentrate on the research without any problem of administrative task.

Finally, I would like to dedicate this thesis to my parents, my sister, and good friends.

*Takehiro Hiracka*

January 2013

## List of Papers

### 1. Original Papers

<i>Title</i>	<i>Journal</i>	<i>Authors</i>
1 Temperature measurement of Si substrate using optical-fiber-type low-coherence interferometry employing super continuum light	Japanese Journal of Applied Physics, <b>52</b> , 026602 (2013).	T. Hiraoka, T. Ohta, T. Kageyama, M. Ito, N. Nishizawa, M. Hori (Chapter 3)
2 Temperature Measurement of Silicon Substrate with Carbon Nanowalls Using Optical low-Coherence Interferometry	Japanese Journal of Applied Physics, (Submitted)	T. Hiraoka, T. Ohta, M. Ito, N. Nishizawa, M. Hori (Chapter 4)
3 Optical-Fiber-Type Broadband Cavity Ring-Down Spectroscopy Using Wavelength-Tunable Ultrashort Pulsed Light	Japanese Journal of Applied Physics, (accepted)	T. Hiraoka, T. Ohta, M. Ito, N. Nishizawa, M. Hori (Chapter 5)

## 2. International Conferences

	<i>Title</i>	<i>Journal</i>	<i>Authors</i>
1	Non-Contact Measurement of Substrate Temperature Using Optical Low-Coherence Interferometry (Oral)	The 9th Korea-Japan Workshop on Thin Film and Plasma Process for Green Technology Advanced Plasma Diagnostics for Plasma-Nano Processing, <b>KJP-08</b> , Kwangwoon University, Seoul, Korea, July 9-11, 2009.	T. Hiraoka, T. Kageyama, T. Ohta, K. Takeda, M. Ito, and M. Hori
2	Accurate Monitoring System for Silicon Wafer Temperature Using Super-Continuum Light Source on Low-Coherence Interferometry	2nd International Symposium on Advanced Plasma Science and its Application, <b>PA007A</b> , p.120, Meijo University, Nagoya Japan, Mar. 7-10, 2010.	T. Hiraoka, T. Kageyama, C. Koshimizu, T. Ohta, M. Ito, N. Nishizawa, and M. Hori
3	Measurement of silicon substrate temperature by optical low coherence interferometry using Super-Continuum light (Oral)	The 11th International Workshop on Advanced Plasma Processing and Diagnostics, <b>PO-04</b> , p.31, Ramada Jeju Hotel, Jeju, Korea, July 8-9, 2010.	T. Hiraoka, T. Ohta, M. Ito, N. Nishizawa, and M. Hori

## List of Papers

4	High resolution measurement of silicon wafer temperature using super-continuum light on optical low-coherence interferometry	63rd Annual Gaseous Electronics Conference and 7th International Conference on Reactive Plasmas, <b>CTP. 66</b> , p.27, Paris, France, October 4-8, 2010.	T. Hiraoka, C. Koshimizu, T. Ohta, M. Ito, N. Nishizawa, and M. Hori
5	Study of Terahertz Time Domain Spectroscopy for Biological Plasma Applications (Oral)	The 12th International Workshop on Advanced Plasma Processing and Diagnostics, <b>S09</b> , Kyushu University, Fukuoka, Japan, Jan. 4-6, 2011.	T. Hiraoka, K. Takeda, K. Ishikawa, H. Kondo, M. Ito, M. Sekine, M. Hori
6	Measurement of Optical Properties of Carbon-based Material Using Terahertz Time domain Spectroscopy	3rd International Symposium on Advanced Plasma Science and its Applications for Nitrides and Nanomaterials, Nagoya Institute of Technology, <b>P2-002A</b> , p.97, Nagoya, Japan, Mar. 6-9, 2011.	T. Hiraoka, K. Takeda, K. Ishikawa, H. Kondo, M. Ito, M. Sekine, and M. Hori

List of Papers

7	<p>Evalutaion of Penicillium digitatum sterilization using non-equilibrium atmospheric pressure plasma by terahertz time-domain spectroscopy (Oral)</p>	<p>64th Annual Gaseous Electronics Conference, <b>DT2.7</b>, p.20, Salt Lake City, Utah, Nov. 14-18, 2011.</p>	<p>T. Hiraoka, N. Ebizuka, K. Takeda, T. Ohta, H. Kondo, K. Ishikawa, K. Kawase, M. Ito, M. Sekine, and M. Hori</p>
8	<p>Terahertz time-domain spectroscopy for penicillium digitatum sterilization using non-equilibrium atmospheric pressure plasma</p>	<p>4th International Symposium on Advanced Plasma Science and its Applications for Nitrides and Nanomaterials, <b>P1021A</b>, p.74, Chubu University, Aichi, Japan, Mar. 4-8, 2012.</p>	<p>T. Hiraoka, N. Ebizuka, K. Takeda, T. Ohta, K. Ishikawa, M. Ito, K. Kawase, M. Sekine, M. Hori</p>
9	<p>Temperature Measurement of Carbon Nanowall/Silicon Substrate Using Fourier-Domain Low-coherence Interferometry</p>	<p>5th International Conference on PLASMA-NanoTechnology &amp; Science, <b>P-35</b>, Freude, Inuyama International Sightseeing Center, Aichi, Japan, Mar. 9-10, 2012.</p>	<p>T. Hiraoka, M. Natsume, H. Kato, T. Tsutsumi, T. Ohta, M. Ito, K. Takeda, H. Kondo, M. Hori</p>

List of Papers

<p>10 Terahertz Time-domain Spectroscopic Sensing of Penicillium Digitatum Inactivated by Non-equilibrium Atmospheric Pressure Plasmas</p>	<p>2012 MRS Spring Meeting &amp; Exhibit, <b>WW-7.3</b>, Moscone West Convention Center / Marriott Marquis, San Francisco, California, Apr. 9-13, 2012.</p>	<p>T. Hiraoka, N. Ebizuka, K. Takeda, T. Ohta, K. Ishikawa, M. Ito, K. Kawase, M. Sekine, and M. Hori</p>
<p>11 Optical Properties of Carbon Nano Walls in Terahertz Frequencies Region</p>	<p>11th APCPST / 25th SPSM, <b>2-P45</b>, p.282, Kyoto University ROHM Plaza, Kyoto, Japan, Oct. 2-5, 2012.</p>	<p>T. Hiraoka, K. Takeda, T. Ohta, N. Ebizuka, H. Kondo, K. Ishikawa, K. Kawase, M. Ito, M. Sekine, and M. Hori</p>
<p>12 Temperature measurement of substrate with a thin film using low-coherence interference</p>	<p>65th Annual Gaseous Electronics Conference, <b>UF3.1</b>, p.108, Austin, Texas, USA, Oct. 22-26, 2012.</p>	<p>T. Tsutsumi, T. Hiraoka, K. Takeda, K. Ishikawa, H. Kondo, T. Ohta, M. Ito, M. Sekine, and M. Hori</p>
<p>13 Measurement of carbon nanowalls / silicon substrate temperature by Fourier-domain low-coherence interferometry</p>	<p>5th International Symposium on Advanced Plasma Science and its Applications for Nitrides and Nanomaterials, <b>P1022A</b>, p.79, Nagoya University, Aichi, Japan, Jan. 28 - Feb. 1, 2013.</p>	<p>T. Hiraoka, T. Tsutsumi, H. Kato, K. Takeda, T. Ohta, H. Kondo, K. Ishikawa, M. Ito, M. Sekine, M. Hori</p>

## List of Papers

14	Real time temperature measurements of film-covered-substrate employing fourier domain low coherence interferometer during plasma processes	5th International Symposium on Advanced Plasma Science and its Applications for Nitrides and Nanomaterials, <b>P1023A</b> , p.80, Nagoya University, Aichi, Japan, Jan. 28 - Feb. 1, 2013.	T. Tsutsumi, T. Hiraoka, K. Takeda, K. Ishikawa, T. Ohta, M. Ito, H. Kondo, M. Sekine, M. Hori
15	Temperature measurement of carbon nanowall / silicon substrate using super-continuum light source on low-coherence interferometry	6th International Conference on PLAsma-NanoTechnology & Science, <b>P-G11</b> , Gero Synergy Center, Gifu, Japan, Feb. 2-3, 2013.	T. Hiraoka, H. Kato, T. Tsutsumi, T. Ohta, M. Ito, K. Takeda, H. Kondo, M. Hori

### 3. Research Project

- International Training Program (Program for incubating young researchers on plasma nanotechnology materials and device processing, conducted by Japan Society for the Promotion of Science) in Prof. Graham research group, Queen's University Belfast, Belfast, Northern Ireland, UK, from January to March, 2011.